Impact of actuation frequency on mean topology and breakdown past a Laminar Separation Bubble

An Experimental Investigation

ME55035: ME-EFPT MSc Thesis

Sibasish Panda

Delft University of Technology

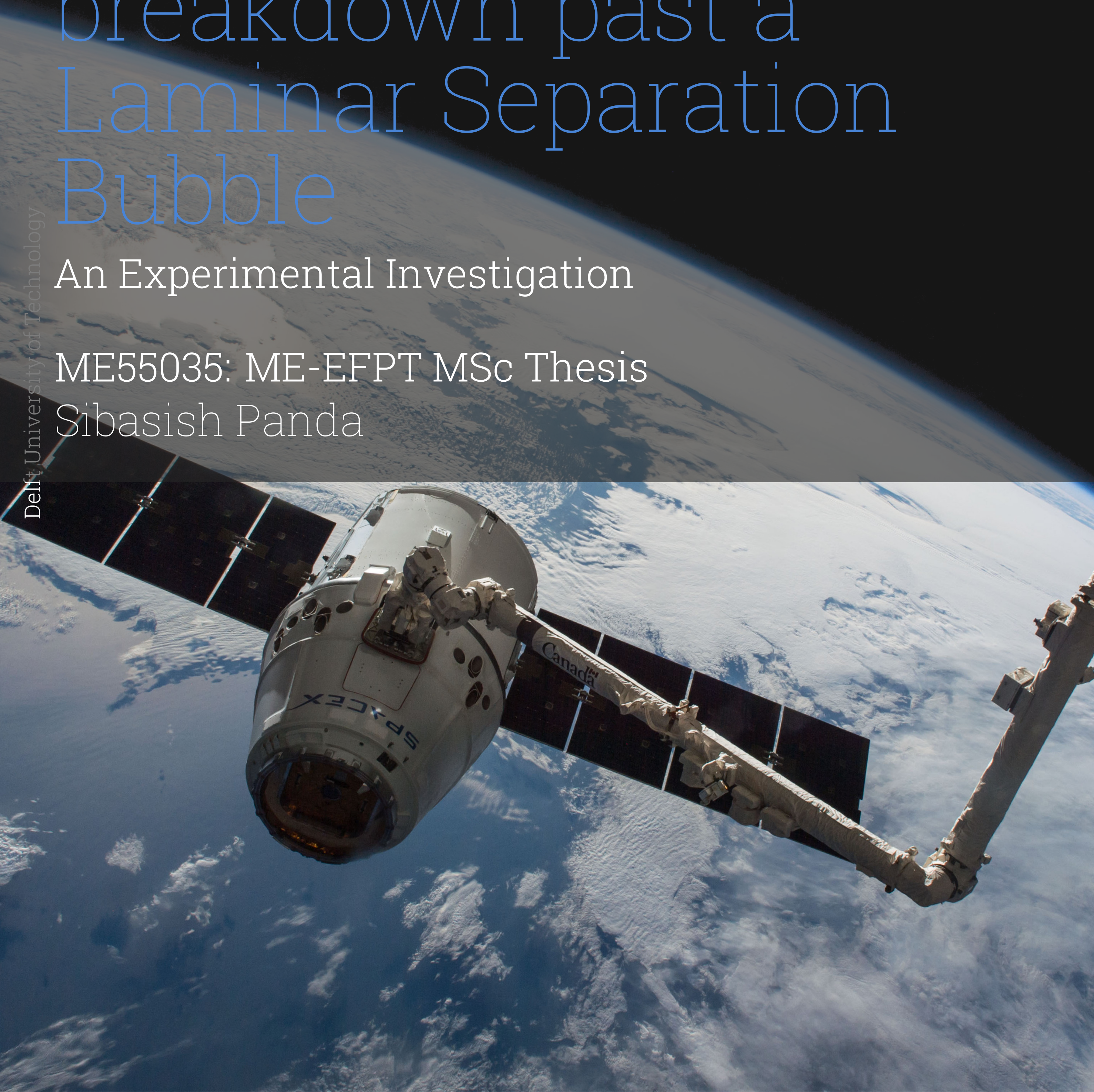

Impact of actuation frequency on mean topology and breakdown past a Laminar Separation Bubble

An Experimental Investigation

by

Sibasish Panda

Student number:	5939321
Thesis committee:	Dr. Theo Michelis, Supervisor
	Dr. Abel-John Buchner, Chair
	Nick Papanikolatos, Supervisor
	Dr. Gerrit Elsinga, External examiner
Project Duration:	December, 2024 - November, 2025
Faculty:	Faculty of Mechanical Engineering

Acknowledgements

What started as a childhood curiosity fed by science-fiction movies turned into an interest in aerospace engineering. Though my entrance rank and my fate sent me to chemical engineering for my bachelor's, that curiosity never really disappeared. Somewhere between mass and heat balances, I found my way back to fluid mechanics, and eventually to my master's at TU Delft. Doing my thesis in aerospace engineering with a background in chemical engineering has been both humbling and difficult, but one of the most fulfilling things I have ever done. As I reach the end of my master's, I have come to realize that it is rarely about the background and mostly about the process. It took me a painfully long time to realize that, and I hope I live by it in the future.

As I reach the end of my master's, I want to thank the people who made this possible. I want to thank Theo for taking the time, almost a year ago, to talk about all the available projects and then agreeing to supervise me on this one. Over the past year, what has stood out the most is how patient he has been with my confusion. No matter how basic, half-baked, or twisted my questions were, he always took them seriously, tried to understand where I was stuck, and then helped me walk through the ideas in our meetings until they finally made sense - sometimes only much later. I often walked into the meetings with an idea, and walked out with a direction and a clear perspective. Beyond his technical depth and sharp eye for detail, I have come to admire him as a person. His mix of honesty, sarcasm, and kindness made this journey far less intimidating. I am grateful to John, from whom I learned Advanced Fluid Dynamics in my first year. His Queen's English and dry humor often brought lightness to our weekly meetings. I am thankful that he was willing to supervise this work on top of his busy schedule, and for the time and care he put into reading my drafts and gently pushing the ideas a bit further each time. My thanks go to Nick for being available for the questions that I was too hesitant to ask anyone else. His doubling down on comparing color maps with identical limits and nitpicking sometimes frustrated me, but they definitely helped improve my thesis. I am thankful to him for this. I enjoyed our side conversations about the nuances of Greek names, and I was genuinely impressed by his ability to drive the big LSL van through the narrow streets of Delft. I would like to thank my fellow students in Master's room and the people of LSL for the discussion over the lunches that we had. I am grateful to the technical staff who played an important role in helping me set up the experiments, answered practical questions, and still trusted me around the equipment after I dropped an inclinometer.

To my friends in Delft, thank you for making my life fun. From those who were there from my very first day, Karthik, Vishal, Affan, Amrit, Manu, Kanza, Rushil, my library mates, and to those that I met along the way. To my dear DISS board, I am grateful for your company and the wonderful time we had together as a board. To my flatmates, Kishore and Sunruta, thank you for your patience with me in the past few months. Our shared dinners, cooking sessions, and talks about films and society kept me sane. To my seniors, Pritesh, Sarthak, Ezra, and Varun, I am grateful for all the advice that you have shared with me. I hope I have been able to do some justice to them. To my friends from bachelors, Prateek and Kaustuv, thank you for staying close across the distance and time zones. You helped me through some low points, advised me, and helped me settle in Delft, and even took the time to read and comment on parts of my thesis. It means a lot to have you as my friends. To my friends in the Odia group, thank you for bringing a taste of home to Delft. Being able to speak my mother tongue, joke about familiar things, and share food from my state made this place feel far warmer.

Finally, I owe my deepest thanks to my family. To my parents have supported every turn my academic path has taken, from chemical engineering to mechanical and then to aerospace, without telling me to play it safe. To my uncle and aunt have encouraged me at every step and pushed me to follow what I wanted, not just what was convenient. I am indebted to them for standing firmly behind me. To my brothers Mikun and Guddu, thank you for being my confidants.

I hope I have done good, I wish I could have done better.

Sibasish Panda
Delft, November 2025

Abstract

Laminar Separation Bubbles (LSBs) typically form in a low Reynolds number boundary layer flow involving a strong pressure gradient. These bubbles adversely impact the aerodynamic performance of a body by increasing the drag, susceptibility to stall, and noise emission. Since a large number of unmanned aerial vehicles and small wind turbine blades operate in a similar Reynolds number range, it is crucial to have an understanding of the bubbles' behavior to improve aerodynamic performance in these operating conditions. The frequency at which this bubble sheds due to amplification of disturbances is termed the natural, harmonic, or fundamental shedding frequency. The way in which the shed vortices break down impacts the behavior of the bubble, and hence it is crucial to study this breakdown of the vortices as well. Though previous works have shown that varying external forcing frequency alters the bubbles' behavior, there is no study investigating the variation of bubble topology and the breakdown of vortices in a forcing frequency regime varying from impulsive to fundamental forcing.

An experimental study is performed using a NACA 0018 airfoil in the Anechoic Tunnel at TU Delft. Under the chosen conditions, a short LSB forms on the suction side and is chosen as the baseline bubble for the current study. Using a spanwise uniform Alternating Current-Dielectric Barrier Discharge (AC-DBD) plasma actuator placed upstream of the separation point, two-dimensional forcing is applied. The actuator geometry and voltage are kept fixed while only the actuation frequency is varied from a low frequency regime, where the bubble has enough time to recover close to its natural state between the actuations, up to the regime where the forcing is close to the fundamental shedding frequency of the bubble. Surface pressure and velocity fields are measured using pressure taps and Particle Image Velocimetry (PIV), respectively. PIV measurements are done in both time averaged and phase averaged manner to gain insight into the vortex dynamics and breakdown characteristics. While the surface pressure taps along the airfoil chord provide time-averaged pressure measurements, PIV data captures the bubble topology in the wall normal plane, and the breakdown characteristics of the actuated wave packet in the wall parallel plane.

The LSB topology quantified in terms of bubble area shows a monotonic decrease in area with an increase in forcing frequency. The decrease in area is steep at lower forcing frequencies and gradual at higher forcing frequencies. The displacement thickness moves closer to the wall, and the maximum shape factor value shifts upstream, indicating increased stability of the free shear layer. Analysis of the breakdown characteristics shows distinct breakdown behavior across the forcing frequency ranges. At a lower forcing frequency, the breakdown shows features of the unforced bubble breakdown. In the subharmonic and fundamental forcing frequency range, the wavelength variation of the convected wave packet shows a distinct U-shape, indicating changed stability of the bubble as compared to lower forcing frequency actuation. The results provide valuable insights into the bubble topology and the breakdown characteristics under the considered forcing frequency range and can be useful in designing an active control system in the future for similar low Reynolds number range.

Contents

Acknowledgements i

Abstract iii

Nomenclature vi

1 Introduction 2
- 1.1 Structure of the report . . . 4

2 Background Theory 5
- 2.1 Navier-Stokes Equations . . . 5
- 2.2 Boundary Layer . . . 5
  - 2.2.1 Transition and Separation . . . 7
  - 2.2.2 Boundary Layer stability . . . 7
- 2.3 The Laminar Separation Bubble . . . 8
  - 2.3.1 Properties of laminar separation bubble . . . 9
  - 2.3.2 The feedback mechanism . . . 11
- 2.4 Evolution of instabilities in laminar separation bubbles . . . 11
- 2.5 Self-excitation in Laminar separation bubbles . . . 12
- 2.6 Classification of pertinent instabilities in an LSB . . . 13
- 2.7 Dynamics of Vortex shedding and reattachment . . . 14
- 2.8 Impact of external forcing on Mean flow of an LSB . . . 17
- 2.9 Impact of external forcing on the vortex dynamics of an LSB . . . 20

3 Research plan 26
- 3.1 Research questions . . . 26

4 Methodology 28
- 4.1 Experimental Techniques . . . 28
  - 4.1.1 Particle Image Velocimetry . . . 28
  - 4.1.2 Alternating Current - Dielectric Barrier Discharge actuator . . . 29
- 4.2 Experimental Setup . . . 30
  - 4.2.1 Experimental Facility . . . 30
  - 4.2.2 Airfoil and test-section . . . 31
  - 4.2.3 Low speed planar PIV and Setup . . . 32
  - 4.2.4 Plasma Actuator Setup . . . 35
  - 4.2.5 Plasma Actuator Characterisation . . . 35

5 Data processing 37
- 5.1 Non dimensionalisation and Notation . . . 37
- 5.2 Experimental Matrix . . . 38
- 5.3 Processing of Pressure Data . . . 38
- 5.4 Processing of PIV Data . . . 39
- 5.5 Processing of velocity signals . . . 40
  - 5.5.1 Fourier Analysis . . . 40

5.5.2 Wavelet Analysis 41
5.5.3 Convective Velocity 43

6 Results and Analysis **44**
6.1 Pressure data 44
6.2 Flow-field characteristics 45
6.2.1 Unforced bubble 45
6.2.2 Forced bubble 48
6.2.2.1 Time-averaged bubble behavior 49
6.2.2.2 Wave packet evolution in wall-normal and wall-parallel plane 51
6.3 Changes in Bubble topology 68
6.4 Breakdown Characteristics 70

7 Discussion and Conclusion **78**
7.1 Discussion 78
7.2 Conclusion 80

8 Recommendations **81**
8.1 Experimental Setup 81
8.2 Future research 82

Nomenclature

Abbreviations

Abbreviation	Definition
AC-DBD	Alternating Current–Dielectric Barrier Discharge actuator
AFC	Active Flow Control
AoA	Angle of Attack
APG	Adverse Pressure Gradient
BL	Boundary Layer
CV	Control Volume
DNS	Direct Numerical Simulation
FFT	Fast Fourier Transform
FOV	Field of View
FST	Free-stream turbulence
KH	Kelvin–Helmholtz (instability)
LNSE	Linearised Navier–Stokes Equations
LSB	Laminar Separation Bubble
LST	Linear Stability Theory
MFD	Mean Flow Deformation
NACA	National Advisory Committee for Aeronautics
PIV	Particle Image Velocimetry
POD	Proper Orthogonal Decomposition
PSD	Power Spectral Density
SIA	Secondary Instability Analysis
STFT	Short-Time Fourier Transform
T-S	Tollmien–Schlichting (waves)

Symbols

Symbol	Definition	Unit
C_p	Pressure coefficient	[–]
H	Boundary-layer shape factor	[–]
Re_c	Chord-based Reynolds number	[–]
R	Reattachment point (time-averaged)	[–]
S	Separation point (time-averaged)	[–]
T	Maximum bubble height location (time-averaged)	[–]
T_x	Momentum-flux integral (streamwise component)	[m^3/s^2]
T_y	Momentum-flux integral (wall-normal component)	[m^3/s^2]
c	Airfoil chord length	[m]

Symbol	Definition	Unit
f	Forcing frequency	[Hz]
f^+	Non-dimensional forcing frequency, $f^+ = fc/U_\infty$	[–]
U_c	Convective velocity of the wave packet	[m/s]
U_e	Local edge velocity at separation	[m/s]
U_∞	Free-stream velocity obtained from pitot	[m/s]
V	Velocity magnitude	[m/s]
r	Wavelength ratio λ_z/λ_x	[–]
t	Time	[s]
u	Streamwise velocity component	[m/s]
v	Wall-normal velocity component	[m/s]
w	Spanwise velocity component	[m/s]
x	Streamwise coordinate	[m]
x/c	Streamwise coordinate normalised by chord	[–]
y	Wall-normal coordinate	[m]
y/c	Wall-normal coordinate normalised by chord	[–]
z	Spanwise coordinate	[m]
z/c	Spanwise coordinate normalised by chord	[–]
Δt	Phase separation time between snapshots	[s]
δ^*	Displacement thickness	[m]
δ^*_0	Displacement thickness at separation in the unforced case	[m]
λ_x	Streamwise wavelength	[m]
λ_x/c	Streamwise wavelength normalised by chord	[–]
λ_z	Spanwise wavelength	[m]
λ_z/c	Spanwise wavelength normalised by chord	[–]
ν	Kinematic viscosity	[m^2/s]
Ω	Dimensional vorticity	[s^{-1}]
ω	Non-dimensional vorticity, $\omega = \Omega\delta^*_0/U_\infty$	[–]
ϕ	Phase index	[–]
ρ	Density	[kg/m^3]
θ	Momentum thickness	[m]

1

Introduction

In low Reynolds number ($10,000 \sim 500,000$) flows over an aerodynamic surface, a major obstacle to aerodynamic performance is the laminar separation of the boundary layer (Lissaman, 1983; Schlichting and Gersten, 2017). Along with small unmanned aerial vehicles and wind turbine blades, many other equipment operate in a similar Reynolds number range. Knowledge of flow physics could assist in preventing separation, improving aerodynamic and fuel efficiency in the aviation and energy sectors. While the aerodynamic performance of a body can be measured through several aspects, here, the adverse impact on lift and drag forces, noise emission, and stalling is relevant. Figure 1.1 highlights the region of interest in the Reynolds number-mass domain. In such flows, separation occurs beyond the point of minimum surface pressure, where an adverse pressure gradient causes the laminar boundary layer to detach. The separated boundary layer forms a free shear layer and transitions downstream of the separation point. For low Reynolds number or high angle of attack, the shear layer does not reattach, significantly affecting the body's aerodynamic performance. Conversely, at lower angles of attack, the transitioned flow reattaches due to sufficient momentum influx from the outer layer. This forms a turbulent boundary layer past the reattachment point, enhancing the aerodynamic performance. However, the reattachment can be described only in a time-averaged sense. This reattachment results in formation of a closed flow region, commonly referred to as a *Laminar Separation Bubble (LSB)*. The term "laminar" refers to the condition of the boundary layer at the point of separation rather than the flow conditions. An experimental visualization of a Laminar Separation Bubble along with its vortex shedding is shown in Fig. 1.2.

The separated shear layer transition is of particular importance as it dictates the dynamics of the laminar separation bubble. This transition is dependent on the evolution of incoming disturbances in the flow in the form of Tollmien-Schlichting waves. Such waves are input into the flow through the process of receptivity (Reed and Saric, 2015). While the disturbances include a broadband of frequencies, the inherent inviscid instability mechanism amplifies only a specific band of frequencies. This band is generally the natural or fundamental instability, which corresponds to the shedding frequency of the bubble. The Kelvin-Helmholtz instability mechanism dominates the initial linear stage of this amplification. These primary disturbances grow and saturate, leading to two-dimensional shear layer roll-ups and eventual vortex shedding. Post-shedding, the vortices deform and break down, driven by secondary instability mechanisms. The mechanism and length over which the breakdown happens are important as they influence the pressure distribution behind the separation bubble, and consequently, the global pressure field. The change in the global pressure field dictates the growth of disturbances in the fore part of the

LSB. This establishes a feedback loop that influences the formation and characteristics of the Laminar Separation Bubble (Rist, 2002).

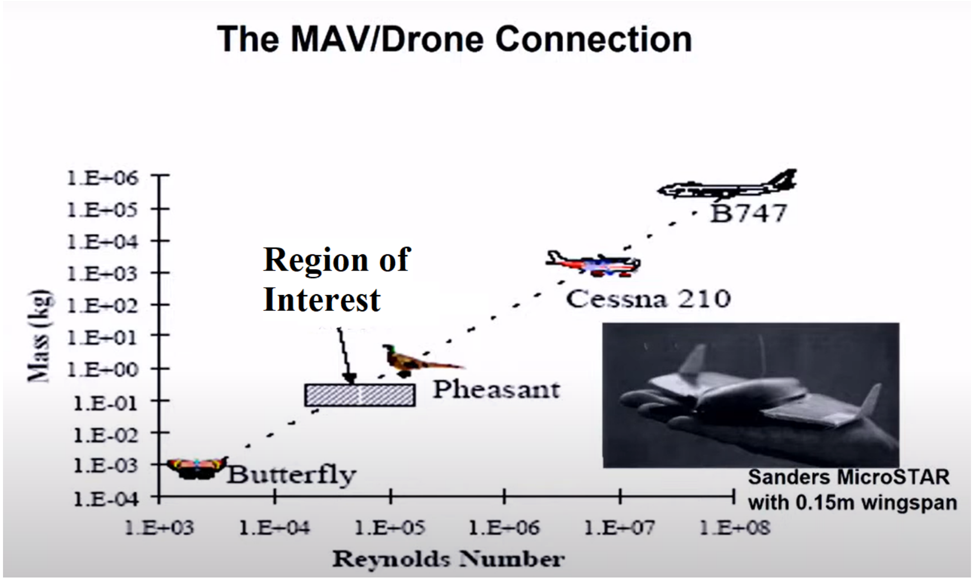

Figure 1.1: Reynolds number range for flight vehicles in Reynolds number-mass domain, highlighting the region of interest. Source: Mueller and JANSEN (1982).

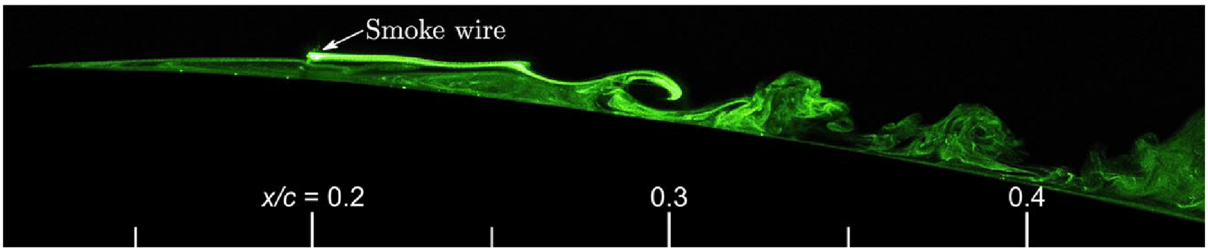

Figure 1.2: Flow visualisation of a Laminar separation bubble using the smoke wire technique. This shows a laminar separation bubble shedding instantaneously. Source: Lambert and Yarusevych (2017).

The motivation for this study stems from the desire to understand the behavior of Laminar Separation Bubbles (LSB), which can prevent undesirable outcomes such as stalling, loss of lift, or increased drag. A flow control mechanism can be used to introduce a wave packet mimicking a disturbance under which the bubble's response and its breakdown can be studied for diagnosis. The amplitude and frequency of introduction of the wave packet influence the breakdown of the wave packet-generated vortices in the aft part of the laminar separation bubble. While several studies (Yarusevych and Kotsonis, 2017; Kurelek et al., 2021) investigate the effect on bubble topology in the fundamental (natural shedding frequency of an LSB) and its harmonic forcing frequency regimes, a few studies (Michelis et al., 2017; Watmuff, 1999) investigate the effect of impulsive forcing. To date, there have been no studies on the bubble topology and breakdown in the gap between the impulsive and harmonic forcing frequencies.

With the premise of the current study established, this research aims to fulfill the main objective:

> **Investigating the effect of periodic actuation frequency on LSB topology and vortex breakdown characteristics with a focus on the forcing range between impulsive and continuous actuation.**

1.1 Structure of the report

The report is organized as follows: Chapter 2 introduces the fundamental concepts of boundary layer, its stability, separation, relevant instability mechanisms, a brief overview of methods for its control, the Laminar Separation Bubble, and its dynamics. It delves into the instability mechanisms that are present and affect the LSB topology, self-excitation mechanisms, and the predominant types of instabilities. This chapter also details the dynamics of vortex shedding, flow reattachment, and the impact of external forcing. The findings are then used to motivate and formulate the research questions. Chapter 3 outlines the research plan, reiterates the identified research gaps, and presents the research questions that this thesis aims to address. Chapter 4 details the experimental setup, where model design, experimental techniques, equipment used, and constraints are covered. Post-processing methodologies are explained in Chapter 5, followed by the presentation, analysis, and discussion of the results in Chapter 6. The conclusions drawn from this research are presented in Chapter 7. Lastly, Chapter 8 gives recommendations for future research.

2

Background Theory

This chapter gives a brief overview into the theoretical concepts necessary for understanding boundary layer flow, its separation, and control. While sufficient effort has been made to give a comprehensive overview, an exhaustive picture of the theory and underlying concepts can be obtained by going through the cited literature.

2.1 Navier-Stokes Equations

Molecular interaction at a particular density range forms a continuous state of matter termed generally as "*fluid*". This state of matter is ubiquitous, and its study, fluid mechanics, has been referred to as a fundamental strand of physics and engineering. The study of the effect of forces on such a continuous state of matter can be described by a set of governing equations termed as the *Navier-Stokes equations*, which are essentially Newton's laws of motion applied to a fluid element in a continuum. These equations describe the motion of a fluid by accounting for the conservation of mass, momentum, and energy. For an incompressible fluid, the following form of Navier-Stokes Equations describes fluid behavior (White and Majdalani, 2006):

$$\nabla \cdot \mathbf{u} = 0 \tag{2.1.1a}$$

$$\frac{\partial \mathbf{u}}{\partial t} + (\mathbf{u} \cdot \nabla)\mathbf{u} = -\nabla p + \nu \nabla^2 \mathbf{u} + \mathbf{F} \tag{2.1.1b}$$

where equation 2.1.1a represents mass conservation and equation 2.1.1b represents momentum conservation; $\mathbf{u}$ represents the local fluid velocity, p denotes the pressure, ρ is the density of the fluid, and ν is kinematic viscosity. The operator ∇ is the spatial gradient operator, and t represents time. The $\frac{\partial \mathbf{u}}{\partial t}$ term represents the local acceleration of the fluid and $(\mathbf{u} \cdot \nabla)\mathbf{u}$ is the convective acceleration. The term $-\nabla p$ denotes the pressure gradient force, $\nu \nabla^2 \mathbf{u}$ represents viscous dissipation of momentum, and $\mathbf{F}$ accounts for external body forces. Hence, the left-hand side of the equation 2.1.1b accounts for a positive acceleration of the fluid in space that is brought by any body force, pressure gradients, and viscous effects. These equations are accompanied by boundary and initial conditions to properly describe real-world flows.

2.2 Boundary Layer

In his seminal work, Prandtl (1904) defined boundary layer and its properties. Fluid flow on a surface necessitates a *no-slip* boundary condition on the surface. This leads to a velocity gradient that eventually merges into the freestream flow. The velocity gradient occurs primarily due to the dominance of viscous forces, which mimic friction in a fluid and oppose relative motion. Beyond the extent of the boundary layer region, the flow can be considered inviscid. Figure 2.1shows a simple and widely prevalent schematic of boundary layer development over a flat plate. The Reynolds number(Re) is defined as the ratio of inertial viscous forces in the flow and is represented mathematically as

$$\mathrm{Re} \equiv \frac{\text{inertial forces}}{\text{viscous forces}} = \frac{\rho U_\infty L}{\mu} = \frac{U_\infty L}{\nu} \tag{2.2.1}$$

where ρ is the fluid density, U_∞ is the freestream velocity, L is the reference length, μ is the dynamic viscosity and ν is the kinematic viscosity. A higher Re value indicates a reduced influence of viscous force and, hence, a thinner boundary layer. The Reynolds number is used to categorize if fluid flow is Laminar or Turbulent. Laminar flow is described and visualized by no mixing and velocity fluctuations while a turbulent flow is characterized by chaotic motion, manifested in the form of vortex breakdown, facilitating an energy cascade. The effect of viscous forces inside a boundary layer can also be studied using the shear stress (τ), expressed mathematically as:

$$\tau = \nu \frac{du}{dy}. \tag{2.2.2}$$

As it is dependent on the gradient of velocity, τ has a maximum value at the surface and tends to zero on reaching the freestream.

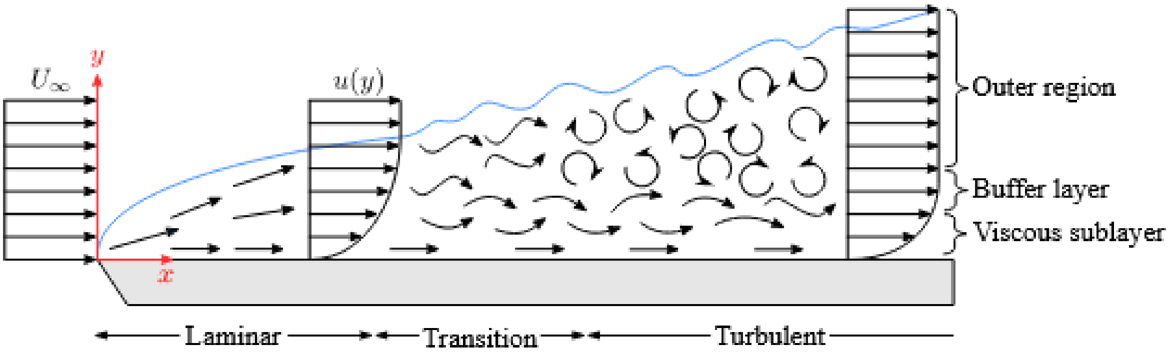

Figure 2.1: Schematic of boundary layer laminar to turbulent transition. Source: Michelis (2017).

The three prevalent methods used for estimating boundary layer thickness have been summarized and referenced from the seminal work by Schlichting and Gersten (2017). The commonly used definition, the extent of the boundary layer (denoted by δ_{99}) can be crudely ascertained to be till the point where the fluid velocity reaches 99% of its freestream value (U_∞). Different measures of boundary layer thickness other than the arbitrarily defined δ_{99} are the displacement and momentum thicknesses (Kundu et al., 2024). Displacement thickness, denoted by δ^*, indicates the degree of vertical displacement of streamlines due to the boundary layer and is analogous to the mass deficit associated with the boundary layer while momentum thickness accounts for momentum deficit (Schlichting and Gersten, 2017). The mathematical formulations of displacement and momentum thickness are presented in equations 2.2.3a and 2.2.3b, respectively.

$$\delta^* = \int_0^\infty (1 - \frac{u}{U_\infty})\, dy \tag{2.2.3a}$$

$$\theta = \int_0^\infty \frac{u}{U_\infty}(1 - \frac{u}{U_\infty})\, dy \tag{2.2.3b}$$

Shape factor (H) is defined as the ratio of the displacement and momentum thicknesses. This parameter is relevant in the context of this report as it determines boundary layer stability. It can be represented mathematically as

$$H = \frac{\delta^*}{\theta} \tag{2.2.4}$$

2.2.1 Transition and Separation

The boundary layer at formation is usually laminar, which may evolve into a turbulent boundary layer or undergo separation. Both of these pathways occur for one reason: to account for the lost momentum due to viscous forces inside the laminar boundary layer. Transition is necessary in transferring momentum from the boundary layer and plays an important role in the formation of the Laminar Separation Bubble. A brief discussion of the transition process of the boundary layer is given. While the initiation of transition of a laminar boundary layer is dependent on the disturbances through receptivity (Reed and Saric, 2015) and properties of the mean flow, surface morphology also plays a role (Schlichting and Gersten, 2017). A comprehensive review on boundary layer transition by Tani (1969) conveys the underlying physics of transition, including disturbance evolution and development from a stability point of view. It further distinguishes natural and forced transition while listing various sources that can induce transition. The listed sources include the effect of free-stream Turbulence Intensity, pressure gradient, surface curvature, and roughness. An overview of the transition to a turbulent boundary layer was given by Morkovin (1994), who emphasized that the process of transition begins with the process of receptivity. Subsequent works by Saric et al. (2002) and Mack (1984) expanded and provided more insights.

One of the primary forces that affects the aerodynamics of a body is the Drag force. It can be classified into two types: skin friction drag and pressure drag. Skin friction drag is due to the surface effects and roughness, whereas pressure drag occurs due to boundary layer separation. Since the magnitude of pressure drag is much larger than the skin friction drag in separated flows, controlling the boundary layer separation significantly improves aerodynamic performance. On imposition of an adverse pressure gradient on the surface, the resistance increases in the flow direction. As there is no momentum influx to replenish the lost momentum due to viscous forces, the boundary layer separates to form a free shear layer. This can be reasoned by a balance of the right-hand side terms in equation 2.1.1b. The point of separation of the boundary layer is characterized by the zero wall shear stress (τ_w).

2.2.2 Boundary Layer stability

The state of a boundary layer can be described by studying its stability characteristics. Boundary layer stability is important for understanding transition and separation. In literature (Mack, 1984; Schlichting and Gersten, 2017), the Tollmien-Schlichting (T-S) waves represent small instabilities often represented by low amplitude sinusoidal waves traveling parallel to the boundary inside the boundary layer. The behavior of these waves is defined by their initial amplitude and

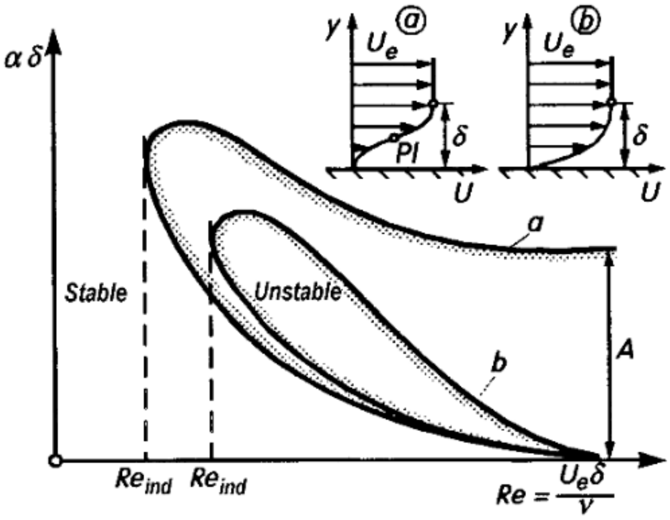

Figure 2.2: Curves of neutral stability of a plane boundary layer for two-dimensional incompressible perturbations. (a) "inviscid" instability, (b) "viscous" instability. Source: Schlichting and Gersten (2017).

frequency, which influence their evolution as per the stability theory. Early stages of development of these perturbations can be predicted using linear theory.

A disturbance (instability wave) can dampen, amplify, or be neutral depending on its location on a wavenumber-Reynolds number space, and the growth rate predicting such behavior can be illustrated by a stability diagram as shown in figure 2.2. It is important to note that the minimal critical Reynolds number ($\mathrm{Re}_{\mathrm{cr}}$) denotes the beginning of amplification and not the transition point. For a given initial disturbance spectrum, the stability theory identifies the frequency whose amplitude increases the most at each Reynolds number. These amplified wave at a particular frequency ultimately reaches a critical amplitude and trigger the transition process.

A brief overview of the instability mechanisms relevant for this study is given. The T-S instability mechanism amplifies the disturbances that penetrate the boundary layer through receptivity (Morkovin, 1994). The disturbances originate from experimental conditions, environmental noise, or vibrations. The viscous amplification process is slow, and they move downstream in the still attached BL in the favorable pressure gradient part. Another instability mechanism, the Kelvin-Helmholtz (KH)instability mechanism primarily arises from the shear between two fluid layers (Mack, 1984; Chandrasekhar, 2013; Schlichting and Gersten, 2017). The shear might occur within a single fluid or across an interface between two different fluids due to a relative velocity difference between these layers.

2.3 The Laminar Separation Bubble

Under a strong adverse pressure gradient, the attached boundary layer can separate to form a free shear layer. The separated shear layer can develop in two ways: it can either remain separated, leading to a drastic decrease in its aerodynamic performance (stall, loss of lift, and increase in drag), or it can reattach, which improves the aerodynamic performance. This separated boundary layer is highly unstable as the instabilities introduced into the attached boundary layer (as T-S waves), prior to its separation, through the process of receptivity (Morkovin, 1994) are quickly amplified by the KH mechanism. The transfer mechanism from T-S mode to KH mode happens near the separation point in the Adverse Pressure Gradient (APG) region. The initial growth of these instabilities in the separated shear layer can be modeled using linear stability theory; these instabilities gradually saturate and manifest in the form of vortices. These vortices shed and transfer the momentum from the outer flow towards the boundary and effectively cause the flow to reattach in a time-averaged manner (this can be inferred from figure 2.3). This momentum exchange can be explained using the terms of the equation 2.1.1b. The net momentum loss, which leads to separation, is due to an adverse pressure gradient imposed on the airfoil surface and momentum losses due to viscous forces. However, the shed vortices infuse momentum, causing attachment to the boundary. The reattached shear layer gradually develops into a turbulent boundary layer later. This time-averaged reattachment traps a recirculating region of fluid, effectively forming a "Laminar Separation Bubble". A simplified instantaneous and time-averaged schematic of the bubble is presented in figure 2.3.

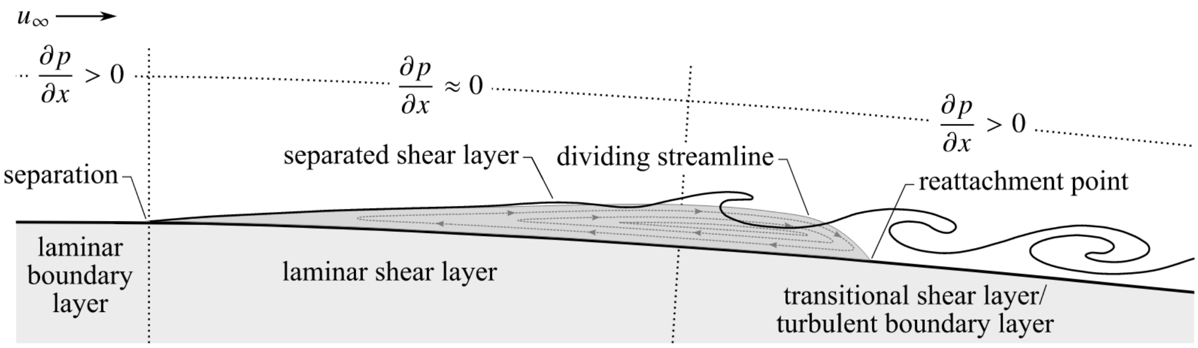

Figure 2.3: Cross-sectional (both instantaneous and time-averaged) view of a Laminar Separation Bubble (LSB). The partial derivatives in the figure are indicative of the corresponding pressure gradient in the region. Source: Kurelek (2021).

2.3.1 Properties of laminar separation bubble

Preliminary studies by Tani (1964); Horton (1968) and Gaster (1967) on LSB provide insights into the mean topology of the bubble, and fundamental properties, which are discussed herein. The figure 2.4 shows the sudden decrease in lift and increase in drag due to the formation of a laminar separation bubble in the Reynolds number range of $10^4 - 10^5$. Additionally, the size of the bubble plays a major role in dictating the forces experienced by the aerodynamic surface. The coefficient of pressure is obtained by scaling the pressure at a point with dynamic pressure. This is shown in equation 2.3.1.

$$C_p = \frac{p - p_\infty}{\frac{1}{2}\rho U_\infty^2} \tag{2.3.1}$$

where p_∞ is the freestream pressure. Based on the length of the formed bubble, it can be classified into either a long or a short laminar separation bubble (Gaster, 1967). A short bubble exists when the flow Reynolds number is less that $10^2\delta_s - 10^3\delta_s$ (where δ_s is the displacement thickness), it extends for a short percentage of chord length of the airfoil and is stable for a short duration (Robinet, 2013). Marxen and Henningson (2011) detail and summarize several features of a short bubble observed in due course of other studies. On the other hand, if the Reynolds number exceeds $10^4\delta_s$, a long bubble of 20-30% of the chord length forms, affecting the global pressure distribution, which drastically affects the aerodynamics of the lifting surface (Tani, 1964). Air-

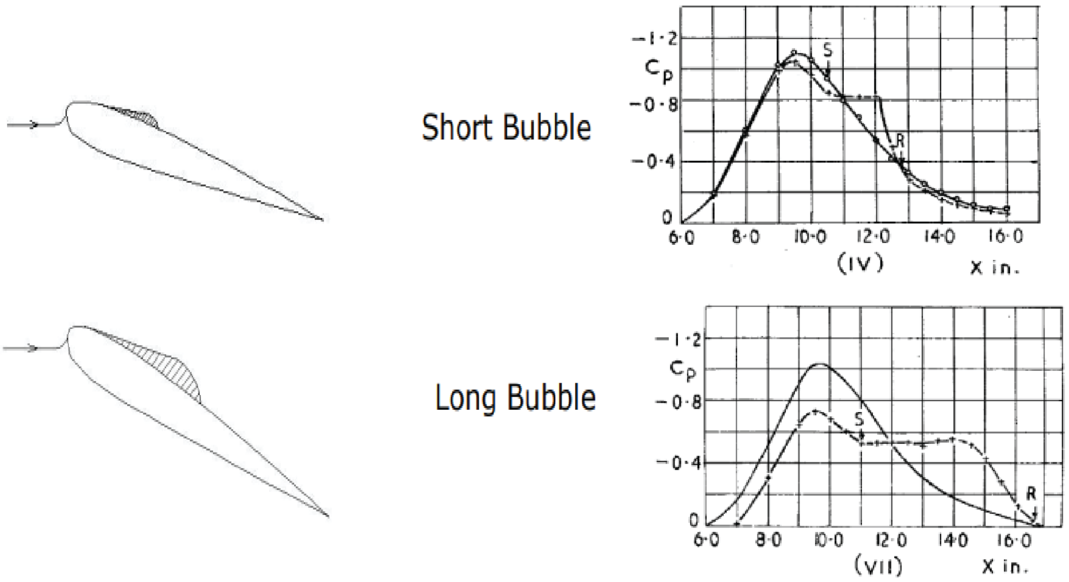

Figure 2.5: Long and short bubble with pressure profiles. Source: Gaster (1967).

foils operating above a Reynolds number of 10^6 experience early transition to turbulent flow and do not experience flow separation (Aftab et al., 2016). This is evident in figure 2.4.

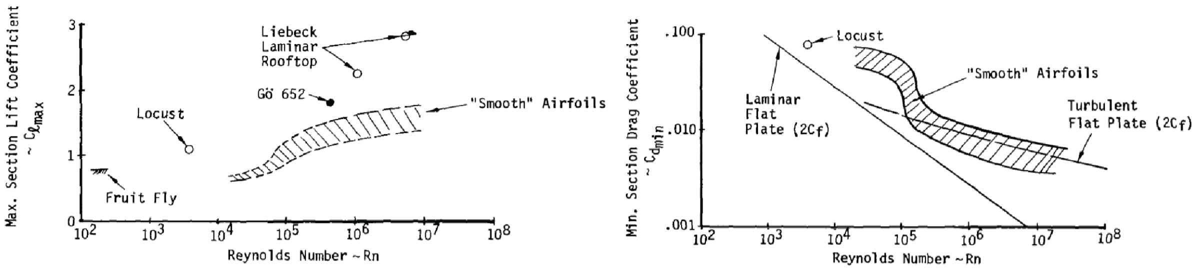

Figure 2.4: Abrupt changes in aerodynamic forces due to laminar separation. Source: McMasters and Henderson (1979).

Tani (1964) states that the region underneath the separated flow is formed of quiescent or slowly circulating fluid and is referred to as a dead-air region, as evident in figure 2.3. Such a slowly circulating flow can be associated with a ‘region of nearly constant static pressure’ is called the pressure-plateau region. This plateau region in a short separation bubble enhances the lift, whereas a long separation bubble decreases the lift significantly. This can be seen in figure 2.5. Early research on the “bursting” phenomenon by Gaster (1967) defines it as a phenomenon in which a short LSB switches to form a long LSB because of a variation in flow conditions. Gaster (1967)’s seminal research on defining the bursting criterion is modified and improved by studies of Diwan and Ramesh (2009) and Dellacasagrande et al. (2024). Study by Marxen and Henningson (2011) treat bursting as a dynamic phenomenon and highlight the relevance of bursting on reattachment dynamics and transition between long and short bubbles. Another dynamic behavior associated with LSB is ”flapping”. The low-frequency oscillations manifest in terms of global displacement of the separated shear layer with a nearly periodic growth and reduction of the reversed flow region (Zaman et al., 1989). Rist (2002) hypothesizes a few mechanisms associated with flapping that include receptivity, instability of bubble, interactions between transition, mean flow, and far-field boundaries. In a study, Marxen and Henningson (2011) claims flapping and bursting to be driven by altered stability characteristics due to the influence of incoming disturbances of different amplitudes. Understanding the flapping and bursting provides insights into bubble behavior over a range of flow conditions.

2.3.2 The feedback mechanism

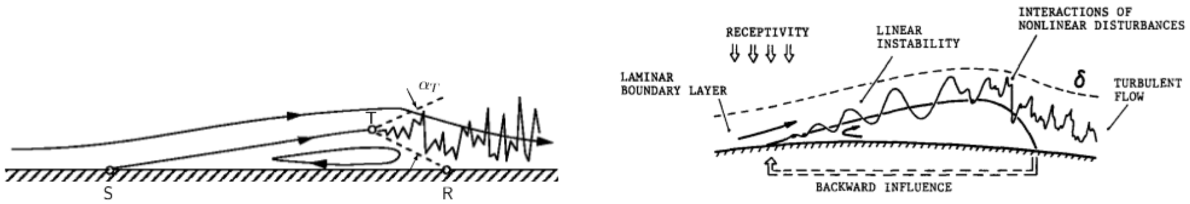

(a) Transitional laminar separation bubble. Source: Rist (2002).

(b) Vortex shedding feedback mechanism. Source: Dovgal et al. (1994).

Figure 2.6: Comparison of laminar separation bubble dynamics and feedback mechanisms.

Figure 2.6a provides a simplified time-averaged representation of an LSB. S represents the separation point, T the transition, R the reattachment point and α_T the turbulence wedge. These shed vortices eventually deform and break down into turbulence in the aft portion of the LSB. This shedding and eventual breakdown significantly affect the pressure field surrounding the bubble, which in turn affects the evolution of incoming flow perturbations and, hence, the properties of the LSB as a whole. This mechanism effectively forms a feedback loop as highlighted schematically in figure 2.6b. This highlights the paramount importance of understanding and controlling vortex shedding dynamics past an LSB. This report outlines sources of incoming disturbances, various types of instabilities, their amplification mechanisms, vortex-shedding processes, their deformation, and eventual breakdown.

2.4 Evolution of instabilities in laminar separation bubbles

This section uses previously introduced concepts to describe and detail the instability evolution in the context of laminar separation bubbles. The separated shear layer is inherently unstable and undergoes a series of instability mechanisms that amplify disturbances and eventually lead to vortex roll-up. An attempt is made to explain the sequence of events chronologically. The concept of *Receptivity* (Morkovin, 1994), explains how external disturbances are introduced in the boundary layer. The listed sources of these disturbances have been described explicitly by Rist (2002):

- Free-stream disturbances including sound and vorticity fluctuations: Their mutual interaction can lead to formation of T-S waves near the leading edge where the boundary layer has large enough stream-wise gradients.
- Interaction of acoustic disturbances with local wall roughness and upstream vortex shedding.
- Shear-layer flapping and *Feedback Mechanisms*.

Studies by Robinet (2013), and Rist (2002) highlight the transfer of amplification mechanism from viscous T-S to the inviscid KH mechanisms near the separation point. After the shear layer separates, KH instability governs the amplification of disturbances that saturate to form vortices, and their eventual breakdown into turbulence.

As a first, Diwan and Ramesh (2009) establish the primary instability in an LSB to be inflectional in nature and assert that this instability is a logical extension of the T-S instabilities in the attached boundary layer upstream. They further state that Kelvin-Helmholtz instabilities become relevant only when the separated shear layer moves considerably away from the wall. This is backed by Rist (2002), who note that *a contribution from a KH-instability can be expected only for large shear-layer distances from the wall*. Furthermore, he states that the instability contribution of T-S instability depends inversely on shear layer distance. Similarly, Watmuff (1999) and Boutilier and Yarusevych (2012) assert a negligible viscous contribution to disturbance development and attribute disturbance evolution to KH instabilities. While initially linear, these disturbances gradually develop non-linear characteristics and saturate to form vortices. (Marxen et al., 2013; Yarusevych and Kotsonis, 2017; Michelis et al., 2018) summarize this process and assert that the separation bubble development is governed by the formation of shear layer roll-up, which originate from the amplification of disturbances in the separated shear layer. *The above studies support the narrative that the separated shear layer acts as an amplifier, selectively enhancing the incoming disturbances at particular frequencies.*

2.5 Self-excitation in Laminar separation bubbles

In the absence of any external forcing, including limited incoming turbulence, several numerical studies report spanwise variation in the time-averaged mean of the bubble. Depending upon the reverse flow magnitude inside the bubble, an instability can be induced in the absence of external disturbances (Rodríguez et al., 2013, 2021). It is important to note that such an observation in *experimental studies is difficult, as achieving zero turbulence intensity (FST) in the incoming flow is not possible*.

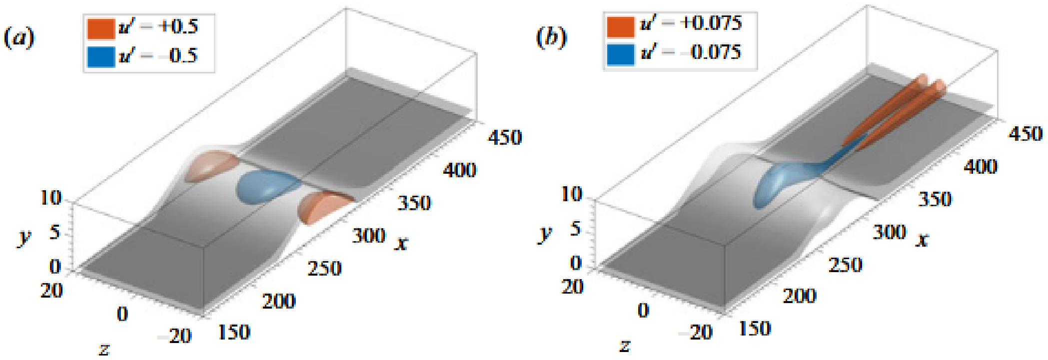

Figure 2.7: Three-dimensional LSB resulting from saturation of primary instability. (a) Baseline LSB corresponding to primary instability $u_{0,rev}$=8.06% (b) Steady three-dimensional LSB resulting from the saturation of the primary instability. Source: Rodríguez et al. (2021).

In one of the first studies, Alam and Sandham (2000) state that the separation bubble can become globally unstable under certain conditions. When the magnitude of the reverse flow velocity within the separation bubble exceeds 15–20% of the free-stream velocity, absolute instability develops, leading to self-sustaining oscillations in the separated shear layer. Focusing on self-excitation, Rodríguez et al. (2013) study global excitation mechanisms that drive unsteadiness and three-dimensionalisation in an LSB. They establish the presence of two types of instabilities: an absolute K-H instability with a reverse flow of more than 12% giving rise to a global oscillatory behavior, and a centrifugal instability with a reverse flow of more than 7%, promoting three-dimensionalisation of the bubble. Following up on the study, Rodríguez et al. (2021)

use DNS to explore the nonlinear evolution of the primary instability, which results in spanwise three-dimensionality of the mean flow. A schematic of the bubble demonstrating instability saturation is presented in the figure 2.7. Such a three-dimensional evolution deforms the shear layer, which triggers a transition in the absence of incoming external disturbances.

2.6 Classification of pertinent instabilities in an LSB

This section attempts to classify and provide a brief description of the instabilities relevant to this study.

- **Fundamental classification**: This classification is based on how the disturbances propagate in time and space. Absolute instabilities are the disturbances that grow at a fixed point due to flow conditions at that particular point. Once the unstable base state is reached, the flow acts as a self-excited oscillator independent of external excitation. The effects induced by absolute instabilities propagate both upstream and downstream. On the other hand, convective instabilities are instabilities that grow in space and are convected by the flow (Monkewitz, 1990). This is the characteristic instability observed in short LSBs.
- **Primary instability mechanisms**: This classifies mechanisms that amplify the small two-dimensional disturbances. The Tollmein-Schlichting wave is the viscous instability wave that amplifies disturbances in the favorable pressure gradient region (Yarusevych and Kotsonis, 2017). Once the flow reaches the adverse pressure gradient part upstream of separation, inflectional instability activates. This is inviscid and inflectional in nature (Diwan and Ramesh, 2009). Once the separated shear layer has moved sufficiently far from the wall, the KH instability mechanism dominates. After the growth rate of the T-S mode of the attached BL dampens near the separation point, KH mode forms the primary amplification mechanism of the separated shear layer (Alam and Sandham, 2000). This mechanism rapidly amplifies the disturbances (exponential growth) and causes shear layer roll-up and periodic shedding of 2D vortical structures (Boutilier and Yarusevych, 2012).
- **Secondary instability mechanisms**: These instability mechanisms are used to describe how the vortices break down into three-dimensional turbulence in the aft portion of the LSB. In the context of LSB, Marxen et al. (2013) classify these instabilities as either elliptic or hyperbolic. Elliptic instability is active in the core of the spanwise vortices and leads to the initial spanwise deformation of the vortex cores. Hyperbolic Instability is active in the braid region between consecutive vortices. It amplifies disturbances with much smaller spanwise wavelengths, causing rapid disintegration into small-scale turbulence. Moreover, Marxen et al. (2009) establishes the existence of Göertler instabilities in an LSB, which show streamline curvature along with formation of longitudinal vortices.
- **Global or intrinsic Instability**: This type of instability arises from the flow in the separation bubble itself without the existence of external disturbances. A global instability manifests as a stationary centrifugal instability (Marxen et al., 2013). After a peak reverse flow magnitude threshold($\geq$ 7%), spanwise undulation forms in the mean flow of the bubble (Rodríguez et al., 2013). But when the reverse flow inside the bubble exceeds a higher threshold ($\geq$ 16%), a Global Oscillator Instability kicks in, leading to local regions of absolute instability of 2D K-H waves. The bubble deforms differently than before as the inflection point shifts below the zero mass-flux streamwise line, converting it to the KH into an absolute instability (Avanci et al., 2019). On this 3D base flow, a secondary global oscillator instability can form, which features amplified spanwise distortion and

localized pockets of strong reverse flow. This sequence of self-excited instabilities can trigger laminar-turbulent transition without requiring external disturbances.

2.7 Dynamics of Vortex shedding and reattachment

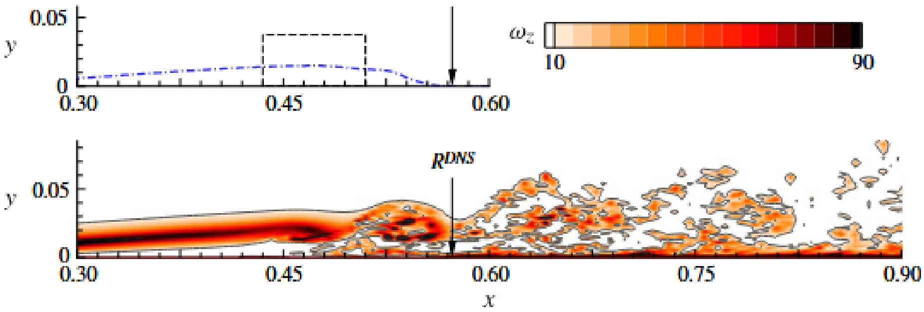

Figure 2.8: Two-dimensional depiction of flow evolution and reattachment. Source: Marxen et al. (2013).

As KH instability dominates and disturbances saturate, the separated shear layer exhibits a two-dimensional coherent vortex roll-up. Although initially two-dimensional tubes, these vortices deform in a spanwise manner due to the acting secondary instabilities. They disintegrate into small-scale turbulence, and a turbulent reattachment boundary layer develops. A schematic highlighting the process in an instantaneous sense is shown in figure 2.8. The effect of external factors on vortex dynamics of an unforced LSB was studied by Lambert and Yarusevych (2019). For a large range of experimental parameters, they find shear layer vortices roll up upstream of the mean transition location and break down in the vicinity of mean reattachment. They further note that the mean size of the LSB decreases with increasing angle of attack, the vortex shedding frequency increases, and the characteristic streamwise wavelength decreases. Additionally, they detect vortex merging events irregularly in the aft portion of the separation bubble. An experimental image sequence highlighting the process is shown in figure 2.9a.

Marxen et al. (2013) elaborates the active secondary instability mechanisms. While elliptic instability acts on vortex cores leading to initial spanwise deformation of the shed vortex cores, hyperbolic instability acts in the braids region connecting consecutive vortices. These instabilities are present when the bubble is forced with both the fundamental and subharmonic frequencies and are indicated by elliptic and hyperbolic streamlines. A visualisation of these instabilities, as adapted from their article, is shown in figure 2.9. Along the same lines, Alam and Sandham (2000) and Rist and Maucher (2002) mention that the presence of secondary absolute instabilities strongly influences the initial spanwise vortex deformations. The interaction of localized instabilities in the reattachment zone further accelerates the transition to turbulence (Marxen and Rist, 2010).

As a first Michelis et al. (2018) propose a model for the observed deformation mechanism. It hypothesizes that the observed deformation of vortex tubes starts in the relative amplification and superposition of the normal and oblique modes well before the separation of the boundary layer. **Hence, an amplification or forcing of a particular mode could change the breakdown characteristics of the vortices.** A sample image of the shed and subsequently deformed vortices is shown in figure 2.10. This wavelength ratio is of particular interest as several experimental studies (Watmuff, 1999; Michelis, 2017; Kurelek et al., 2019; Rodríguez et al., 2021) find a similar

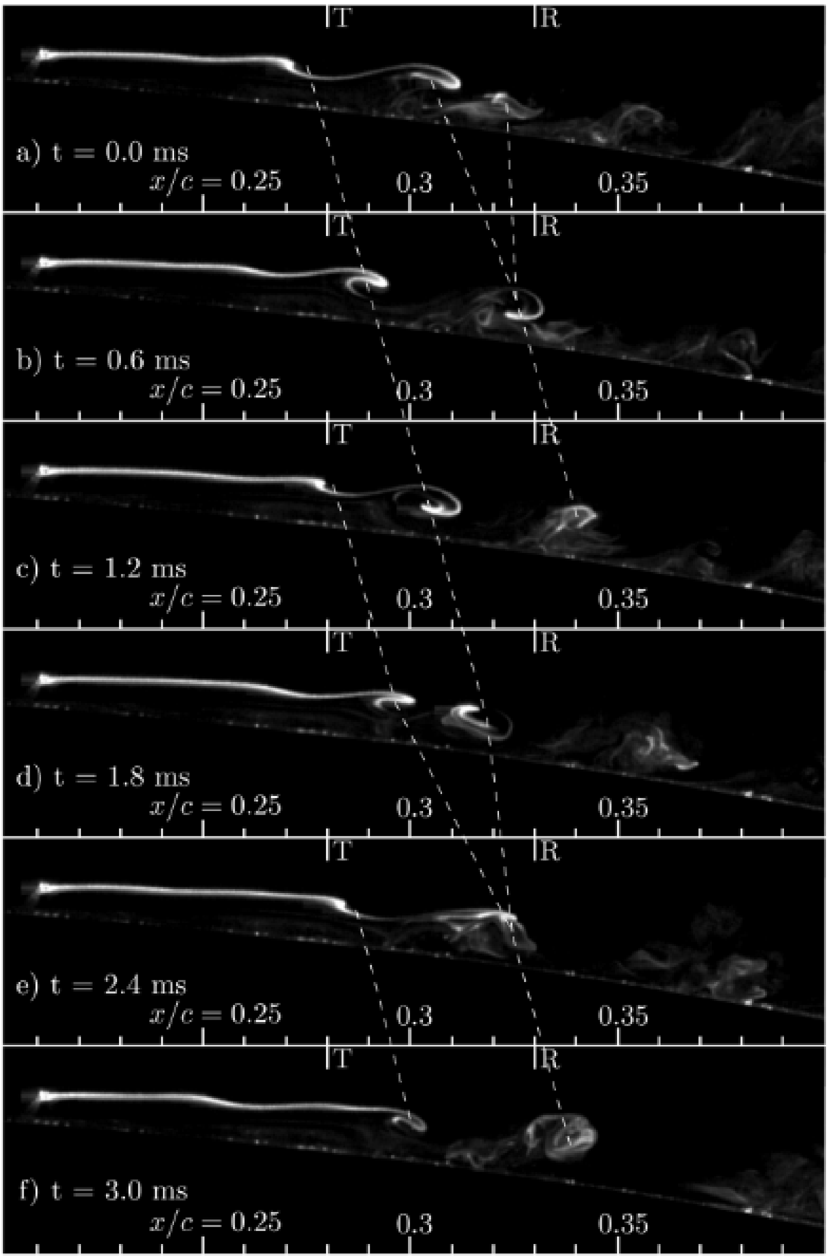

(a) Sequence of separation bubble visualizations (a)–(f) at AOA = 8 degree.

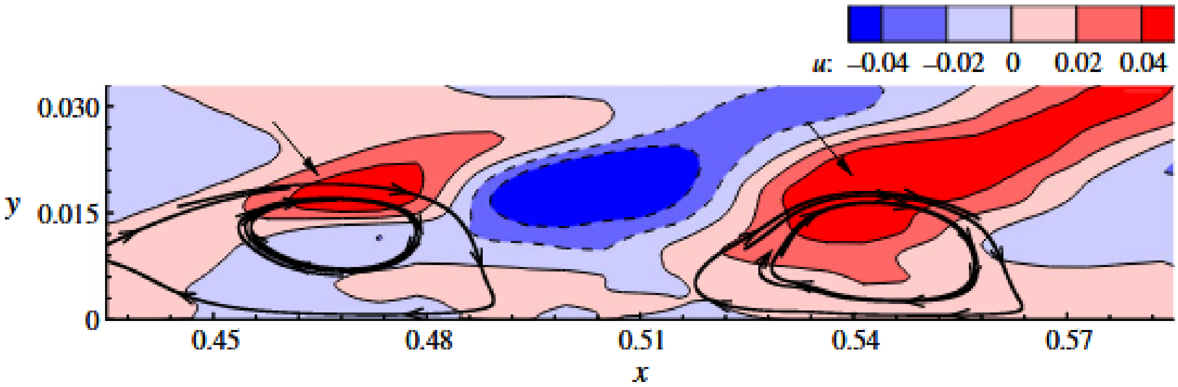

(b) Elliptic streamline vortices downstream of LSB.

Figure 2.9: (a) Vortex merging visualizations. (b) Elliptic secondary instabilities. Sources: Lambert and Yarusevych (2019); Marxen et al. (2013).

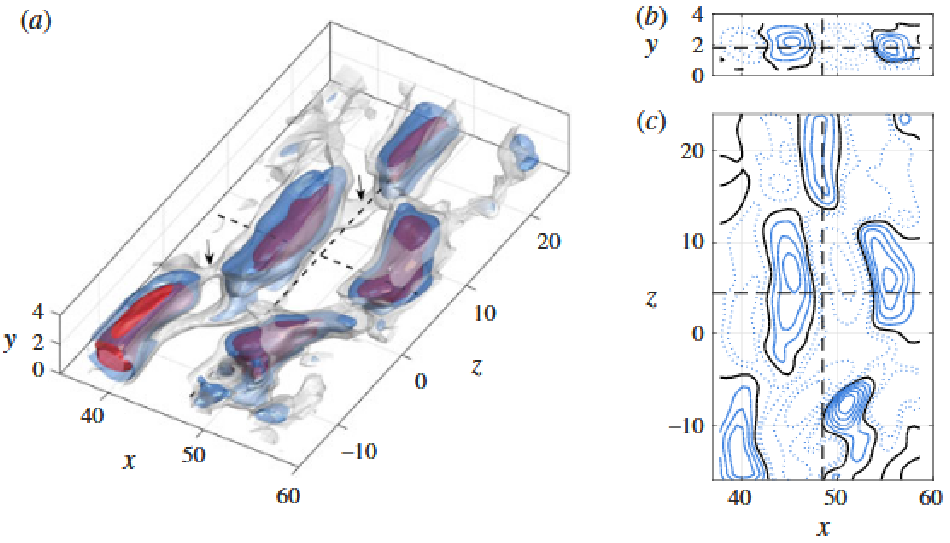

Figure 2.10: Vortex breakdown post-shedding from an LSB. The ratio of wavelength is implied here. Figure Source: Michelis et al. (2018).

ratio. Rodríguez et al. (2021) provide a succinct compilation of relevant studies that demonstrate the same observed ratio, presented here in figure 2.11. This ratio provides a quantitative estimate of the initial breakdown mechanism of the shed vortices from an unforced LSB.

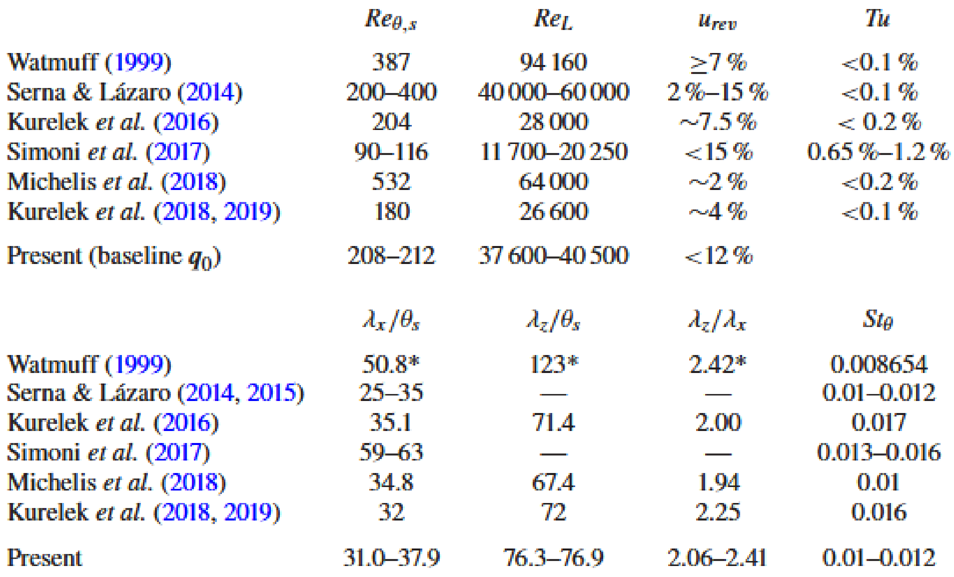

	$Re_{\theta,s}$	Re_L	u_{rev}	Tu
Watmuff (1999)	387	94 160	≥7 %	<0.1 %
Serna & Lázaro (2014)	200–400	40 000–60 000	2 %–15 %	<0.1 %
Kurelek *et al.* (2016)	204	28 000	∼7.5 %	< 0.2 %
Simoni *et al.* (2017)	90–116	11 700–20 250	<15 %	0.65 %–1.2 %
Michelis *et al.* (2018)	532	64 000	∼2 %	<0.2 %
Kurelek *et al.* (2018, 2019)	180	26 600	∼4 %	<0.1 %
Present (baseline q_0)	208–212	37 600–40 500	<12 %	

	λ_x/θ_s	λ_z/θ_s	λ_z/λ_x	St_θ
Watmuff (1999)	50.8*	123*	2.42*	0.008654
Serna & Lázaro (2014, 2015)	25–35	—	—	0.01–0.012
Kurelek *et al.* (2016)	35.1	71.4	2.00	0.017
Simoni *et al.* (2017)	59–63	—	—	0.013–0.016
Michelis *et al.* (2018)	34.8	67.4	1.94	0.01
Kurelek *et al.* (2018, 2019)	32	72	2.25	0.016
Present	31.0–37.9	76.3–76.9	2.06–2.41	0.01–0.012

Figure 2.11: Table showing comparison of various parameters characterising a laminar separation bubble. Source: Rodríguez et al. (2021).

Following the three-dimensional vortex breakdown in the aft of an LSB, the flow reattaches in a time-averaged manner. This entrains momentum from the outer flow to the boundary by the vortices. Hence, the reattachment is primarily three-dimensional, and spanwise reattachment undulations are observed in a time-averaged flow field. The driving factor in this undulatory mean reattachment is the secondary instability-induced breakdown. A sample time-averaged spanwise undulation is shown in figure 2.12(c). Short bubbles tend to exhibit vortex shedding closer to the separation point, resulting in relatively rapid turbulent reattachment, whereas in long bubbles, the shear layer roll-up occurs farther downstream, leading to a state where the flow never fully reattaches within the field of view as observed by Marxen and Henningson (2011). As stated above, the reattachment location itself is dynamic, capable of undergoing temporal variations associated with impulsive disturbances during which reattachment temporarily shifts downstream before returning to its position. This was observed and demonstrated by Michelis et al. (2017).

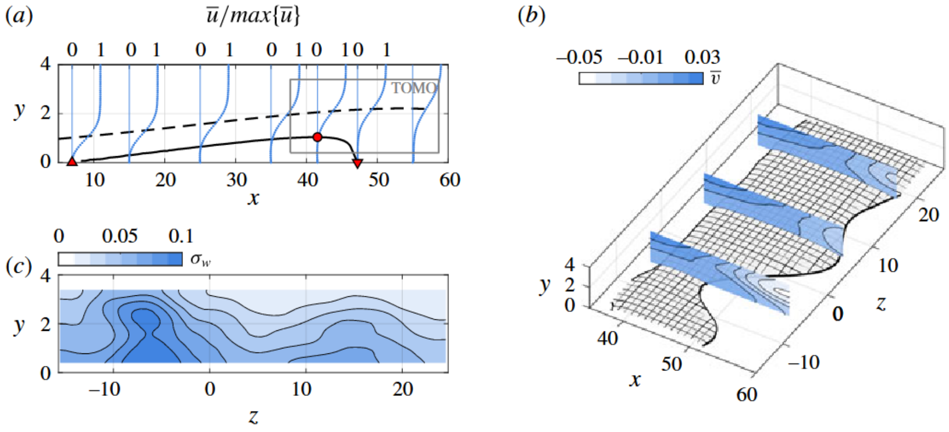

Figure 2.12: (a) Planar PIV time-averaged streamwise velocity profiles. (b) Tomographic PIV time-averaged velocity field. The iso-surface marks the bubble outline. Slices depict wall-normal velocity. (c) Fluctuation of spanwise velocity component. Source: Michelis et al. (2018).

2.8 Impact of external forcing on Mean flow of an LSB

In the context of this study, forcing an LSB refers to introducing independent disturbances in the form of velocity or pressure fluctuations to alter the bubble's topology and vortex breakdown characteristics. Forcing promotes earlier transition and reattachment and reduces the size of the LSB (flow deformation of the LSB). This makes forcing an effective diagnosis method for LSBs. While an unforced LSB's behavior depends on incoming natural disturbances, the behavior of a forced LSB can be studied by varying the frequency, amplitude, and dimensionality of forcing method to modify stability and transition characteristics (Marxen and Henningson, 2011; Yarusevych and Kotsonis, 2017; Michelis, 2017; Kurelek et al., 2023). An external forcing can be applied through a number of methods. Many studies (Yarusevych and Kotsonis, 2017; Michelis, 2017; Michelis et al., 2018) use a dielectric barrier discharge (DBD) plasma actuator. An AC-DBD's capability to introduce controllable disturbances in terms of amplitude and frequency makes it a good choice. The actuator is placed upstream of the separation point. Expanded sections on AC-DBD actuation principles, setup, and quantification of an AC-DBD's effect on flow are presented in sections 4.1.2, 4.2.4 and 4.2.5 respectively.

Marxen and Rist (2010) highlighted the effect of flow deformation. They mention it as a *reduction of the separation region and stabilization of flow with respect to small and linear perturbations*. They term the change in the averaged flow field as *Mean Flow Deformation (MFD)*. The mechanism of MFD can be elaborated as follows. Forcing modulates the vortex shedding, which dictates how the vortices break down. This causes a global change in pressure distribution and influences the growth rate of disturbances in the separated shear layer. This stabilization upstream is an indirect, non-local effect caused by global pressure change. Dellacasagrande et al. (2023) observe a similar relation between disturbance growth rate and LSB size. They observed an increased sensitivity of a larger bubble and decreased sensitivity of shorter LSBs to external flow characteristics such as the free-stream turbulence level.

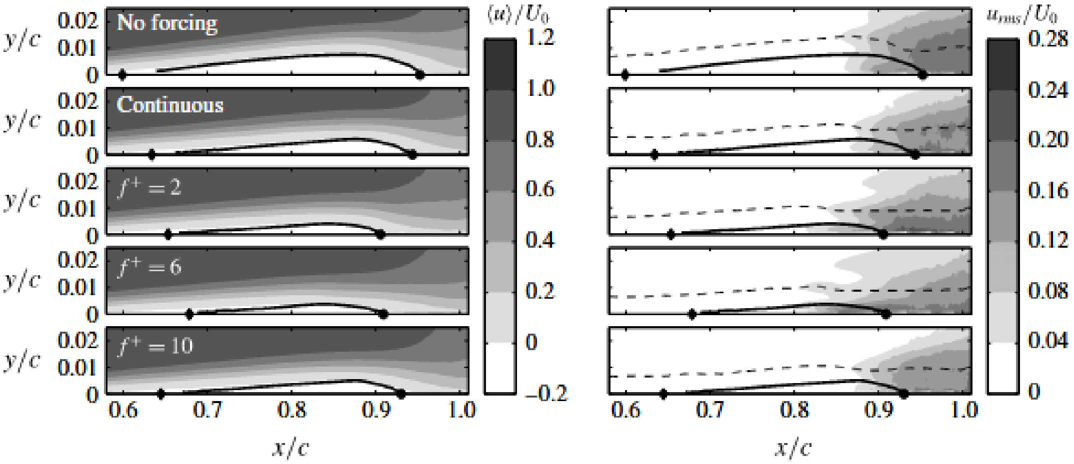

Figure 2.13: Time-averaged and fluctuating streamwise velocity fields for different forcing frequencies. Source: Yarusevych and Kotsonis (2017).

As stated above, the impact of external forcing can be varied by a number of parameters. Since the preferred method of forcing is two-dimensional, the degree of size reduction depends on the frequency and amplitude of forcing. In their experiments, Yarusevych and Kotsonis (2017) find that forcing can reduce the mean bubble length by up to 40%. As the separation and reattachment points move closer together, the maximum height of the bubble reduces. Actuating at the most unstable frequency of the separated shear layer (which is the shedding frequency of the bubble, also termed as the fundamental frequency) produces the largest shrinkage, whereas frequencies far from the unstable frequency are less effective (Yarusevych and Kotsonis, 2017; Marxen and Rist, 2010). This can be inferred from figure 2.13 and figure 2.15, which shows that the most shrunk bubble refers to the most unstable frequency range in PSD and is indeed correlated.

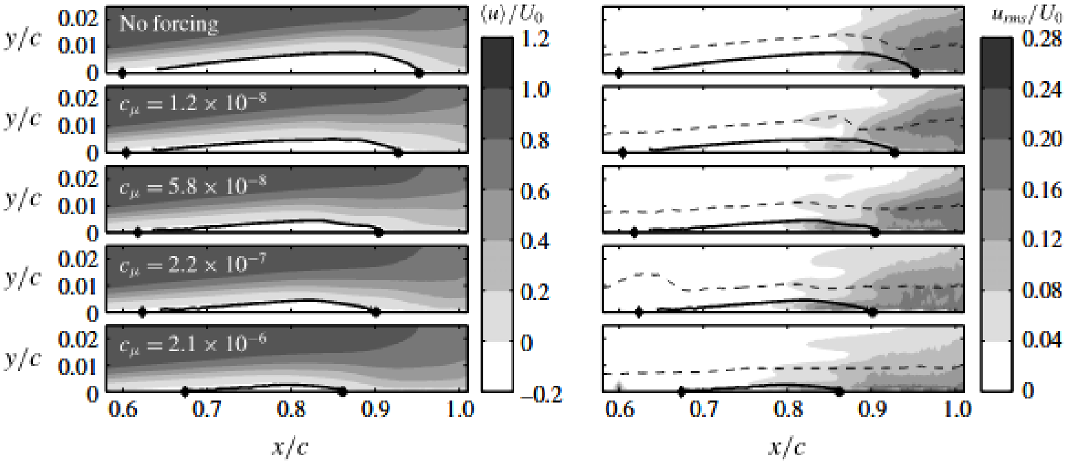

Figure 2.14: Time-averaged and fluctuating streamwise velocity fields for different forcing amplitude. Source: Yarusevych and Kotsonis (2017).

Varying forcing amplitude also affects the LSB topology. Increasing the forcing amplitude above the minimum threshold of naturally occurring amplitude causes the bubble size to decrease exponentially with increase in momentum coefficient (Marxen and Henningson, 2011; Yarusevych and Kotsonis, 2017). Along similar lines, Rist and Augustin (2006), for their two-dimensional study, show that the length of the bubble is roughly proportional to -log A_v, where A_v is the forcing amplitude. Marxen and Henningson (2011) observe that reducing the forcing disturbance below a particular amplitude causes the short bubble to grow continuously, and forms a long bubble. A recent study by Borgmann et al. (2025) demonstrated smaller LSBs as the amplitude of two-dimensional periodic forcing was increased. Through a careful comparison between experiments and DNS study, they emphasized the prevalence of absolute instabilities as described in section 2.6 after a certain amplitude threshold. They state that at high forcing amplitudes, significant spanwise variation of the mean flow was observed (Borgmann et al., 2025). A sample representation of the mean spanwise flow deformation can be seen in figure 2.16. Figures 2.13 and 2.14 demonstrate the effect of forcing frequency and amplitude on the LSB and subsequent breakdown.

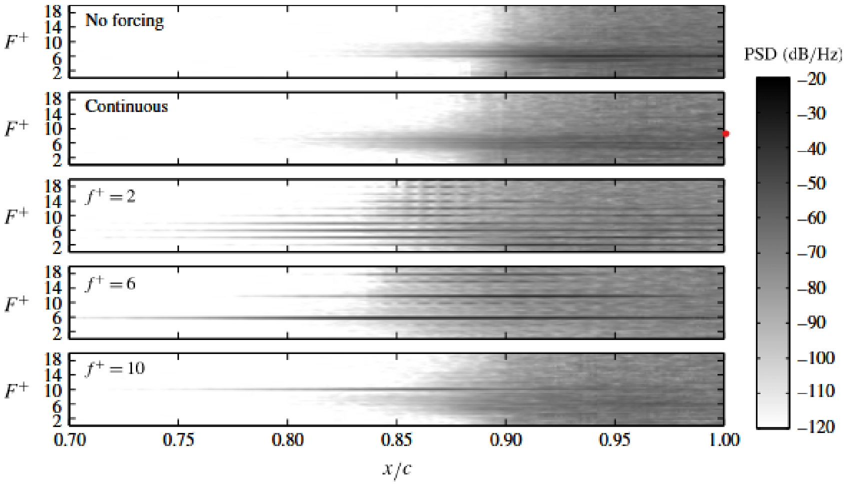

Figure 2.15: Power spectral density (PSD) showing locking of forcing frequency to unstable frequency. Source: Yarusevych and Kotsonis (2017).

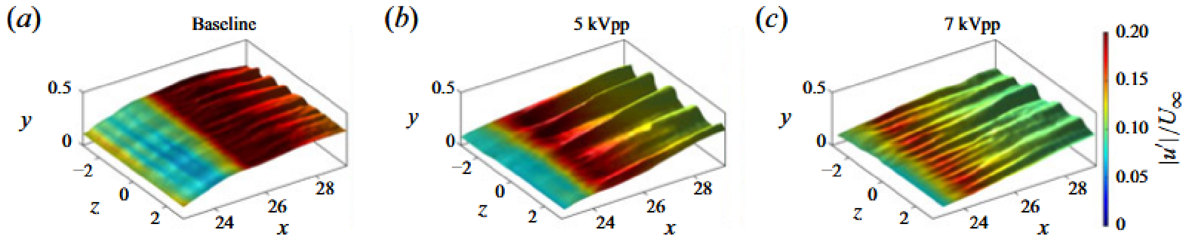

Figure 2.16: Time-average of the reconstructed three-dimensional flow field. Displayed is a plane of constant streamwise velocity, taken at $u/U_\infty = 0.8$ for the baseline case and at $u/U_\infty = 0.87$ for the active flow control (AFC) cases. Source: Borgmann et al. (2025).

In the current study, only the forcing frequency is varied. Hence, some of the forcing types found in the literature and their effects are given below:

- **Periodic forcing**: This forcing scheme can be tuned to the frequency of natural instabilities. Forcing at this frequency amplifies the disturbance exponentially until it reaches large non-linear amplitudes, causing the flow to ”lock on” to the actuation frequency. This locking advances the point of vortex formation significantly upstream, maximizing momentum exchange and causing the early reattachment (Yarusevych and Kotsonis, 2017). Other regimes, such as harmonics and subharmonics of fundamental frequency, less efficiently affect the bubble. This is observed in figure 2.15, which shows heightened amplification of disturbances associated with the unstable frequency band of the bubble. Using periodic forcing, Marxen and Henningson (2011) studied the effect of amplitude. While higher amplitudes produced distinctly shorter bubbles with altered stability characteristics of the mean flow, low amplitudes resulted in behavior closer to the natural unforced state of an LSB.
- **Impulsive forcing**: Michelis et al. (2017) show that a single two-dimensional impulse can trigger a rapid shortening of the bubble as the separation and reattachment points move closer together. Because successive impulses are separated by large time intervals, they perform quasi-steady and phase-averaged analyses. At sufficiently high impulse amplitudes, the LSB is temporarily eliminated, and the subsequent regrowth phase is used to analyse growth rates and the variation of the most unstable frequency with boundary-layer shape factor. As the bubble regrows beyond its original length and vortex shedding temporarily ceases. Since the recovery phase is driven only by the constant natural disturbance amplitude reacting to the changing stability characteristics (MFD), it confirms that bursting and flapping are driven by altered stability characteristics due to fluctuations in incoming perturbations influencing the bubble topology.

2.9 Impact of external forcing on the vortex dynamics of an LSB

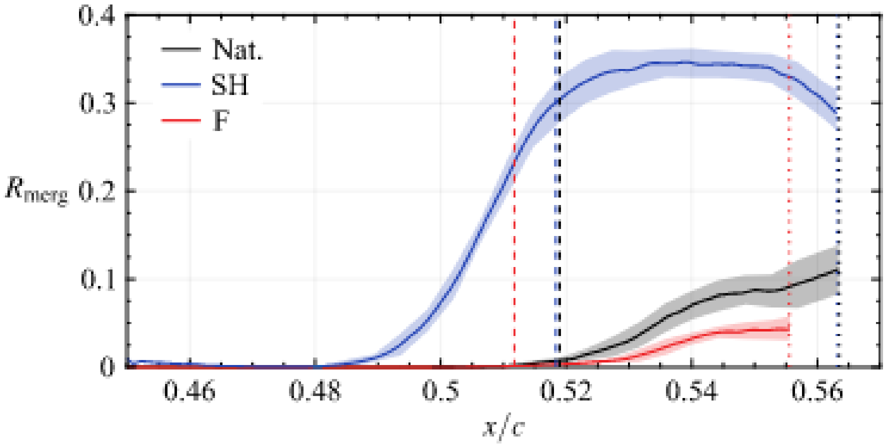

Figure 2.17: Ratio of detected merged structures to total number of shed primary structures. Source: Kurelek et al. (2019).

While the above section describes and discusses the effect of forcing on the streamwise variation of an LSB, and time-averaged LSB topology, this section focuses on the effect of forcing on the span of the reattachment region of an LSB. With forcing, the vortex breakdown characteristics change. The transition process changes due to artificial forcing altering the disturbance growth rates, which play a major role in determining the shape and dynamics of spanwise reattachment past the LSB. An important aspect to highlight is that the vortices always shed from an LSB at the natural/fundamental frequency, irrespective of the forcing frequency. Michelis et al. (2017) in their study highlight that when a natural LSB is forced with an impulsive broadband frequency, the K-H mechanism selectively amplifies the disturbances at fundamental frequencies from the broadband input, and the vortices shed are at fundamental frequency. This is in line with the observation by Marxen et al. (2013) who state that shear-layer vortices are generated at the natural frequency or its subharmonics with periodic excitation.

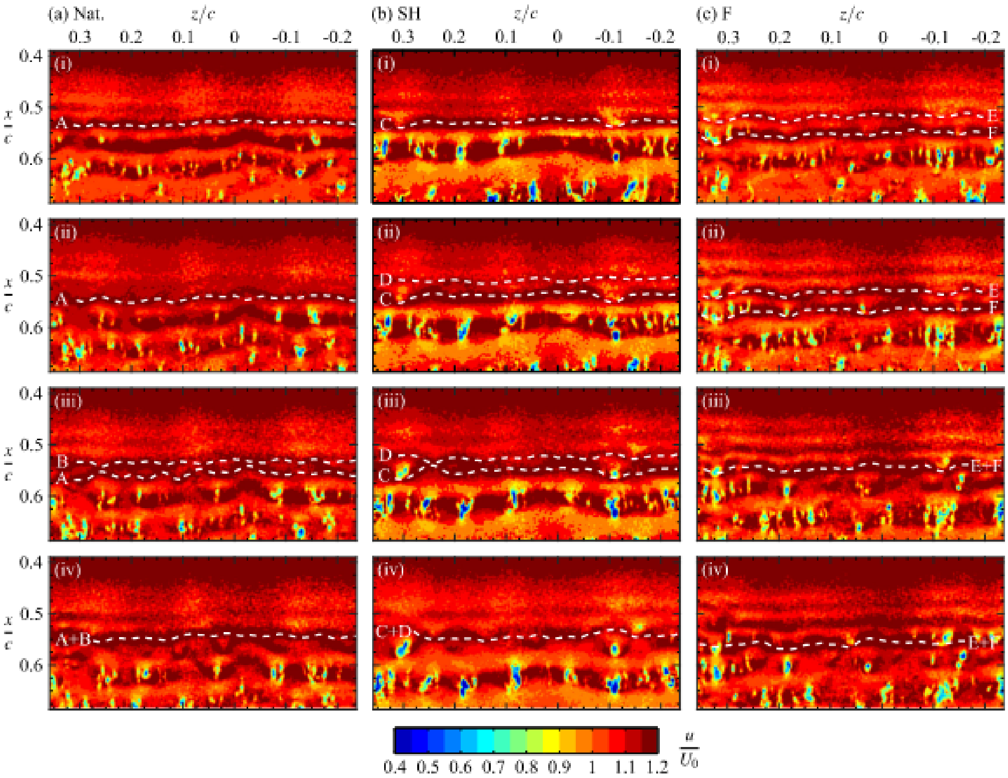

Figure 2.18: Sequences of instantaneous streamwise velocity contours. Flow is from top to bottom. Dashed lines indicate smoothed spline fits to the center of selected structures (labeled A–F). Source: Kurelek et al. (2019).

In their study, Kurelek et al. (2019) force the bubble at subharmonic and harmonic frequencies. They find the shedding frequency to be the natural frequency in both cases. They observe vortex merging, where two consecutively shed vortices co-rotate and merge, a phenomenon observed for both harmonic and subharmonic forcing frequencies. Kurelek et al. (2016) mention that the shed vortices slow down as they merge near the mean transition, reach a minimum velocity at this merging center, and then begin to increase again as the reattached turbulent boundary layer redevelops. They notice a higher merging rate when the forcing frequency is subharmonic as compared to harmonic forcing. They attribute this increase to a higher amplification and saturation of the subharmonic frequency modes. However, the bubble size remains similar, which is attributed to the fact that equal momentum is entrained back both by merged (with a lower frequency of entrainment) in the subharmonic forcing case, as well as the unmerged vortices in the harmonic forcing case. The ratio and extent of merged structures for different forcing frequencies can be seen in figure 2.17. Using time-resolved experiments, they confirm that vortex merging occurs in a spanwise non-uniform manner and is intrinsically linked to the spanwise undulations of the vortex filaments. The sequence of events can be found in figure 2.18. In another study to better understand the initial vortex undulation, Kurelek et al. (2021) state that the patterns observed in spanwise velocity fluctuations confirm the association of spanwise undulations in the vortex filaments with wall-normal deformations, with the filaments tilting away from the wall at locations where they surge forward in the streamwise direction. This peak and valley structure is observed in figure 2.18.

Using figure 2.19, (Michelis et al., 2018) showed that in the aft part of an unforced bubble, the shed vortices deform along their span. By doing stability analysis using the data from both PIV and numerical solver, they relate the observed deformation to the growth of oblique modes with *highest amplification rates associated with oblique angles below approximately 30* °. They further state that the degree of spanwise deformation depends on the relative amplitude of normal and oblique modes. Two-dimensional forcing significantly promotes the normal mode (using a spanwise-uniform impulse emitted through an AC-DBD plasma actuator), and the resulting shed vortices are spanwise-coherent, taking a longer time to deform (figure 2.20). After the initial forced shedding, the vortex shedding in the aft part ceases entirely, and the bubble elongates temporarily.

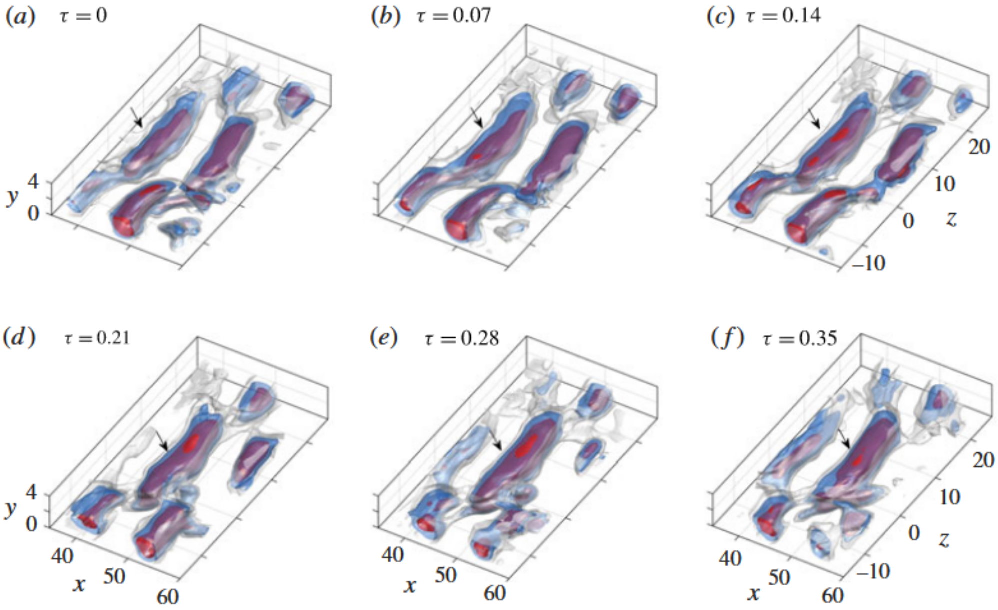

Figure 2.19: Unforced bubble instantaneous Q-criterion snapshot. Source: Michelis et al. (2018).

While that was the observation in impulsive forcing allowing full bubble recovery, when forced at fundamental forcing frequency, the vortex shedding locks and the vortices shed are more coherent and convect farther downstream before they break down (Michelis et al., 2018). However, at frequencies much below the natural frequency, the shear layer does not lock onto excitation, and vortex shedding is rather modulated. A sample illustration showing the impact of forcing frequency can be found in figure 2.21 for different forcing frequencies. They conclude by attributing the deformations to the interaction between different constituent modes of the incoming boundary and shear layer stability characteristics. **This establishes a fact that the LSB merely acts**

as an amplifier, which is also stated by other studies (Borgmann et al., 2021; Michelis et al., 2018; Kurelek, 2021).

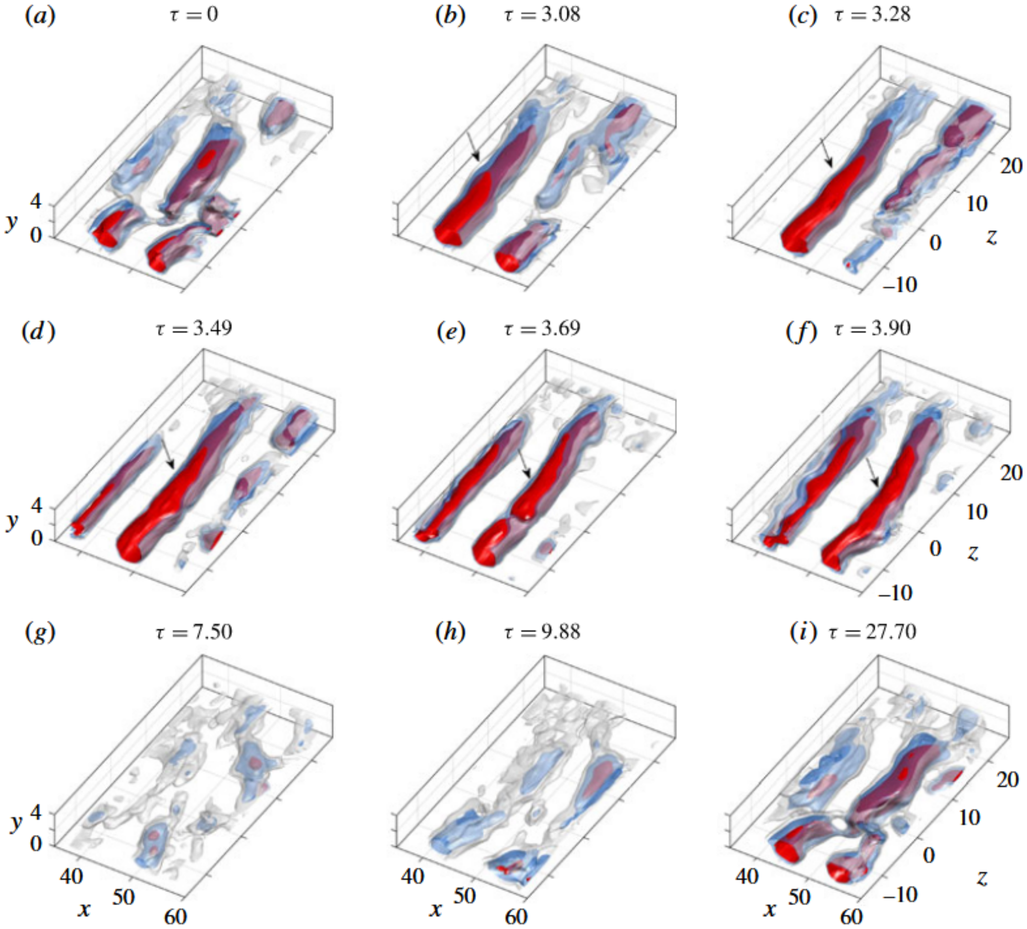

Figure 2.20: Forced bubble instantaneous Q-criterion snapshot. Source: Michelis et al. (2018).

Apart from experiments, DNS studies investigating the spanwise deformation of the shed vortices under forcing also shed light on the breakdown dynamics under controlled conditions. A study by Hosseinverdi and Fasel (2018) confirmed the ability of strong spanwise-coherent vortical structures generated at intermediate forcing amplitudes to reattach the flow before turbulent breakdown. Results by Borgmann et al. (2025) also provide similar insights.

A general metric to quantify the breakdown mechanism is the spanwise to streamwise wavelength ratio. This was discussed in brief in section 2.7. In a time-resolved 3D-PIV study. Kurelek (2021), show that the ratio of spanwise-to-streamwise wavelength, $\langle \lambda_z/\lambda_x \rangle$, for the spanwise vortex deformations ranged between 1 and 7. Since this observation is along the lines of previous studies (table 2.11), it questions the relation of the deformation mechanism with an underlying instability mechanism. This motivated a study by Kurelek et al. (2023) where they used a three-dimensional forcing technique. They superposed disturbances from sequentially arranged AC-DBD plasma actuators to produce controlled disturbances at desired spanwise wavelengths.

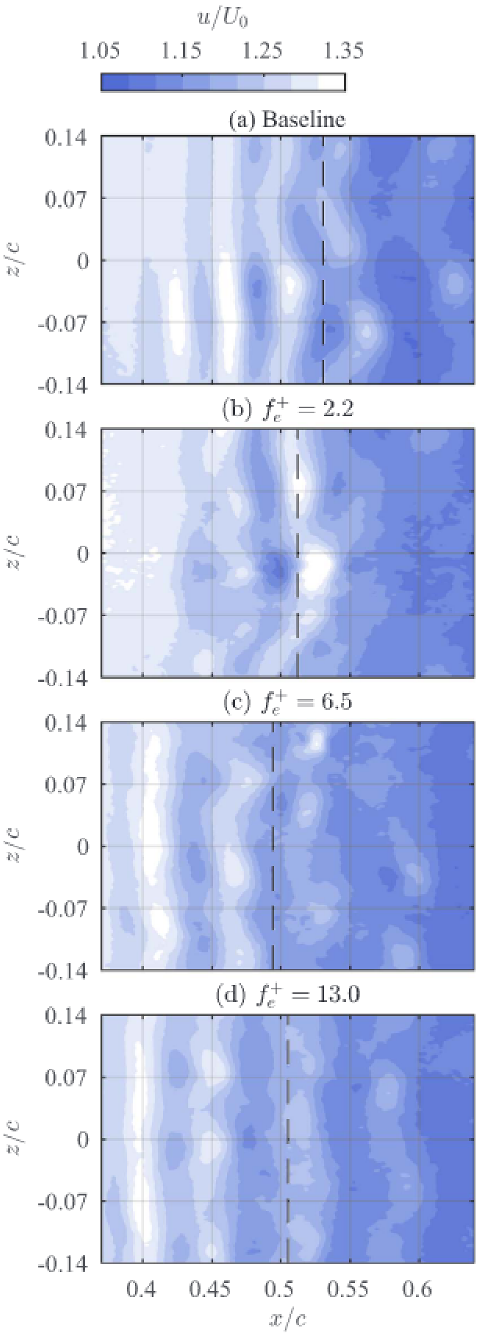

Figure 2.21: Impact of forcing frequency on spanwise deformation of shed structures in a streamwise velocity field. Source: Michelis et al. (2018).

While the previous studies have statistically quantified the dominant spanwise and streamwise wavelength to quantify the breakdown mechanism, none used stability analysis to quantify and compare the spanwise wavenumbers possible on the periodic shed vortex tube as a base flow. Borgmann et al. (2022) conducted secondary instability analysis (SIA) by using Linearised Navier-Stokes equations (LNSE) to obtain insight into the non-linear stages of transition and to predict the onset and initial growth of the unstable three-dimensional (3D) disturbances in the time-periodic shed vortex tubes susceptible to secondary instabilities. For an intermediate forcing amplitude, the flow was predicted to become unstable over a restricted range of spanwise wavenumbers. This finding was in complete agreement with the dominant spanwise wave-

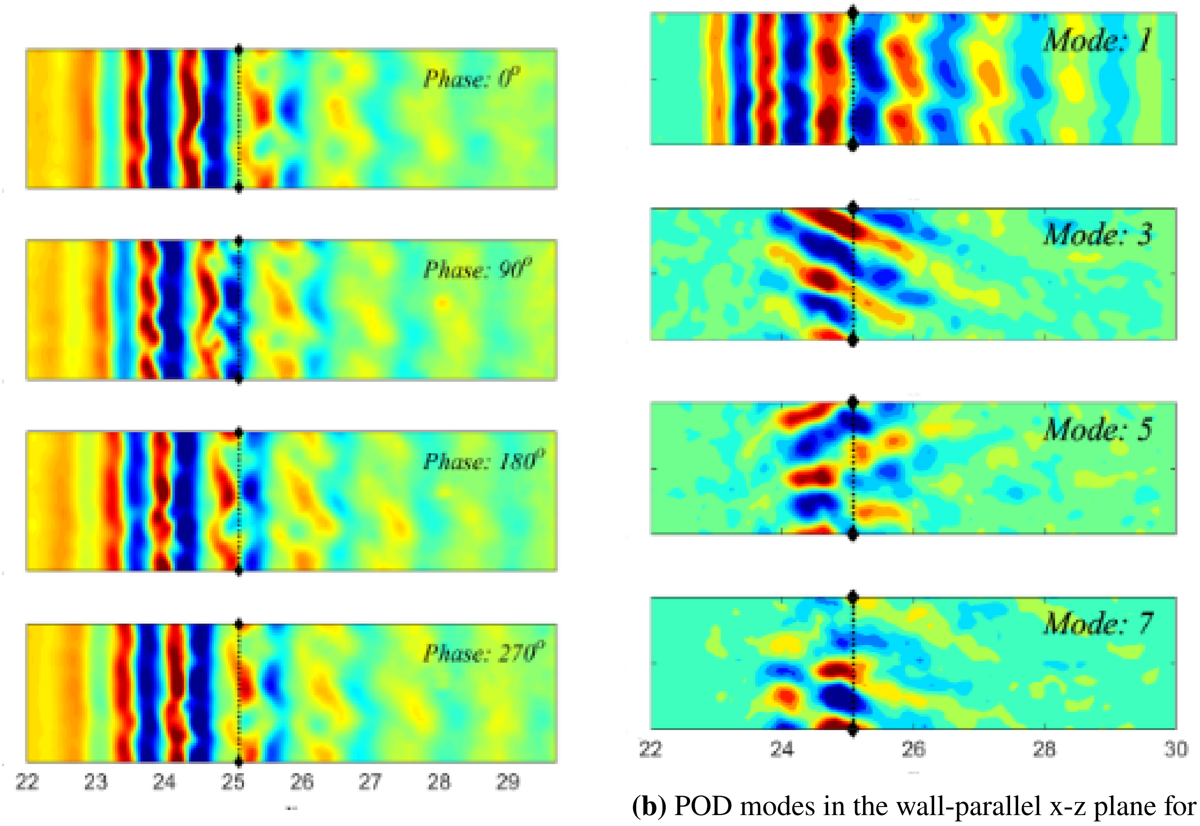

(a) Phase averaged v-velocity (wall-normal) from experiment in the wall-parallel x-z plane for intermediate amplitude.

(b) POD modes in the wall-parallel x-z plane for intermediate amplitude. Shown are contours of the u component of most dominant eigenfunctions.

Figure 2.22: Source: Borgmann et al. (2022).

length identified from Proper Orthogonal Decomposition (POD) of experimental data and the flow structures obtained from the corresponding Direct Numerical Simulations (DNS). Other interesting observations included a staggered breakdown pattern in the breakdown region, indicating interaction of oblique and normal modes, and an increase in spanwise wavelength in the phase-averaged velocity field as the vortices convect downstream. A representation of the same can be found in figure 2.22.

3

Research plan

While seminal works by Gaster (1967) and Horton (1968) laid insights into the LSB topology and behavior, experimental studies (Yarusevych and Kotsonis, 2017; Michelis et al., 2017, 2018; Borgmann et al., 2021, 2025) and numerical studies (Alam and Sandham, 2000; Marxen and Rist, 2010; Marxen and Henningson, 2011; Marxen et al., 2013; Hosseinverdi and Fasel, 2018) provide valuable insights on how external forcing affects LSB topology and vortex breakdown characteristics. These studies investigated the effect of external forcing on LSB and its vortex dynamics by varying the parameters of forcing, which vary the pattern of momentum injection into the boundary layer. Depending on how the momentum is imparted into the boundary layer through these parameters, the LSB topology and breakdown characteristics change. In the present work, an AC-DBD plasma actuator is employed, for which three parameters can be tuned: the forcing frequency, the forcing amplitude, and the dimensionality of the forcing (two- or three-dimensional). Among these control parameters, the forcing frequency plays a central role, and the effect of its variation on LSB topology and breakdown is the focus of this study.

While several studies (Michelis et al., 2017; Yarusevych and Kotsonis, 2017; Borgmann et al., 2022, 2025) have examined impulsive and fundamental forcing and their harmonics, no study has addressed how periodic forcing with an actuation-frequency range between the impulsive regime and the harmonics of the natural frequency influences LSB topology and breakdown characteristics. Accordingly, investigating the effect of this forcing-frequency range on LSB topology and breakdown characteristics forms the premise of this thesis. Using appropriate methodologies and analysis techniques, this thesis aims to bridge that gap.

3.1 Research questions

Two research questions are posed that would be helpful to address the objective, posed in section 1. The brief description below each research question provides a line of thought driving the research question and an analysis direction to address the question.

1. How does the LSB topology vary with a two-dimensional AC-DBD actuation frequency ranging from impulsive to fundamental forcing frequency?

   Line of thought: As the frequency of periodic actuation increases, the recovery time of the bubble decreases. A bubble actuated impulsively is expected to have no time-averaged variation in topology and a bubble actuated at a higher forcing frequency is expected to show larger time-averaged variation in topology, i.e a have smaller size.

Intended investigation direction: This will be investigated using quantitative measures such as LSB size (length, height, or area), standard deviation of the flow field, and boundary layer integral quantities.

2. How does the 3D breakdown of the shed vortex, quantified in terms of wavelengths of coherent structures in streamwise and spanwise directions, vary over the range of actuation frequency?

   Line of thought: A constant amplitude forcing frequency changes the breakdown by promoting or inhibiting instability modes, leading to different breakdown characteristics. The different breakdown characteristics would be indicated by a change in wavelengths.

   Intended investigation direction: This will be investigated by comparing the variation of spanwise and streamwise wavelengths of the forced wave packet, at different streamwise locations, to those of an unforced bubble as a baseline.

4

Methodology

This chapter describes the experimental methodology employed to address the research questions posed in Section 3.1. The measurement and actuation techniques used in this study are low-speed planar Particle Image Velocimetry (PIV) for quantification of the flow field and an Alternating Current–Dielectric Barrier Discharge (AC-DBD) plasma actuator for introducing disturbances into the flow. Subsequently, the characteristics of the wind-tunnel facility, the airfoil model, and optical arrangements used to obtain wall-normal and wall-parallel views of the laminar separation bubble topology and breakdown are also described.

4.1 Experimental Techniques

4.1.1 Particle Image Velocimetry

PIV is selected as the primary flow visualisation and measurement technique. The choice is motivated by studying relevant literature (Watmuff, 1999; Boutilier and Yarusevych, 2012) that employ different experimental techniques. In the current context, separation bubbles are extremely sensitive to disturbances in the flow field, and those disturbances can be amplified by using intrusive measurement techniques. This highlights a need for proper models, free-stream conditions, and minimally invasive methods. PIV meets these requirements: it is optical and non-intrusive, provides quantitative velocity fields at high spatial resolution, and has been extensively validated and is widely used. Apt PIV techniques can be used to obtain two-or three-dimensional velocity vectors in a plane or volume (planar, stereoscopic, or tomographic PIV). An overview of applications and explanations can be found in the recent work of Raffel et al. (2018).

PIV operates on the principle of tracking a set of tracer particles in the flow, which are illuminated twice in rapid succession, and estimates their displacement by a cross-correlation to obtain velocity. The tracer particles are seeded in the flow, whose convection represents fluid motion. The tracer particles should be small enough to faithfully follow the flow but large enough to scatter sufficient light for detection by digital cameras. The mass density of the seeding particle close to the working fluid becomes increasingly important as particle diameter increases. Hence, the seeding density should be optimal and uniform across the measurement region. For low-speed aerodynamics in air, a water–glycol vapor mixture with a particle diameter of approximately 1 μm is most commonly used.

Particles in the measurement region are illuminated instantaneously by a high-powered double-pulsed laser beam. Usually, a green light of wavelength λ = 532 nm is used. The emitted laser beam can be converted into a laser sheet for planar and stereoscopic PIV using cylindrical and spherical lenses and directed into the measurement plane using mirrors. Two laser cavities shoot in rapid succession so that displacement between the two instances is captured, and care is taken that the intensity is homogeneous and uniform between pulses. Additionally, the duration of illumination by the laser and exposure of the flow field onto the camera sensor play a major role. Short pulse durations and exposures freeze particles in captured images and avoid streaking.

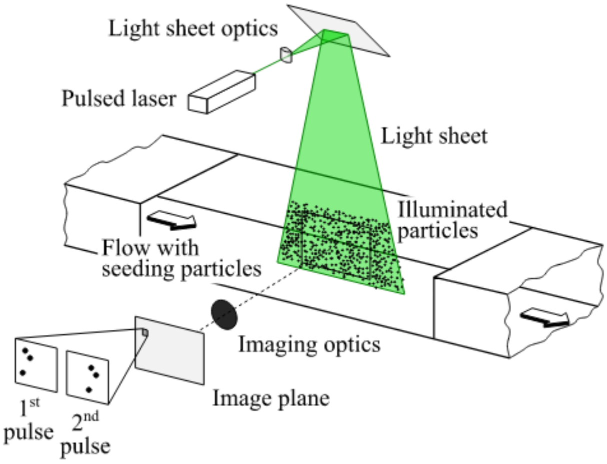

Figure 4.1: Schematic of a sample PIV setup. Source: Raffel et al. (2018).

The frequency of acquisition plays a crucial role. It can range from the order of 10 Hz to the order of 10 MHz. While the low acquisition frequency is sufficient to capture the flow field, a high acquisition frequency enables capturing the time-resolved details of a flow. Since the current study deals with phase-averaged measurements that capture the convection of the actuated wave packet, a low frequency of acquisition is deemed suitable. While some studies have also chosen time-resolved PIV, it's deemed not necessary for the current study since it's a complex setup and requires complex post-processing techniques. Hence, low-speed planar PIV is chosen as a suitable flow visualization technique for the current study. A schematic of the sample PIV setup is given in figure 4.1.

4.1.2 Alternating Current - Dielectric Barrier Discharge actuator

The actuator used for the experiments is the Alternating Current-Dielectric Barrier Discharge (AC-DBD). As the name suggests, plasma actuators are electric devices that generate a body force on the surrounding air producing a weak, nearly wall-parallel jet. They are created by applying an electric field across a gas volume using opposing electrodes driven by an AC voltage; when the breakdown voltage is exceeded, an electrical breakdown occurs, and plasma forms. In flow-control applications, an asymmetric electrode arrangement separated by a dielectric barrier (dielectric barrier discharge, DBD) is commonly used. Under AC operation, heavy ions such as O^+ and N^+ oscillate between the electrodes and transfer momentum to the surrounding air through collisions; because of the electrode asymmetry and the dielectric barrier, unequal momentum is imparted during alternating half-cycles, producing a net body force directed from the high-voltage to the ground electrode, as seen in the figure 4.2. Ideally, the height of the barrier, in order of μm, is much less than the height of the region of interest, a laminar separation bubble. It has been established in previous studies that the dimensions of the barrier have no significant effect on the dynamics of the bubble (Yarusevych and Kotsonis, 2017; Michelis et al., 2017; Kurelek et al., 2019).

In LSB studies, AC-DBD plasma actuators have been used to introduce disturbances, initially introduced as T-S waves, that later amplify through the KH instability of the separated shear layer. Both span-uniform (2D) forcing and span-modulated (3D) forcing have been used; in the latter, two actuators arranged in succession and operated with relative phase delays and ground-electrode gaps impose 3D disturbances (Kurelek et al., 2023). The AC-DBD actuation, being an active flow control method, can also be actuated at different frequencies and amplitudes to mimic different experimental conditions and their effect on bubble dynamics.

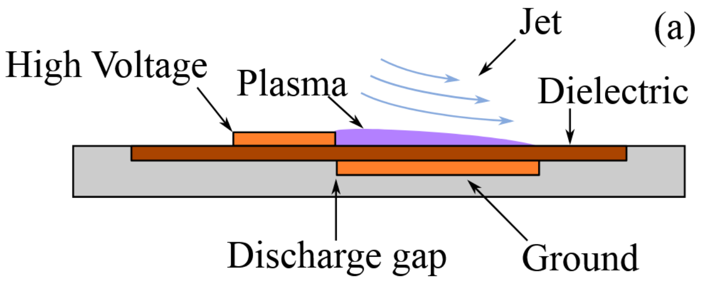

Figure 4.2: Cross-section schematic of the AC-DBD actuator. Source: Michelis et al. (2017).

4.2 Experimental Setup

4.2.1 Experimental Facility

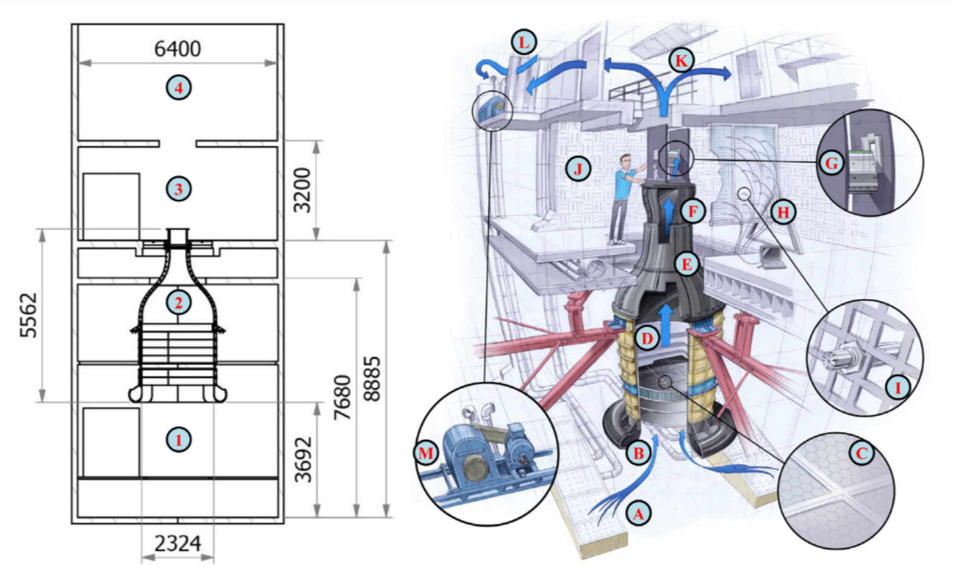

(a)

(b)

Figure 4.3: Dissected view of Anechoic tunnel at Low Speed Laboratory. A detailed description of the labeling can be found in the source. Source: Merino-Martínez et al. (2020).

The experiments were conducted in the Anechoic tunnel (A-Tunnel) at the Low Speed Laboratory of the Delft University of Technology. It is an open-jet, closed-circuit, vertical wind tunnel spread over four floors and consists of several sections. Starting with the initial section, the inflow was conditioned using a honeycomb flow straightener, followed by anti-turbulent screens arranged sequentially. A fan system located on the fourth floor in the return chamber provided the driving force for the tunnel. The velocity was controlled by adjusting the fan's rotational speed using software on the A-Tunnel control PC. The open-jet configuration was advantageous and contributed to lower background noise levels compared to closed-section tunnels. This ensured flow conditions necessary for the intended study of laminar separation bubbles. A dissected view of the A-tunnel can be found in figure 4.3.

While the vertical inflow tunnel (denoted by section F in figure 4.3) has a diameter of 0.6 m, the facility allows use of interchangeable nozzles. For this study, the Delft 40 × 70 nozzle was chosen. The nozzle has a physical dimension of 0.4 m × 0.7 m with a height of 0.72 m and a contraction ratio of 15:1 (Merino-Martínez et al., 2020). Together, the A-tunnel and the nozzle configured stable flow conditions essential for the formation of an LSB. Because of these controlled flow conditions, it is also possible to specifically segregate the effect of only plasma actuation, as the incoming turbulence and disturbances are negligible.

4.2.2 Airfoil and test-section

The NACA 0018 airfoil model has been used for this study, and its aerodynamic characteristics are well established. It has a chord length c of 0.2 m and a span length of 0.4 m. Thus, the airfoil spans the entire width of the test section. The model is equipped with 16 static pressure taps on both the pressure and suction surfaces, which are distributed diagonally so that there is minimal influence from any possible streamwise turbulent streaks. This arrangement also facilitates obtaining pressure variation along a bubble along the streamwise direction for different forcing frequencies. The airfoil is bolted into a specific frame (a plexiglass frame) within the test section, and it also serves as an electrical ground for the plasma actuator.

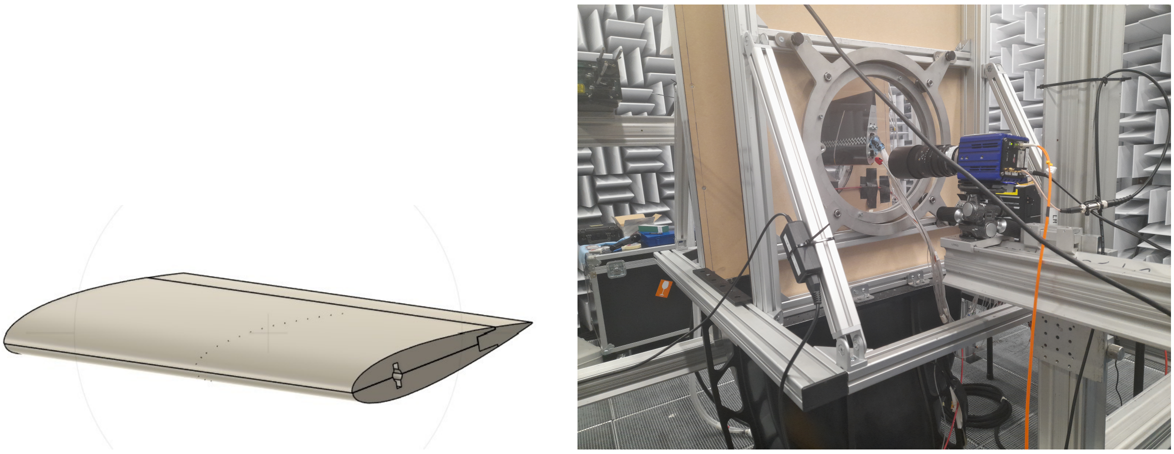

(a) Isometric view of the leading edge showing pressure taps.

(b) Airfoil set-up in the test section with the wall mount flush.

Figure 4.4: Model and facility visualisations: (a) leading-edge detail with pressure taps; (b) test-section installation.

A primary technical issue that was discovered during data processing was a slight misalignment at the leading edge where the two airfoil pieces joined. This misalignment created a step that led to an uneven boundary layer along the span and hence an increase in perturbation levels on one side.

A wall-mounted flush test section was placed over the nozzle. It had dimensions of 1.2 m × 7 m × 4 m, which was fit with a flush-mounted plexiglass window. The plexiglass window enabled optical access through the wall-normal plane, and the window was oriented normal to the airfoil chord, thereby enabling PIV measurements. Additionally, the airfoil's geometric angle of attack was adjusted at 7.1 degree manually, which ensured formation of a laminar separation bubble on the suction surface of the airfoil. A sample isometric view of the airfoil and setup is presented in the figure 4.4.

4.2.3 Low speed planar PIV and Setup

The working principle was established in section 4.1.1. To study the flow development, two mutually perpendicular planes were used: a wall-normal (side-view) plane to capture the bubble behavior and vortex shedding, and a wall-parallel (top-view) plane to reveal spanwise development of actuated wavepackets leading to breakdown. In terms of equipment, both planes use the same laser, PIV cameras, and plasma actuator. However, the camera and laser orientation are changed when capturing the flow field. This change in orientation is shown in a schematic of the setup in figure 4.5.

Planar PIV configurations use a sheet of laser beam of 1 mm thickness for both the Wall-normal and the Wall-parallel configurations separately. The sheets are obtained using a combination of spherical and cylindrical lenses with cameras directed normal to the illuminated plane. The illuminated plane is focused and calibrated using a calibration target on the airfoil negative in the wall normal plane, and a calibration plate in the wall parallel plane. This is done before the seeding is introduced and the flow is imaged. The camera and laser system are synchronized for the same acquisition frequency.

Following this initial setup, particle seeding is introduced into the flow, and paired images are captured at two successive time instances to allow noticeable particle movement. This particle movement is quantified with an optimized interrogation window to obtain a vector field. Care is taken such that the time gap for a pair of image acquisitions corresponds to a limit in particle movement Δx. This is normally taken to be the time for the seeded particles to travel 25% of the interrogation window size (the quarter rule). The estimation of particle displacement using the Particle Image Velocimetry (PIV) algorithm starts by dividing the pair of images into small grids called interrogation windows of m×n pixels. For the pair of images, corresponding windows are analyzed through cross-correlation, adjusting for various overlap values to enhance accuracy through vector spacing. This cross-correlation produces a two-dimensional map with a peak indicating the displacement that maximizes similarity between the windows. This peak correlates to the average linear motion of particles within the window, allowing for the calculation of a local two-dimensional velocity vector, given that the time interval Δt between images is known. This procedure is reiterated across all windows and throughout all captured double-paired images to compile a series of velocity fields.

While the above section describes the general process of cross correlation, some additional factors have to be taken into account when calculating the velocity field. Since the field of view in the physical space is calibrated and is mapped onto the sensor of the camera, it introduces a magnification factor (M_f). This factor is taken into account when calculating the velocity obtained from cross-correlation.

$$\vec{v} = \frac{1}{M_f} \frac{\Delta\vec{x}}{\Delta t}$$

where v is the velocity, M_f is the magnification factor, Δx is the distance traveled by the particle and, Δt is the time difference between two frames.

(a) Wall-normal plane (Side View)

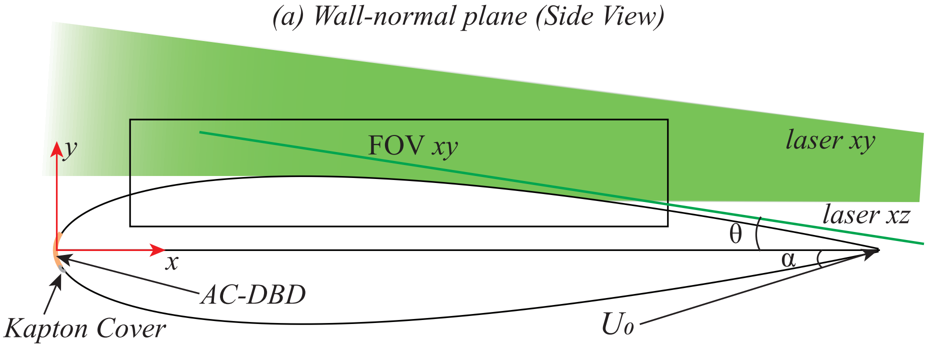

(b) Wall-parallel plane (Top View)

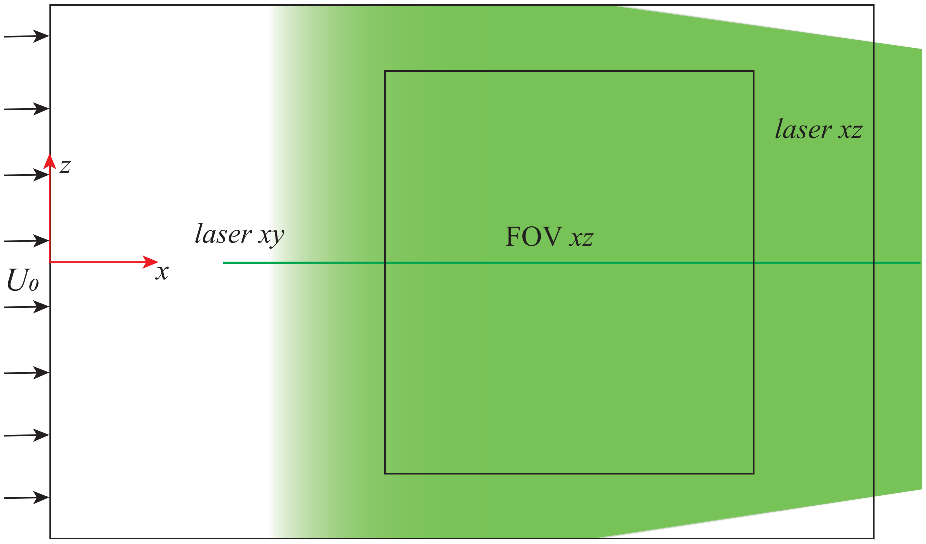

Figure 4.5: Schematic of the Wall-normal and Wall-parallel experimental setup planes.

A brief description of the equipment used will be given. This includes the placement of cameras and laser emitter. For illuminating the measurement planes, a Quantel Evergreen EV00200 series Double-pulse Nd:YAG laser system at a wavelength of 532 nm, with a maximum repetition rate of 15 Hz and average energy of 200 mJ per pulse, was used. The laser sheet in the wall-normal plane was formed using a 50% power collimated beam, whereas the laser sheet in the wall-parallel plane was formed using a 60% power collimated beam. Following the emission as a cylindrical beam, it passed through spherical and cylindrical lenses and a mirror to form a laser sheet of 1 mm in both planes. The unavailability of knife edges prevented further focusing of sheet thickness in both planes. This could have helped mitigate any projected vectors due to in-plane movement. Seeding was generated and provided by a SAFEX smoke generator on the fourth storey of the building, producing 1 μmdroplets of a fresh water–glycol mixture.

A LaVision Imager sCMOS CLHS camera with a 12-bit CMOS sensor imaged the illuminated region for both planes. The camera had an f#=5.6 in the wall normal plane. The streamwise extent of the field of view was set such that the vortex-shedding region is captured. Both the cameras have a sensor of 2560 ×2160 pixels. For the wall normal plane, the field of view was cropped to 137×47 mm, yielding magnification 0.12, whereas for the wall parallel plane, the field of view was cropped to 119×140 mm, yielding magnification 0.11. Reflections from the metallic framework were prevented by coating the airfoil with black matte paint and covering the image background with a matte vinyl sheet.

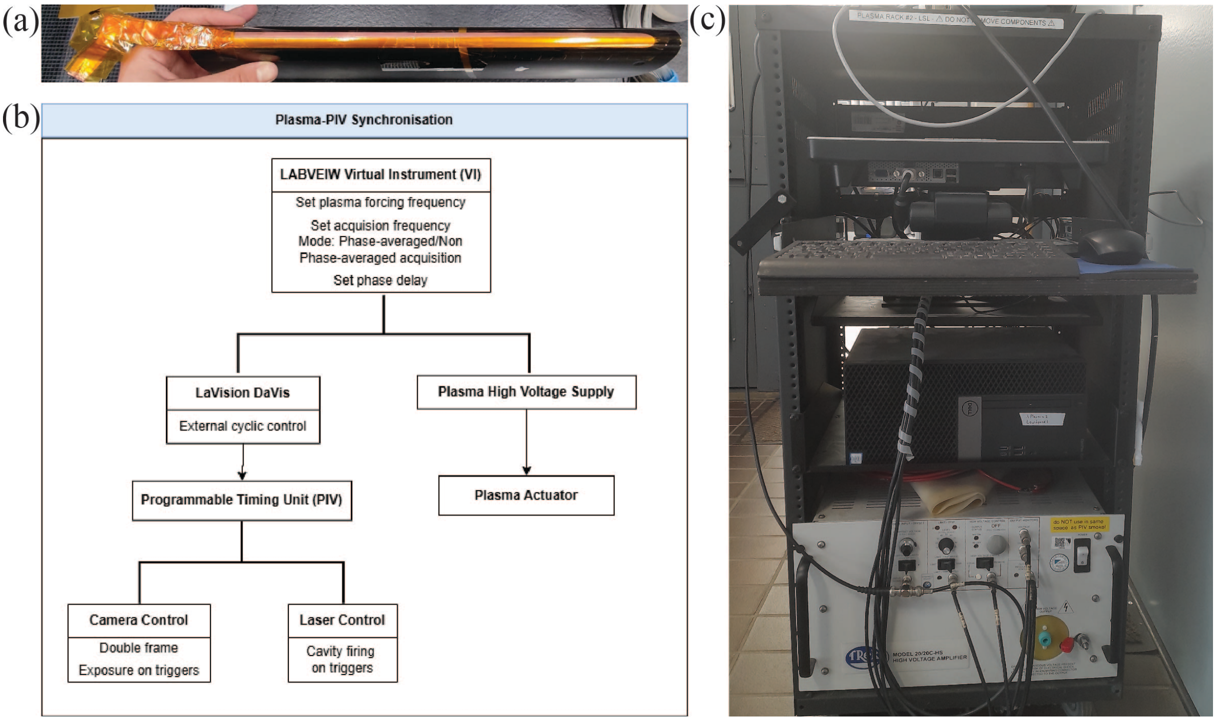

Figure 4.6: (a)The AC-DBD plasma actuator on the Leading Edge of the airfoil. (b)Flow chart of synchronization of plasma actuation and PIV. (c)The plasma control computer including the plasma amplifier and the digital-to-analog gate.

Synchronization between the laser and camera was handled digitally. Cameras and lasers were synchronized using DaVis 10, and a plasma computer using National Instruments LabVIEW software was used for laser control. An overview of the workflow is given in figure 4.6. The camera used had an exposure time of 15 μs, and pulse separation between the two consecutive frames was 100 μs in both planes. The acquisition comprised two parts: no phase-averaged sampling at a given forcing frequency and phase-averaged sampling with an applied delay between the plasma actuation and image capture. Synchronization with the measurement system was essential for phase-averaged observations of the actuated rollers at defined instants within a forcing cycle. For the phase-averaged sampling, the acquisition rates were set equal to the 15 Hz laser limit; above this, the PIV sampling was set as a multiple of 15 Hz so that structures were captured at the same phase but in different cycles. For independent sampling intended to capture average behavior without phase bias, a PIV frequency of 13.13 Hz was used to avoid accidental synchronization. For the phase-averaged mode, 350 images were taken in the wall-normal plane and 500 images were taken in the wall-parallel plane. For random acquisition, 1500 image pairs were taken for both planes in double-frame mode, with images chosen to be statistically independent; phase-averaged pairs were not independent by design, enabling statistically averaged velocity fields.

A few initial test runs helped finalise the aperture size, pulse separation duration, exposure timings, and seeding duration. This ensured that particles are discrete, maintain clear statistical significance in cross-correlation results, while also avoiding ’peak-locking’ issues that obscure sub-pixel movements.

4.2.4 Plasma Actuator Setup

In the present experiments, an AC-DBD plasma actuator was used to generate wave packets. The actuator is constructed by placing one exposed and one ground electrode on either side of the dielectric, with the airfoil serving as the negative (ground) electrode. The actuators were constructed by gluing Kapton tape to the leading edge as the dielectric barrier and gluing a copper tape on top as the high-voltage electrode. The free end of the copper tape at the leading edge was cut as a semicircle to avoid protruding edges and electric arcs, and the opposite end was connected to the power line. Initially, a carrier frequency of 2.5 kHz produced a non-uniform discharge; the carrier frequency was then increased to about 3.4 kHz and combined with a higher amplitude to achieve a uniform, properly two-dimensional, and stable plasma. Pulse length of 1 ms was used, and the actuation amplitude was deliberately kept high so that the bubble response was clearly visible and the actuated jet was uniform. As discharge can occur on both sides of the AC-DBD span and interfere, the backside of the actuator was covered with Kapton to suppress pressure-side discharge and maintain discharge only on the suction side. This is shown in figure 4.5.

4.2.5 Plasma Actuator Characterisation

The plasma actuator was characterised to quantify the momentum imparted into the boundary layer along its span. Since a three-dimensional breakdown is investigated in the aft part of the LSB, confirmation of the two-dimensionality of the plasma actuation indicated by its spanwise uniformity is deemed essential. As a direct evaluation of momentum flux was not possible, an alternate approach was adopted, and the momentum addition was estimated using the integral of the convective components of the velocity field over a Control Volume. Though an approximation, this procedure gives a consistent approach to quantify the output.

The actuator was driven by an AC carrier at a peak-to-peak voltage of 3.4 kV, and the forcing was applied with a duty cycle of 1 ms. Two wall-normal planes, located at equal distances from the mid-plane $z/c = \pm 0.26$, were selected. Raw images were captured using planar PIV, and the measurements were performed at a very low free-stream speed of 1 m/s. This condition was chosen as such a flow condition has negligible contribution from pressure and viscous forces, while in a quiescent field, the plasma-induced near-wall vortices tend to eject seeding particles and produce gaps in the field of view. In each plane, images were acquired with the actuator on and off. While the velocity fields with the actuator-on revealed a momentum jet from the exposed electrode, this was not visible in the corresponding actuator-off fields. This enabled obtaining the pure plasma-induced velocity field by subtraction.

A Control Volume(CV) was chosen near the location of the actuator on the airfoil surface. This control volume was fixed after iterating over a number of CVs, while smaller CVs barely captured the jet, larger CVs were not deemed suitable due to their size and due to viscous and pressure effects in them. The velocity field with control volume for the chosen planes is shown in figure 4.7b. It can be noted that the coordinates of both fields are offset by a small amount. This is attributed to the small misalignment of the camera lens and the chord of the airfoil, leading to the shift. The momentum was quantified by integrating the convective component along the edges of the control volume with appropriate normal vectors (Equation 4.2.1a). The x and y momentum components were computed separately, and the obtained momentum magnitude is presented in Table 4.1. The similar values indicate a uniform plasma discharge throughout the span, and hence uniform two-dimensional forcing.

$$T = \int_L \tilde{u}(\tilde{u}.\tilde{n})dL \tag{4.2.1a}$$

Table 4.1: Momentum values at different wall normal planes.

z/c	$T_x\,[m^3s^{-2}]$	$T_y\,[m^3s^{-2}]$	$\|T\|\,[m^3s^{-2}]$
-0.26	-8.863×10^{-4}	8.110×10^{-3}	8.158×10^{-3}
0.26	-6.287×10^{-4}	8.237×10^{-3}	8.260×10^{-3}

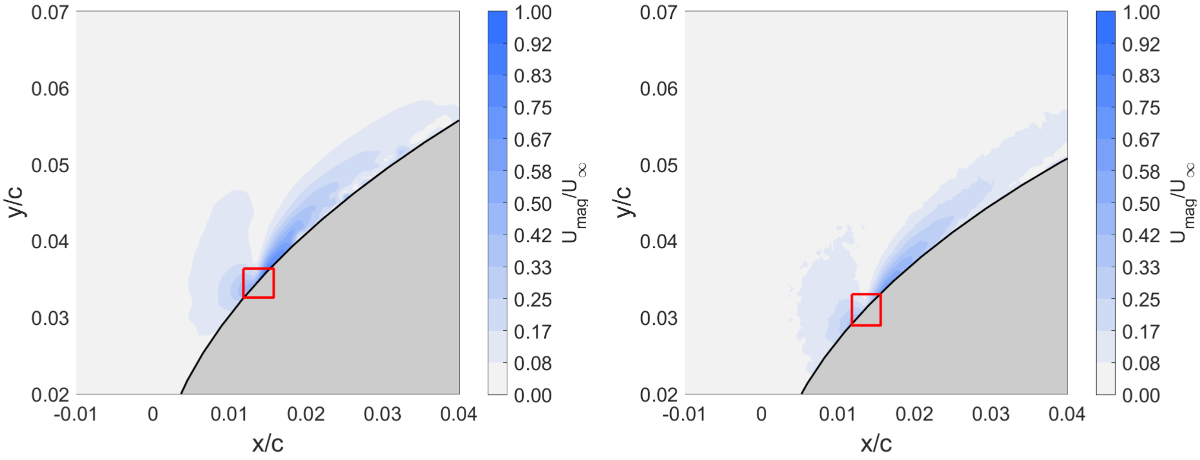

(a) Flow field at z/c = -0.26 with control volume. **(b)** Flow field at z/c = +0.26 with control volume.

5

Data processing

In this chapter, the processing and analysis steps applied to the pressure and velocity measurements are described. First, the non-dimensionalisation of the relevant variables and the experimental matrix used are presented. Subsequently, the treatment of the surface pressure signals, the pre-processing and validation of the PIV fields, and the extraction of laminar separation bubble metrics and boundary-layer integral quantities are mentioned. Finally, the methods used for analysis of velocity signals to characterise the dominant wavelengths of the coherent structures and the process used for estimation of the convective velocity are presented.

5.1 Non dimensionalisation and Notation

For convenience and scalability, quantities in this report are presented in non-dimensional form using scales from the unforced LSB. As a general practice, all lengths are normalized by the airfoil chord length c. Velocity values are normalized by the free-stream value obtained from the pitot U_∞, except for the integral boundary-layer metrics δ^*, θ, and H, which are calculated using local edge velocity (U_e) at the separation point of the boundary layer. Additionally, δ_0^* indicates the displacement thickness at separation location in the unforced case and Ω is the dimensional vorticity. Similarly, fluctuation amplitudes and standard deviations are scaled with U_∞. The characteristic Reynolds number is based on the chord length and free-stream velocity $\left(Re_c = \dfrac{U_\infty c}{\nu}\right)$, a non-dimensional frequency $f^+ = \dfrac{f\,c}{U_\infty}$ is used for describing forcing frequencies and a non-dimensional vorticity is defined as $\omega = \dfrac{\Omega \delta_0^*}{U_\infty}$.

For phase-locked cases, the non-dimensional phase notation (ϕ) describes the phase in use. Throughout the report, ϕ_i and $\phi = i$, notations have been used interchangeably (i corresponds to a phase). Though an actual phase value could have been used, this notation is used consistently for simplicity and ease of comparing the phases between both planes while accounting for the offset. In this report, the streamwise velocity component is indicated by u, the wall normal component by v, and the spanwise component by w. Additionally, a “bar” ($\bar{c}$) over a quantity indicates a time-averaged quantity, whereas a “dash” (c') indicates a fluctuating quantity. The chord-based Reynolds number used in this study is $Re_c \approx 80,000$.

Important dimensional values are mentioned here for reference. $U_\infty = 5.3$ m/s, $U_e = 7.2$ m/s, $c = 0.2$ m.

5.2 Experimental Matrix

An experimental matrix is formulated prior to the experiments to facilitate the acquisition of data. The formulation was done by keeping the research questions in purview to ensure the resulting datasets would enable the intended analysis. From the low to higher forcing frequencies up to the natural shedding (fundamental) frequency were considered. This would help see the effect of Mean Flow Deformation (MFD) on the LSB topology by comparing with the subharmonic and fundamental forcing frequencies. The breakdown of shed vortices in the aft part of the LSB would also be analysed and discussed.

Since both LSB topology and the breakdown of the actuated wave packet were to be visualized using PIV, two perpendicular measurement planes were employed. A wall-normal plane with the imaging normal to the airfoil chord to capture the LSB topology, and a wall-parallel plane with imaging parallel to the airfoil surface to capture the breakdown of actuated wave packets. Two acquisition modes were chosen: a time-averaged mode, where the camera acquisition and the plasma actuation frequency were unrelated. This showed time-averaged characteristics of the bubble in both the wall-parallel and wall-normal planes. Next, a phase-averaged mode, where both the camera acquisition and plasma actuation frequencies were set as integer multiples of each other. This enabled phase-locked acquisition of convective wave-packet and visualization of the sequence leading to breakdown. For the phase-averaged mode, both the wall-normal and wall-parallel datasets comprised five phases. The phases were separated by $\Delta t = 5$ ms. The forcing frequency was kept below the fundamental frequency ($f^+ = 10.19$), which was known from a prior time-resolved measurement. A sweep from the unforced condition to the fundamental value, with intermediate frequencies, was done to see the onset of selective amplification, modulation, and eventual broadband amplification. In the wall normal and wall parallel planes four phases overlapped with each other, as shown in table 5.1.

Table 5.1: Experimental matrix

Plane	Forcing frequency (f+)	Phases (ϕ)
Wall normal	0.03, 0.19, 0.30, 0.37, 0.45, 0.56, 0.75, 1.13, 2.26, , 4.52, 5.66, 6.79, 7.92, 9.05, 10.19, 11.32, 12.45	1, 2, 3, 4, 5
Wall parallel	0.03, 0.19, 0.30, 0.37, 0.45, 0.56, 0.75, 1.13, 2.26, 3.40, 4.52, 5.66, 6.79, 7.92, 9.05, 10.19, 11.32, 12.45	2, 3, 4, 5, 6

5.3 Processing of Pressure Data

The pressure was measured using the pressure taps on the surface of the airfoil, and the data was subsequently processed to obtain the characteristic features of the LSB. The surface pressure taps were connected to a transducer via a tube. A pressure scanner with an update rate of approximately 2 kHz was used for acquisition, and a Pitot was used to obtain the free-stream velocity.

Before capturing the pressure data, the transducers were calibrated under no-flow conditions and a procedure was followed for obtaining the pressure measurements. Data was recorded before and after experimental runs to establish the baseline and check for any drift. The acquisition time was set to 20 seconds, and the data was then time-averaged to get the time-average characteristics. The standard deviation values at each pressure tap also indicate the bubble behavior in the streamwise direction.

5.4 Processing of PIV Data

After capturing the raw images of the flow field in both planes, a number of image preprocessing techniques were applied. In the wall-normal plane, the field of view was masked to cover the reflections from the airfoil outline, and a minimum was subtracted over time, along with normalizing the local average. The PIV algorithm was then employed to obtain the vector fields. To accommodate larger particle movements, an iterative approach is generally employed, which begins with a relatively large window size and is gradually reduced to a smaller size, allowing for larger displacements to be accurately measured. A multi-pass cross-correlation was employed, starting with 48×48 px and refining to 16×16 px with 50% overlap. Spurious vectors were removed using a universal outlier detection algorithm and a median filter. The resulting vector pitch was approximately 0.43 mm in both wall-normal and wall-parallel planes.

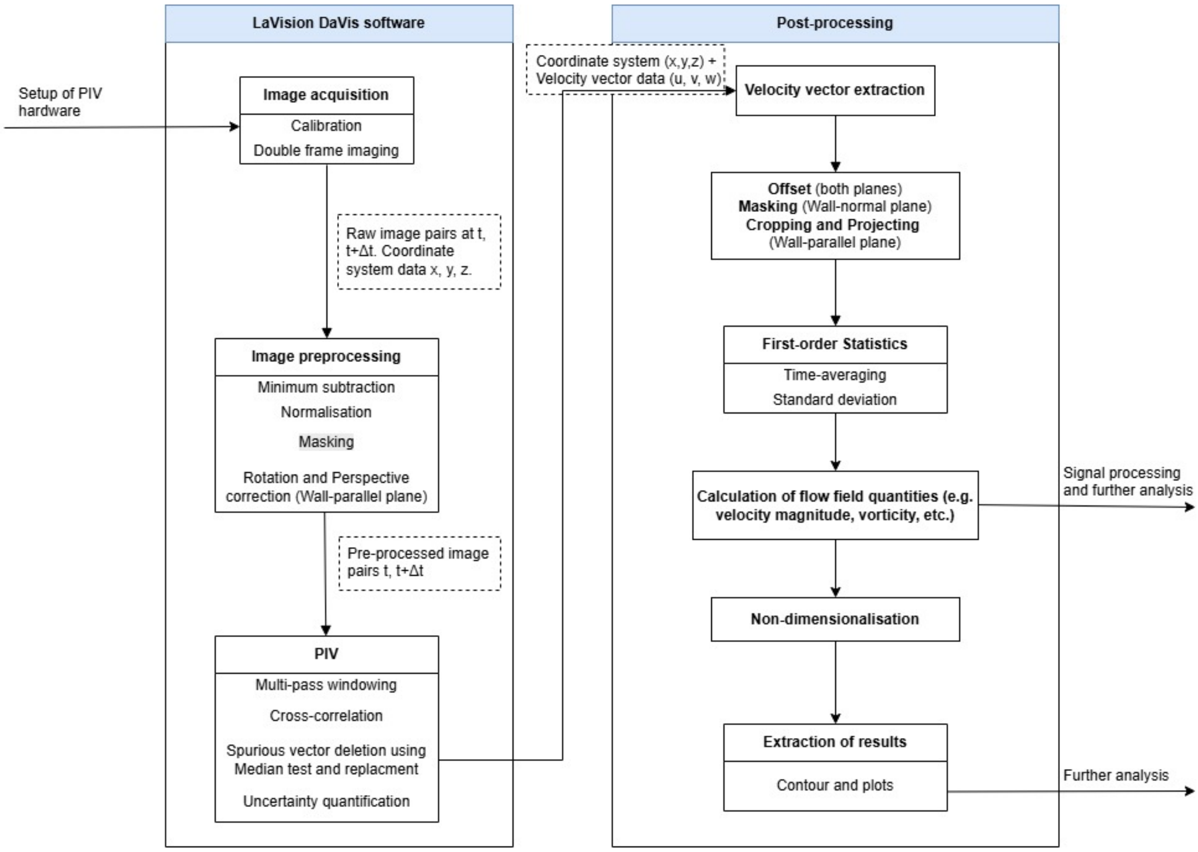

Figure 5.1: Flow chart of post-processing procedure of PIV data.

After obtaining the vector fields, further post-processing was done in MATLAB. Since the spurious vectors were removed in DaVis 10, the vectors were re-inserted in MATLAB using an in-house code to obtain instantaneous fields. As the preprocessing masking was done in DaVis for the wall normal plane, it eliminates vectors near the airfoil surface. These vectors are reinserted in the field by extrapolation using a hyperbolic tangent of the boundary layer profile from the missing point up to the airfoil profile. This gives a better resolution near the airfoil and an accurate calculation of integral boundary layer parameters and other characteristic features of the bubble in the wall normal plane. The velocity fields were then offset using the calibration data, so that they would match the airfoil outline and chord attached coordinate system as shown in figure 4.5(a).

As the coordinate system is the chord-attached and the wall-parallel plane poses an angle to the chord, the wall-parallel vector field is projected onto the chord-attached coordinate system. To obtain the appropriate angle between the wall-parallel plane and the airfoil chord, a systematic procedure is followed. The 'u'-velocity data is extracted along the wall-parallel plane location in the wall-normal plane. Similarly, the u-velocity data for the wall-parallel plane is extracted at the chord centerline(z = 0) location since both of these planes overlap here. The obtained signals were shifted and compared, which showed a very good overlap quantified by a cross-correlation peak. The peak occurs in the middle of the laser sheet, as it follows a Gaussian distribution in intensity along its width. Hence, the angle between the wall-parallel plane and the chord of the airfoil is determined to be 7.24 degrees. Using this value, the wall-parallel vector field is projected into a chord-attached coordinate system. As the projection angle is small, the resulting change in the abscissa value is minimal. Additionally, an area with elevated noise was observed in the top right corner of the wall parallel plane. This area was discarded, and the vector field was cropped to obtain symmetric vector field for further analysis.

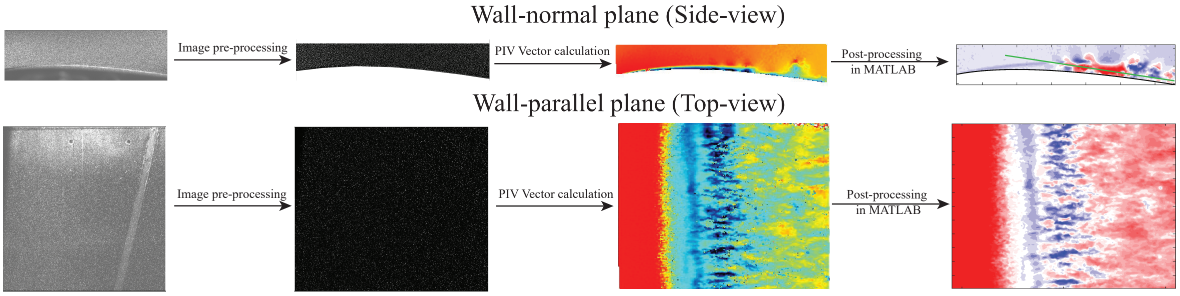

Figure 5.2: Visual flowchart of PIV processing at each step. Stage 1: Raw PIV image. Stage 2: PIV image after pre-processing(masking, perspective correction etc). Stage 3: Obtained velocity field after appropriate cross-correlation and processing. Stage 4: Obtained velocity field after offset, projection etc.

The final field of view chosen for the wall-normal plane spans from 40-150 mm (0.2-0.75c) and 0-30 mm (0-0.15c) in the dimensional x and y coordinate system, respectively. In the wall parallel plane, it spans from 45-155 mm (0.22-0.77c) and -60-60 mm (-0.30-0.30c) in the x-coordinate and in the z-coordinate, respectively. Figure 5.2 illustrates a brief overview of the processing pipeline (raw images to velocity fields). A comprehensive flowchart of the workflow is shown in figure 5.1.

5.5 Processing of velocity signals

5.5.1 Fourier Analysis

As noted in Section 3.1, the wavelength of coherent structures in the wall-parallel plane can be used to infer the 3D breakdown and flow development after the bubble. Hence, velocity signals in regions of interest need to be processed for wavelength extraction. Due to the wide range of applicability and prevalent use, spatial Fourier analysis was applied to the wall-parallel velocity field to decompose the spatial signal into its constituent wavenumbers. The wave numbers provide a direct link between physical flow structures and their spanwise or streamwise signatures.

Spatial Fast Fourier Transform was performed on velocity signals in both spanwise and streamwise directions. While existing periodic flow structures in phase-averaged velocity fields showed a prominent peak, instantaneous fields required signal preprocessing (mean removal and tapering) to reveal dominant peaks. Though DC content often dominated the average in the presence of slope or non-periodicity, pre-processing using a Hann window did not improve the results significantly. Despite the treatment, spectral leakage, the inability to detect dominant peaks, and insufficient resolution, highlighted limitations of the spatial FFT. Additionally, limited signal length and few repetitions restricted accuracy, so longer wavelengths could not be resolved within a short signal length.

5.5.2 Wavelet Analysis

Since the Fourier analysis did not give any useful results, the short-time Fourier transform(STFT) was considered. However, its fixed window imposes a constant time-frequency resolution that poorly matched with scales relevant in the flow. In contrast, the wavelet transform provides a multi-resolution localization enabling better characterization of flow structures. The approach was applied to spatial signals extracted from the wall-parallel plane in the streamwise and spanwise directions. A continuous wavelet transform with a Morlet mother wavelet is chosen as it gives a balanced space-wave number localization. Signals were pre-processed in the same manner before applying the wavelet transform. The transform produced scalograms, which conveyed the presence and dominance of different scales at different locations. For consistency, scale normalization was kept constant across cases. It showed the presence of multiple scales in a signal, which was useful in evaluating the nature of the breakdown in the wall-parallel plane. Sample process workflow is presented in figure 5.3 and it shows how an extracted signal manifests in a scalogram (convolution coefficient map), with the marked peak indicating the dominant wavelength of the signal.

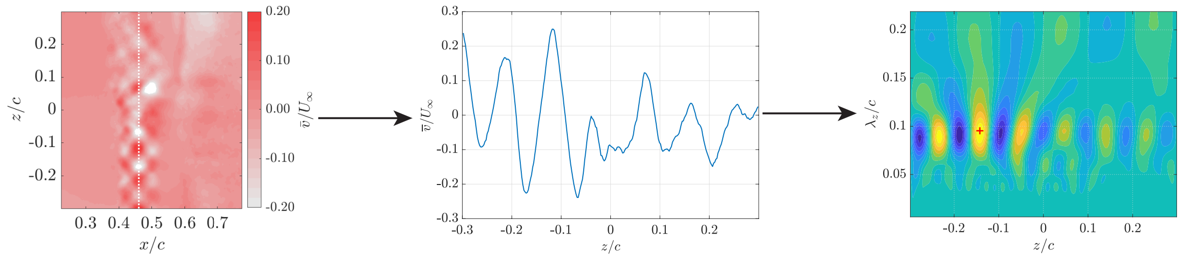

Figure 5.3: Visual flow chart showing a brief overview of the post-processing velocity signal to wavelet coefficients. This figure acts as an aid to the explanation presented in the text. Stage 1:The velocity signal is extracted from the marked location on the wall parallel velocity field. Stage 2: The extracted velocity signal is then processed using wavelet analysis. Stage 3: A convolution coefficient map is obtained from the wavelet analysis. The map highlights multiple peaks indicative of constituent wavelengths of the signal.

The wavelengths have to be analyzed over a certain spanwise length, for the streamwise wavelengths, and in the spanwise direction, for the streamwise wavelengths. This is done to account for the periodicity in both directions. The probing window is of finite length, and the velocity signals have been extracted from the area within those bounds. The wavelet analysis is run on those signals, and several scalograms are obtained. From those scalograms, dominant peaks are obtained which show wavelengths in those signals and their powers. While a probability density function would give the first statistical moment and its central tendencies, it would not account for the power of the wavelengths. Hence, a joint probability density function is constructed that shows wavelength, corresponding power, and average power over the selected dominant peaks from the scalograms. The peak having maximum average power value is then chosen as the dominant wavelength for that particular probing window. A sample process map is shown through the flow chart in figure 5.4. In addition to the visual flow charts, a comprehensive flowchart of the workflow is shown in figure 5.5 as well.

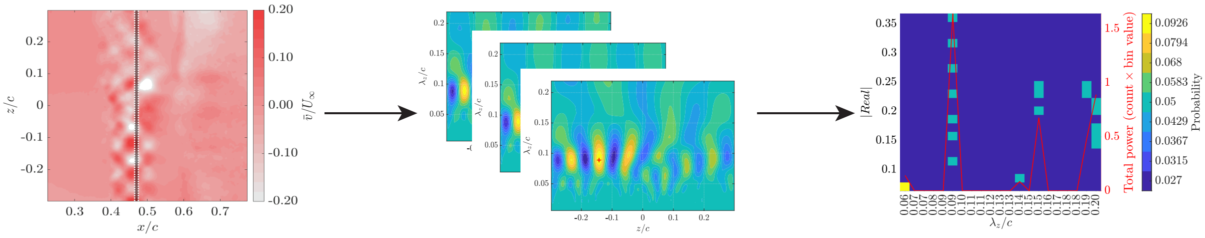

Figure 5.4: Flow chart of post-processing comprehensively showing extraction of dominant wavelengths to form a joint probability density function for a probing window. Stage 1:The velocity signals are extracted from the chosen window on the wall parallel velocity field.
Stage 2: The extracted velocity signals are then processed using wavelet analysis to obtain a convolution coefficient map. Values of multiple prominent peaks and their values are extracted from a map to account for the constitutive wavelengths of the signal.
Stage 3: The obtained peaks and their powers are then constructed as a joint probability density function. The cumulative power corresponding to prominent wavelengths is calculated and the wavelength having dominant power is chosen.

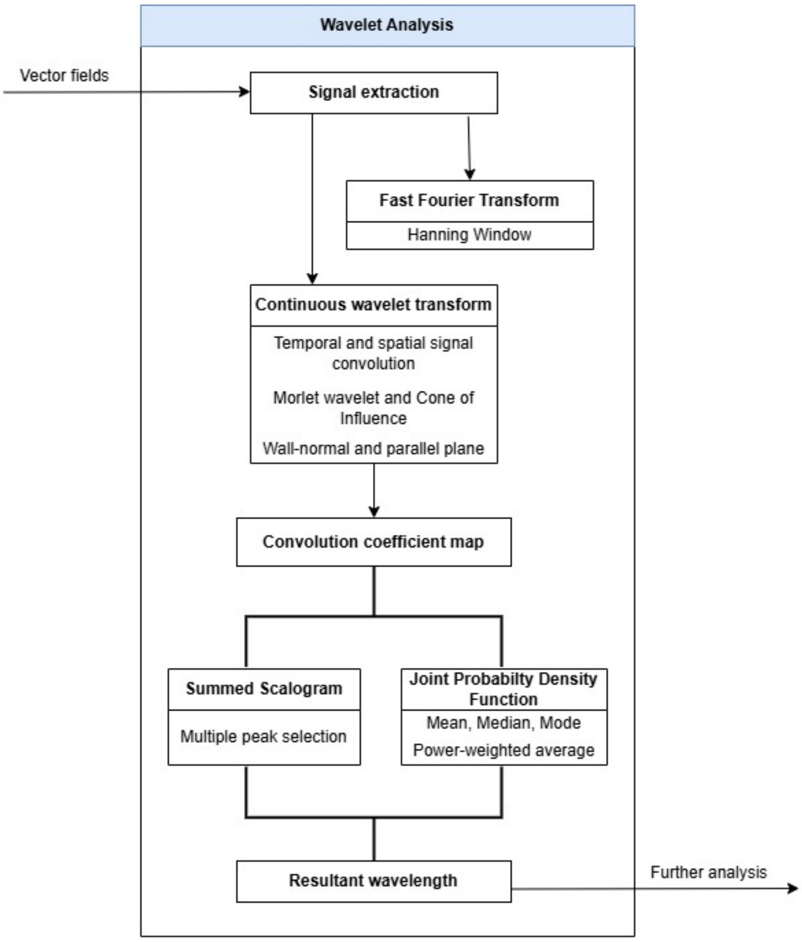

Figure 5.5: Flow chart of signal analysis from velocity data.

5.5.3 Convective Velocity

.

While the processing steps and the wavelength-extraction method have been established, the location of extracting spanwise velocity signals from the wall-parallel plane along the chord is ambiguous due to the variation of vortex breakdown location with forcing frequency. Hence, a location per phase is set by estimating the location of the actuated wavepacket at that phase. This is done using convective velocity (Michelis et al., 2017). To determine the convective velocity, wall-normal velocity fields at a lower forcing frequency are used. For each phase, the velocity field is integrated from top to bottom to produce a one-dimensional chordwise signal. These signals are then stacked as shown in figure 5.6a and the wave packet peak is identified by the peak amplitude of the signal. A linear fit of peak position versus phase yields the convective velocity. For the current study, $U_c = 0.81U_\infty$ which agrees with previous studies (Lambert and Yarusevych, 2017). With this convective velocity, the packet position can be tracked, providing a reliable metric for velocity signal extraction location.

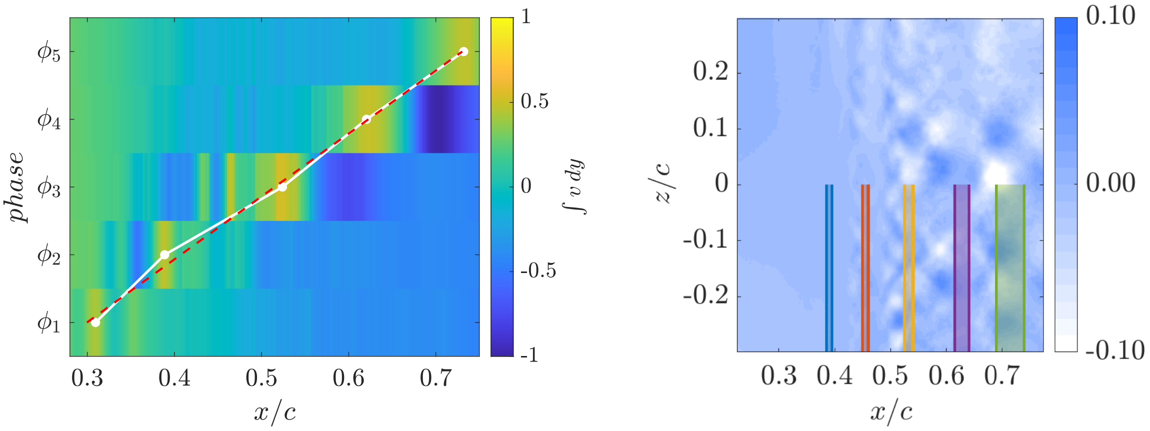

(a) Phase–streamwise location map of the y–integral of wall-normal velocity. White dots indicate the normalised signal peak.

(b) Chordwise variation of the probing windows, arranged in increasing phase ($\phi = 2, 3, 4, 5, 6$), where higher phases correspond to windows located farther downstream.

Figure 5.6: Convective ridge map and the corresponding probing windows with phase.

Windows are placed in the wall-parallel plane, and signals from these windows are used for wavelength extraction for a particular phase via spatial wavelet analysis. As discussed in section 4.2.2, the perturbation growth levels on one side are higher. After analyzing the flow fields of several frequencies, $-0.3 \leq z/c \leq 0$ is chosen to extract signals. The probing window locations are shown in figure 5.6b. Additionally, in the wall-parallel plane, distinct streamwise flow regimes are observed: Upstream part (approximately $x/c \approx$ 0.35-0.5), where the shed vortices have not yet advected out of the plane, have better extracted signals, and the dominant wavelengths are shorter, consistent with rapid breakdown. Downstream part, where parts of the structures move out of the wall-parallel plane, the signal is then biased toward larger streamwise wavelengths, making the wavelength detection more challenging. For this reason, the signal extraction window length is increased in the downstream part to capture the breakdown characteristics.

6

Results and Analysis

This chapter discusses the results obtained from the data of the experimental campaign. Section 6.1 discusses the pressure characteristics, followed by the flow-field characteristics in section 6.2. Followed by these sections analysis on bubble topology and breakdown characteristics is presented in section 6.3 and section 6.4 respectively.

6.1 Pressure data

The time-averaged surface pressure distributions were used to calculate the pressure coefficient (C_p) using the equation 2.3.1. C_p was plotted with the airfoil chord (x/c) to establish the LSB behavior. The plot in figure 6.1 shows a plateau followed by a rapid recovery. This indicates separation followed by reattachment, respectively, in line with prior studies (Alam and Sandham, 2000; Michelis et al., 2017; Borgmann et al., 2022). Separation and reattachment points of the unforced baseline LSB, obtained from velocity fields, are overlaid for reference. Along with the pressure characteristics of the unforced bubble, the pressure distribution of forced LSBs are also plotted for comparison. As the forcing frequency increases, the extent of the pressure plateau decreases, indicating a deformation of the mean flow and an overall smaller LSB. This observation aligns with the pressure variation plot of Borgmann et al. (2022), fig.15(a). An important observation to note is that at some lower forcing frequencies $f^+ = 0.04$, the pressure distribution resembles to that of the unforced case. This is because of the larger time gap between subsequent disturbances, such that no mean flow deformation happens. The pressure plateau observed for such cases is closer to that observed for the unforced bubble. However, as the forcing frequency increases, the mean flow deforms more, resulting in a smaller bubble and hence a smaller pressure plateau.

Since the measurements were time-averaged, the standard deviation of the coefficient at each tap provides the variance. The separation and plateau region showcase lower standard deviation values, while the pressure recovery reattachment region shows a higher value. The increased values near reattachment indicate a dominant contribution from vortex shedding. This behavior is consistent with previous studies (Diwan and Ramesh, 2009; Michelis et al., 2017) that show elevated fluctuation levels in the shedding region. Additionally, the standard deviation value also reduces with increasing forcing frequency, indicating an increasing coherent shedding and breakdown.

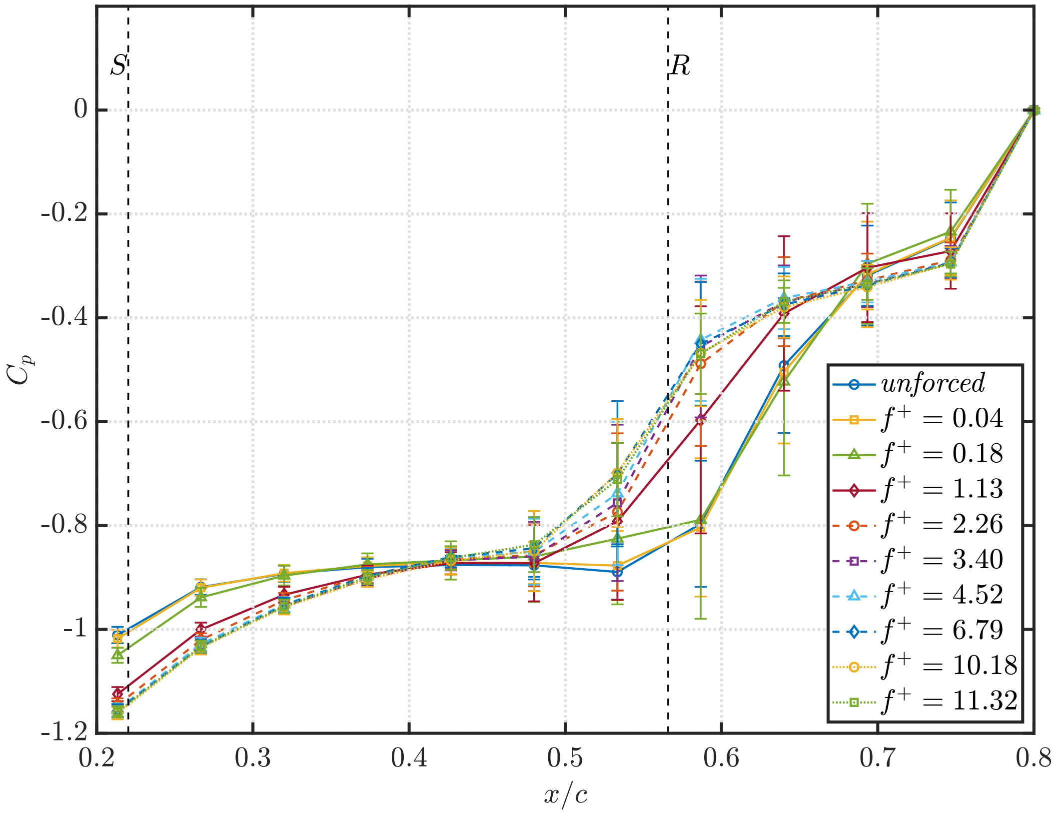

Figure 6.1: C_p distribution in streamwise direction. Dashed lines show the Separation (S) and Reattachment (R) points of the unforced bubble. These points are obtained from the streamwise velocity field of the unforced bubble and presented here for reference.

6.2 Flow-field characteristics

This section discusses the flow field characteristics of the unforced and forced laminar separation bubble (LSB) across the forcing frequencies. The unforced case is established as a reference in terms of topology in the wall-normal plane. Forced cases are then presented to show the effect of forcing (actuation) on the time-averaged bubble and disturbance wave-packet evolution. Three metrics are used for discussion: (i) mean topology in the wall-normal plane; (ii) spatial standard deviation maps; and (iii) phase-averaged velocity and vorticity sequences in both planes to visualize the wave packet roll-up, deformation, and breakdown. These observations provide a qualitative comparison and are used to discuss the changes in bubble topology and wavelength-based breakdown metrics in later sections.

In the context of an LSB, the shedding frequency is termed as natural or fundamental frequency. A fraction of this fundamental frequency are termed as subharmonic frequency, whereas integer multiples of this frequency are called superharmonic frequency. The terminology is used in further sections.

6.2.1 Unforced bubble

To establish a baseline, the unforced laminar separation bubble characteristics are presented and discussed. Both the wall-normal and wall-parallel velocity fields and results derived from them are used. The time-averaged bubble in the wall-normal plane is presented in figure 6.2a. The figure shows a short separation bubble enclosed by a dividing streamline, and its bounds are shown by the separation point (S), the reattachment point (R), and the maximum bubble height (T). The streamline is obtained by computing the streamfunction over the time-averaged velocity field. Within the bounding streamline, a recirculation region is observed, which can also be inferred in the pressure measurements (figure 6.1) by a pressure plateau at the same streamwise extent. Additionally, the reverse-flow magnitude in the recirculation region is within the threshold for the primary instability to be convective in nature.

Development of boundary layer profiles in the streamwise direction is shown in figure 6.2b, with the profiles in the fore portion of LSB showing an inflection point. This figure is overlaid with the time-averaged displacement thickness, which coincides with the inflection point and agrees well with the observations of Boutilier and Yarusevych (2012). They further state that the presence of an inflection point in the velocity profiles at the time-averaged displacement thickness profile indicates that the KH instability is the dominant amplification mechanism.

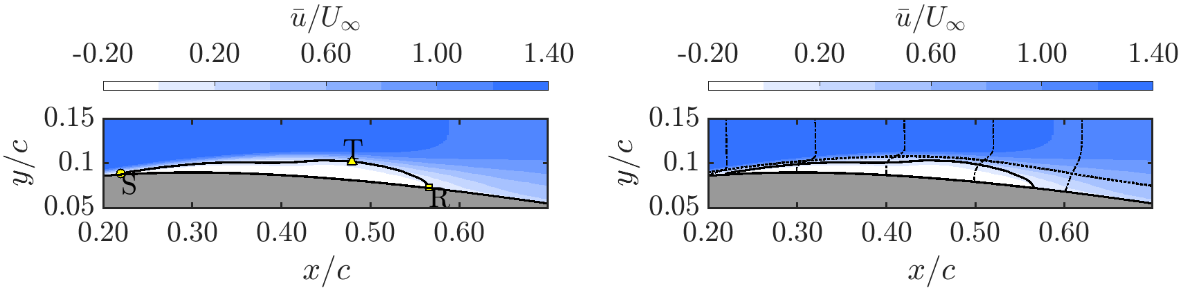

(a) Time-averaged streamwise velocity field in the wall-normal plane. Solid line: dividing streamline.

(b) Variation of boundary layer profile and time-averaged displacement thickness.

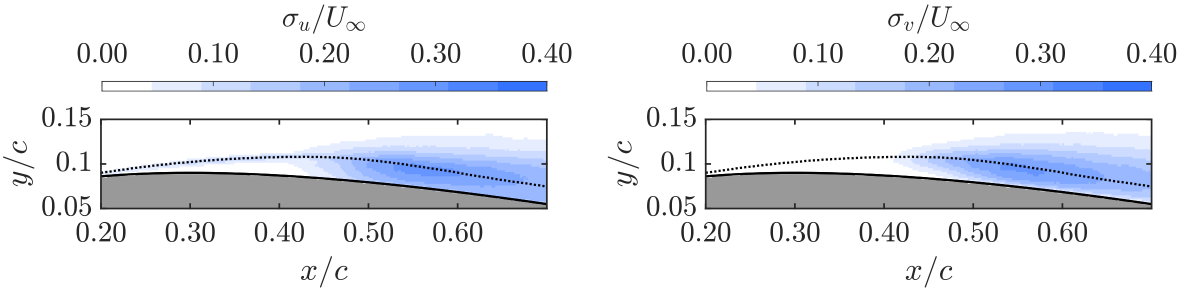

(c) u standard deviation map indicating the streamwise velocity fluctuations.

(d) v standard deviation map indicating the wall normal velocity fluctuations.

Figure 6.2: Wall-normal topology of the unforced LSB. S: Time-averaged separation point, T: Time-averaged maximum bubble height, R: Time-averaged reattachment point.

To characterise spatial fluctuations, the standard deviation of both u and v velocity fields is presented in figure 6.2c and 6.2d. The u standard deviation field shows elevated values near the separation, indicating variability in the separation point due to incoming natural disturbances. Moreover, the standard deviation in the fore portion of the bubble aligned with the displacement thickness denotes shear-layer flapping (Michelis et al., 2017). Both u, v standard deviation fields indicate the breakdown of vortices shed downstream of the bubble.

Vortex dynamics for the unforced bubble is shown using instantaneous vorticity field contours presented in figure 6.3. The location of saturation varies in time (from cycle to cycle). After shedding, the rotating vortices bring high-speed fluid from the outer flow towards the wall, which is then diverted upstream and downstream along the wall, causing flow reattachment. As the vortices convect, they undergo a diffusive growth before breaking down into smaller structures. The breakdown begins with deformation in the span of the shed vortex due to the relative motion of fluid elements. While this is a general observation, variation in incoming natural disturbances can cause the cores of the growing vortices to co-rotate and eventually merge to form a larger structure aperiodically. A merged vortex is observed at $x/c = 0.5$ in figure 6.3b. Several studies (Lambert and Yarusevych, 2017, 2019; Kurelek et al., 2019) note this phenomenon in the aft part of the LSB formed on an airfoil and flat plate, and along with variation in convective velocity, they attribute it to saturation of the subharmonic mode.

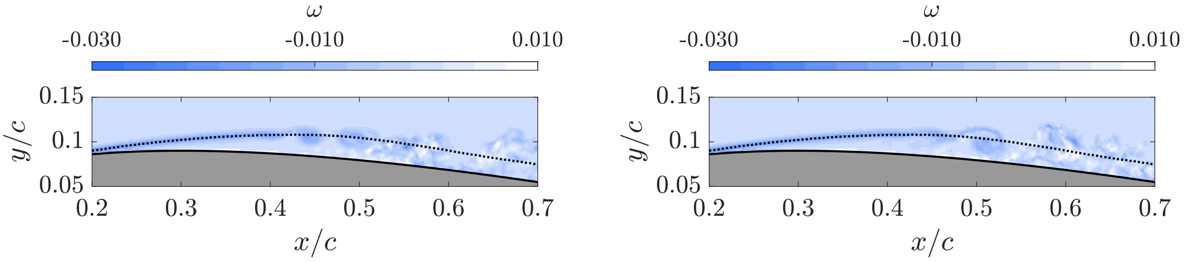

(a) Instant 1.

(b) Instant 2.

Figure 6.3: Vortex rollup and shedding of the unforced bubble. The chosen instances are by choice for representation only and are not consecutive. Instant 1 occurs before Instant 2, and they are not correlated. Instant 2 shows vortex merging. The dotted line indicates time-averaged displacement thickness.

Using the velocity fields of the wall-parallel (x–z) plane, the spanwise uniformity of the time-averaged flow is discussed. In figure 6.4, mean-velocity contours are shown for u (streamwise) and w (spanwise) components. The location of transition and reattachment, obtained from the wall-normal plane, is marked for reference. Since the plane is located at some distance from the surface, as seen in figure 4.5, the reattachment location is not visible in the u velocity field. However, no spanwise undulation is observed in the velocity field, indicating the absence of absolute instability. In the w field, an elevated velocity value indicated by an arrow is observed in the top left part of the field at $x/c = 0.4$, which is attributed to a different perturbation growth, as previously discussed in section 4.2.2. A protruding edge on one side of the airfoil contributed to higher disturbance growth on one side.

As the shed structures convect downstream distinct spanwise undulations develop. This is identifiable by a dark blue patch at $x/c \approx 0.43, 0.48$ and 0.53 in figure 6.4c. One of these rollers is indicated by an arrow. The undulations intensify, followed by a rapid three-dimensional breakdown into smaller-scale structures, giving way to a turbulent boundary layer. From previous studies (Michelis et al., 2018; Kurelek et al., 2019; Borgmann et al., 2022), it can be said that the superposition of fundamental and oblique modes causes this spanwise undulations. Distinct peak-and-valley deformations are observed during the process in figure 6.4c. The valley segments lag while peak segments of the filament surge in the streamwise direction. Such a deformation causes in-and out-of-plane motion, which further intensifies vortex stretching and leads to the breakup of shear-layer vortices. While this explanation is based on the vortex filament model by Kurelek (2021), it explains only the initial undulation of the vortex tube. From a stability perspective, the periodic base flow (the shed vortex) is susceptible to formation of many spanwise wavelengths, which drive the undulation (Borgmann et al., 2022).

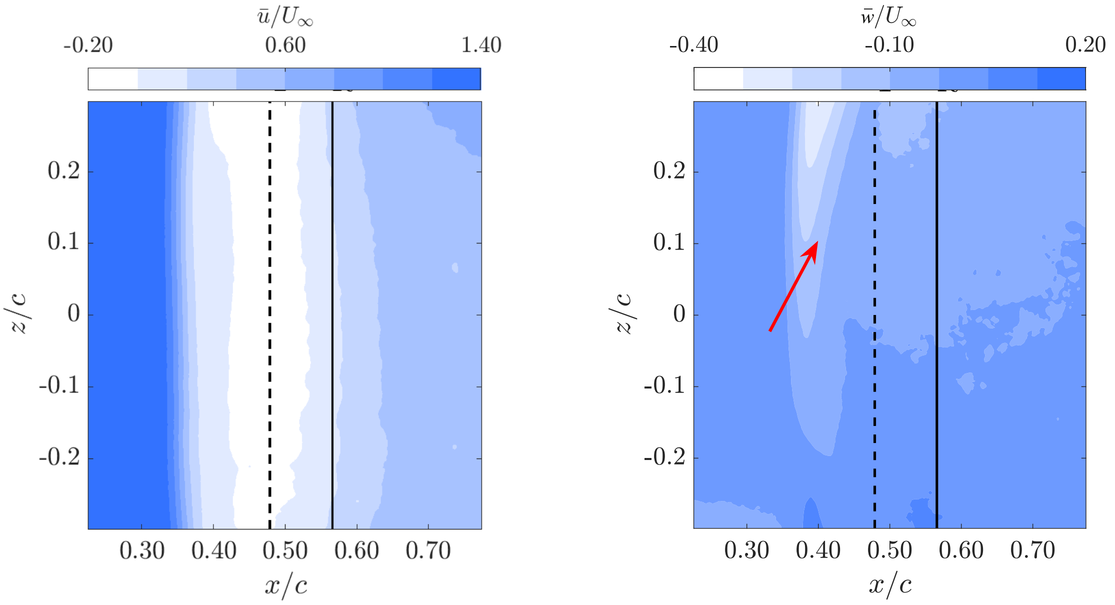

(a) Time-averaged streamwise velocity field. **(b)** Time-averaged spanwise velocity field.

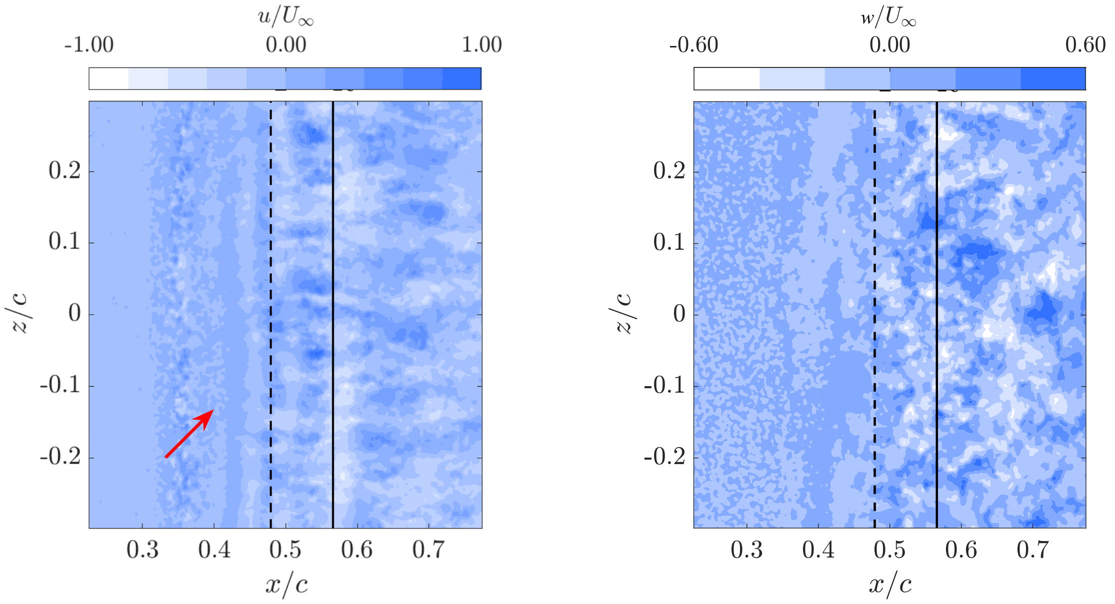

(c) Instantaneous streamwise velocity field showing shed structures and their breakdown. **(d)** Instantaneous spanwise velocity field showing breakdown of shed structures.

Figure 6.4: Wall-parallel velocity profile of the unforced LSB. The dotted line refers to the time-averaged maximum bubble height, and the solid line refers to the time-averaged reattachment point. The overlaid values are taken from the wall-normal plane.

6.2.2 Forced bubble

With the baseline LSB established, the effect of forcing is discussed here using the flow-field characteristics. For comparison, one representative case is selected from each forcing frequency range: (i) a low forcing frequency at $f^+ = 0.19$, (ii) an intermediate frequency at $f^+ = 2.26$, (iii) a near-subharmonic of the fundamental at $f^+ = 4.52$, and (iv) the fundamental (natural/shedding) frequency at $f^+ = 10.19$. These cases are used to discuss aspects of the flow field under a common framework. A quantitative reason for classifying the forcing frequency range is provided in the breakdown characteristics section 6.4. The wall normal time-averaged velocity fields, standard deviation fields, and the phase-averaged vorticity field sequence of both the wall-normal and wall-parallel planes are discussed.

6.2.2.1. Time-averaged bubble behavior

Upon introduction of forcing, the bubble exhibits a reduction in size as compared to the unforced bubble presented in figure 6.2a. For comparison, the streamlines from different forcing frequencies ($f^+ = 0, 4.52$), overlaid on the streamwise velocity field of forcing frequency $f^+ = 2.26$ are shown in figure 6.5. The difference in streamline outline indicates the Mean Flow Deformation (MFD).

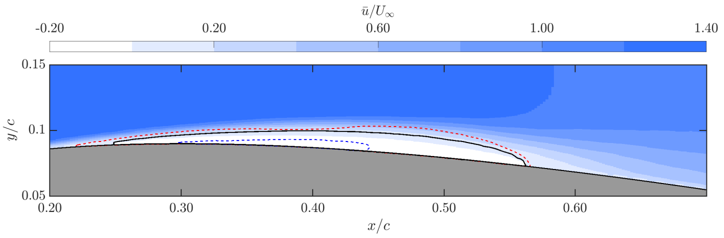

Figure 6.5: Time averaged streamwise velocity field of $f^+ = 2.26$ in the wall-normal plane. Bounding streamlines of different forcing frequencies are plotted for comparison. The black line indicates the bounding streamline of $f^+ = 2.26$, the red dashed line indicates the bounding streamline of $f^+ = 0$, and the blue dashed line indicates the bounding streamline of $f^+ = 4.52$.

The time-averaged streamwise velocity fields for all the forcing frequencies are also presented in figure 6.6. As it is observed, the reduction in size increases as the forcing frequency increases. This observation is in accordance with previous studies where Marxen and Rist (2010) see Mean Flow Deformation (MFD) at higher forcing frequencies. A lower MFD is observed for lower forcing frequency, while a higher MFD is visible for intermediate and higher forcing frequencies. A key observation is the similar bubble size for $f^+ = 4.52$ and $f^+ = 10.19$ despite a large difference in forcing frequency. Kurelek et al. (2019) note a similar observation in their study, which they attribute to equal momentum transfer from the freestream. In addition to the reduction in bubble size, there is a change in separation point, reattachment point, and maximum bubble height as well. The separation point moves downstream, whereas the reattachment point moves upstream, and the maximum bubble height moves closer to the airfoil. The observed streamwise extent of the bubbles presented in figure 6.6 also agrees well with the pressure variation observed in figure 6.1. With increasing forcing frequency, the plotted time-averaged displacement thickness moves closer to the wall. The changed displacement thickness profile indicates enhanced stability with respect to the incoming disturbances (Boutilier and Yarusevych, 2012).

Time-averaged wall-parallel velocity fields do not show any major flow characteristics for lower ($f^+ = 0.19$), intermediate ($f^+ = 2.26$), and near-subharmonic ($f^+ = 4.52$) forcing frequencies. However, at the fundamental ($f^+ = 10.19$) forcing frequency, a marked difference emerges in the velocity field observed in the wall-parallel plane: in the w velocity field, periodic structures are visible. This is shown in figure 6.7b along with the flow-field of lower forcing frequency for comparison. Similar periodicity is also observed in the wall-parallel time-averaged spanwise velocity field at other forcing frequencies near the fundamental forcing frequency, where lock-in occurs.

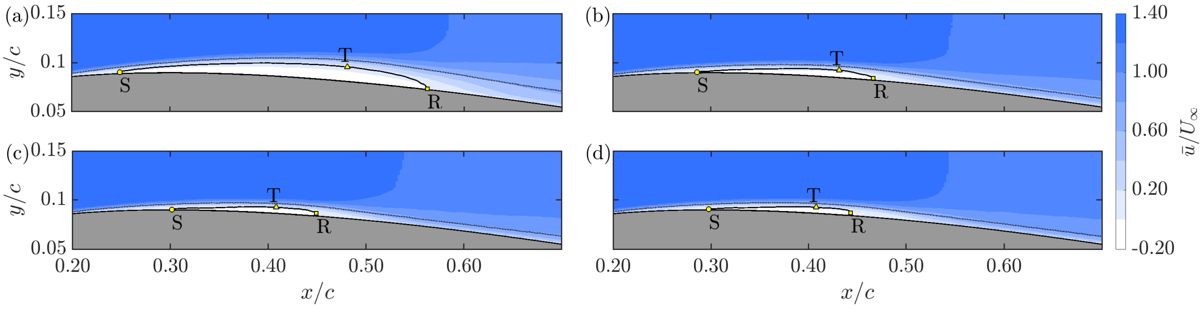

Figure 6.6: Time averaged streamwise velocity field of the forced cases in the wall-normal plane. (a)$f^+ = 0.19$, (b)$f^+ = 2.26$, (c)$f^+ = 4.52$, (d)$f^+ = 10.19$. The dotted line is the time-averaged displacement thickness. S: Time-averaged separation point, T: Time-averaged maximum bubble height, R: Time-averaged reattachment location.

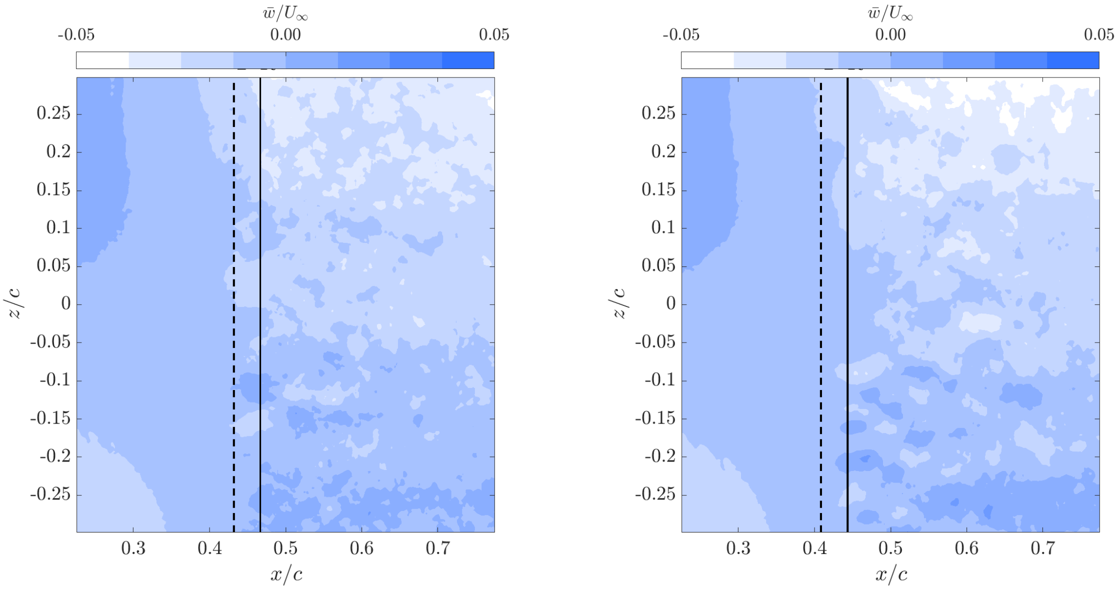

(a) Time averaged wall parallel spanwise velocity field showing w component for forcing frequency $f^+ = 2.26$.

(b) Time averaged wall parallel spanwise velocity field showing w component for forcing frequency $f^+ = 10.19$.

Figure 6.7: The dashed line indicates the time-averaged maximum bubble height, and the solid line indicates the time-averaged reattachment point. The lines indicate the locations as observed only in the wall-normal plane.

The fluctuations in the velocity field and other low-frequency behavior are studied using the standard deviation fields of the u and v velocity components. The general trend is a reduction in the standard deviation value with an increase in forcing frequency. For the low forcing frequency regime, the u standard deviation field (figure 6.8a) is substantially different from the unforced case (figure 6.2c). The increased values indicate bubble shortening during the forcing cycle and subsequent elongation during its recovery. This causes the shear layer to oscillate, leading to a higher standard deviation along the displacement thickness. Additionally, the reverse-flow region also shows increased standard deviation, indicating a dynamic bubble state between actuations. The v standard-deviation field (figure 6.8b), however, does not capture the dynamic state of the bubble but only the vortex breakdown, and has similar values to the standard deviation observed for the unforced bubble (figure 6.2d). At the intermediate forcing frequency ($f^+ = 2.26$), figure 6.8c shows the reduced standard deviation in the fore part of the bubble, indicating reduced intensity of shear-layer flapping, though some standard deviation near the separation point is still observed. This is much lower than that of the $f^+ = 0.19$ case. In addition, the lower v-component standard deviation indicates a more organised breakdown. For the near subharmonic $f^+ = 4.52$ and fundamental forcing frequency $f^+ = 10.19$, the standard deviation maps are similar to the observations made at $f^+ = 2.26$. Additionally, the decrease in standard deviation values with forcing frequency also agrees with the lower standard deviation values seen in the pressure coefficient graph (figure 6.1) in the reattachment region of the LSB.

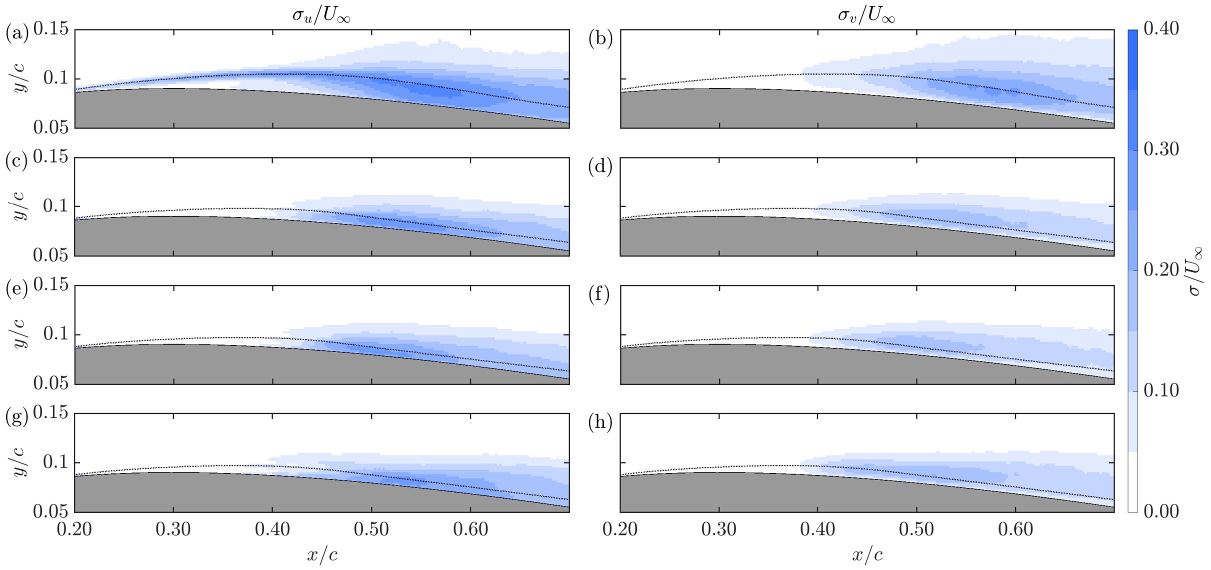

Figure 6.8: Standard deviation fields of streamwise velocity (u) and wall normal velocity (v) of the forced cases in the wall-normal plane presented in the left and right columns, respectively. (a),(b)$f^+ = 0.19$, (c),(d)$f^+ = 2.26$, (e),(f)$f^+ = 4.52$, (g),(h)$f^+ = 10.19$. The dotted line is the mean displacement thickness.

6.2.2.2. Wave packet evolution in wall-normal and wall-parallel plane

With the time-averaged characteristics of the bubble discussed in the previous section. Phase-averaged characteristics are discussed in this section for the same four cases using the Wall-normal and Wall-parallel vorticity fields.

The wall-normal and wall-parallel phase-averaged vorticity fields of $f^+ = 0.19$ are used to discuss the amplification of disturbances, vortex shedding, and breakdown. The figure 6.9 shows the evolution of the actuated wave packet as it saturates and forms vortices for one actuation cycle. It is established from previous studies (Michelis et al., 2017) that shedding occurs at a natural frequency due to selective amplification of disturbances. The actuated wave packet is tracked using the convective velocity ($U_c = 0.81U_\infty$), and the vortex V_2 is estimated to be the primary vortex resulting from actuation. The identification and location of this vortex, determined using the convective velocity, also agrees well with the observations made for other forcing frequency cases. This identification helps classify the dominant mode driving the breakdown of the vortex, and since the primary vortex V_2 has an enhanced normal mode, its breakdown characteristics would be different than other vortices. Vortices (V_1, V_3) also form part of the actuated wave packet, and evidence of prior weak shedding is visible in phase $\phi = 2$ at $x/c = 0.55$. As vortex V_2 passes the location of maximum shape factor, the following vortices break down quickly at $x/c = 0.45$ ($\phi = 3, 4$). This observation is consistent with Michelis et al. (2017), who attribute this to a change in the bubble's stability induced by vortices interacting with the mean reattachment point ($x/c = 0.46$ here). Here, the vortices also modify the bubble's topology, thereby altering the stability and growth rates of instability modes in subsequent vortices, resulting in different breakdown characteristics.

From a kinematic perspective, the shed vortices V_1 and V_2 are affected by the change in relative velocity in the aft part of the LSB (Lambert and Yarusevych, 2017; Kurelek et al., 2016), causing them to convect with different speeds, approach each other, co-rotate, and eventually merge. It can be seen that the V_1 is closer to the wall and its convective velocity is lower than that of the upstream vortex V_2. As V_1 slows down, as seen in the sequence presented in figure 6.9c, the following vortex V_2 moves away from the surface. The vortices begin to orbit as they approach each other, and they eventually merge. This observation is in line with the calculated convective velocity value presented in section 5.5.3.

While merging is observed in an unforced bubble (figure 6.3) is in line with the observation by Lambert and Yarusevych (2017), a phase-averaged vortex merging is a new observation. Irrespective of merging, the shed vortices convect as distinct structures, appearing further downstream than those shed from the unforced bubble, indicating delayed breakdown into small-scale structures. Additionally, the merging here takes place between the transition and reattachment location. This observation is in line with previous studies (Lambert and Yarusevych, 2017; Kurelek et al., 2019).

The wall-parallel vorticity fields of $f^+ = 0.19$ are presented in figure 6.10 and the observations are discussed in tandem with wall-normal vorticity fields presented in figure 6.9. The effect of the uneven growth rate of disturbances due to leading-edge misalignment is distinct here. While one half of the span shows prominent structures, the other half does not. In $\phi = 2$, the undulations in $0.35 \leq x/c \leq 0.42$ correspond to vortex V_3, due to acting secondary instability mechanisms. Given that previous studies (Marxen et al., 2013) have reported elliptic instability acting on vortex cores causing undulations, the observed behavior could therefore be attributed to an elliptic instability of the vortex cores. In $\phi = 3$, the vortex V_2 does not appear as it has moved out of the plane and is near the mean reattachment region. This is visible in the third sequence of figure 6.9. The vortex V_3 develops significant undulation, and the onset of breakdown is observed between $0.38 \leq x/c \leq 0.5$. By $\phi = 4$ (figure 6.10c), vortex V_2 has merged with the vortex V_1 (figure 6.9). Vortex V_3 has broken down and the breakdown shows a signature of hairpin structures (Alam and Sandham, 2000; Hosseinverdi and Fasel, 2018; Kurelek et al., 2016) in $0.4 \leq x/c \leq 0.5$. At phase $\phi = 5$, remnants of the vortex breakdown are visible in this plane. Vortex V_3 has broken down at $x/c \approx 0.6$, whereas the other two vortices, V_1 and V_2, have merged and their cores are completely out of the wall-parallel plane now, though some structures which could be the outer layer are visible at $x/c \approx 0.7$.

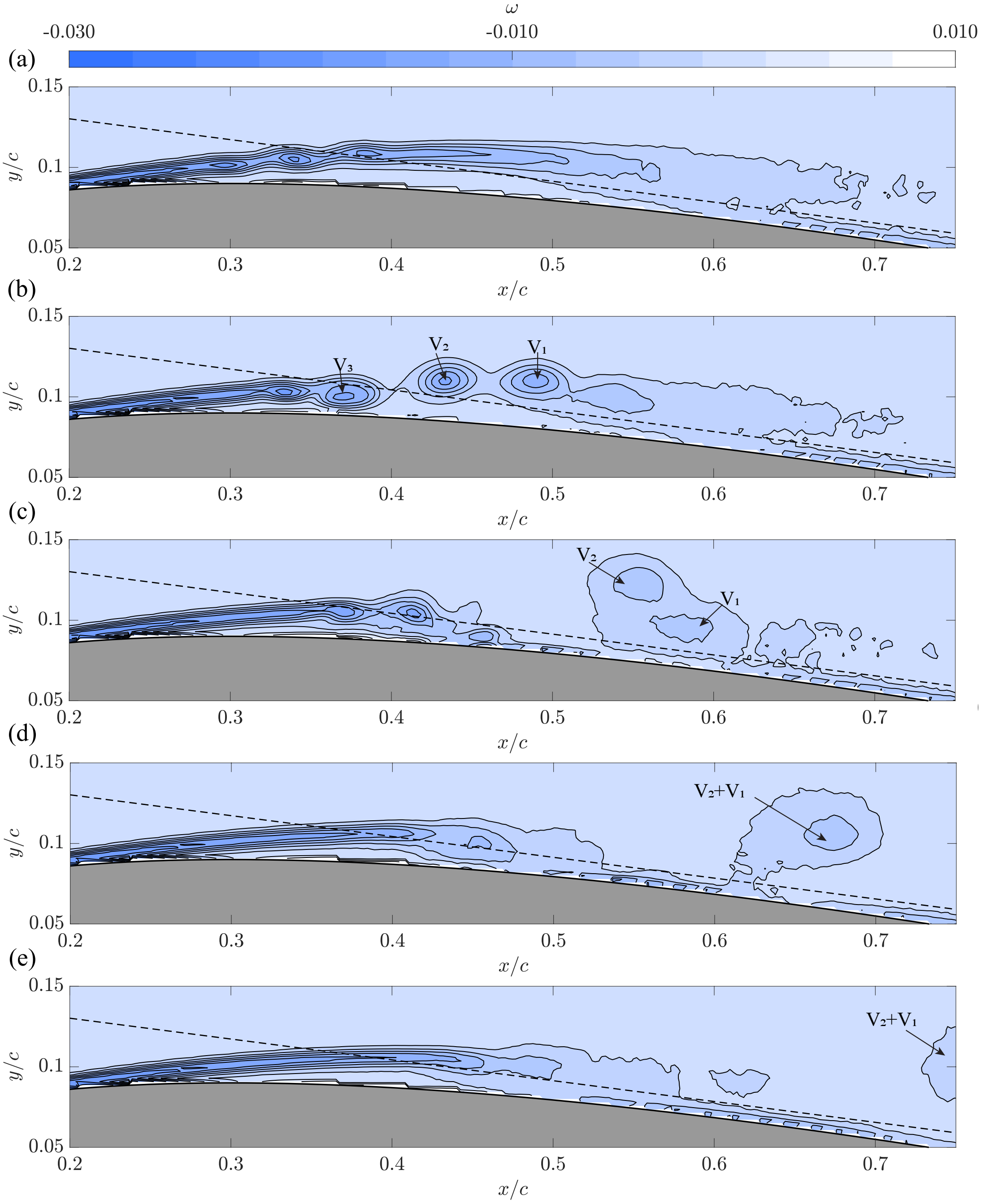

Figure 6.9: Sequence of wall-normal plane vorticity fields showing evolution of shed vortices at $f^+ = 0.19$. (a) $\phi = 1$ (b) $\phi = 2$ (c) $\phi = 3$ (d) $\phi = 4$ (e) $\phi = 5$. The annotations in the figure qualitatively track the interaction of vortices and their interaction throughout the phases. The inclined dashed line near the airfoil shows the position of the wall-parallel plane.

Hence, for a low forcing frequency with a free shear layer at a sufficient distance from the airfoil, the wall-parallel plane is informative during the initial phases, as at later phases, the vortices evolve and move out of the plane. Hence, studying the vorticity field in this forcing frequency range can provide limited information regarding breakdown and further flow development. The phase-averaged u and w wall-parallel velocity fields are used to discuss the evolution of the actuated wave packet as it convects downstream. The w-component is found to be more indicative of breakdown and is used for discussion hereafter, as it highlights the three-dimensionality of

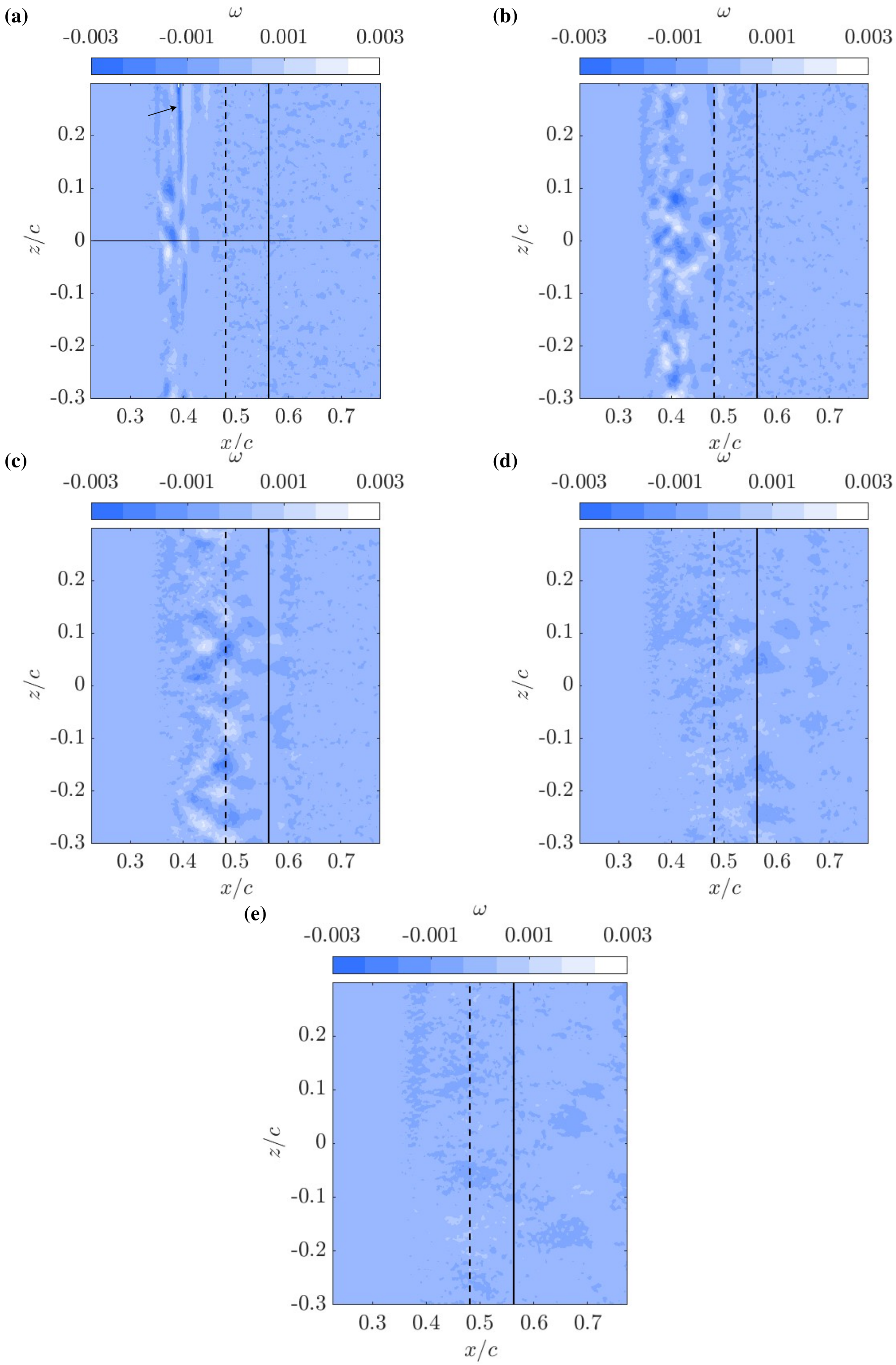

Figure 6.10: Sequence of wall-parallel plane vorticity fields showing evolution and breakdown of shed vortices for at $f^+ = 0.19$. (a) $\phi = 2$ (b) $\phi = 3$ (c) $\phi = 4$ (d) $\phi = 5$ (e) $\phi = 6$. Horizontal line at $z/c = 0$ in (a) indicates the position of the wall normal plane. The dotted vertical line indicates the time-averaged maximum bubble height, and the solid vertical line indicates the time-averaged reattachment point in wall-normal plane.

the flow. The forced wave packet from the actuator has no w component; hence, all the coherent structures in this component are induced by vortex deformation and breakdown. Though laser and the leading edge misalignment issues exist, their effect is observed over the span. Hence, the three-dimensionality introduced in the w velocity field can be primarily attributed to breakdown. At the center of the wall-parallel plane, higher three-dimensionality is observed than at other locations.

Upon convection through the bubble, the front of the wave packet changes the topology and stability characteristics of the bubble. This is known from literature (Michelis et al., 2017). Hence, the tail of the wave packet following this wave front develops undulations. In $\phi = 3$, the actuated roller is visible at $x/c \approx 0.55$ in the u velocity field, while breakdown is observed between $0.35 \leq x/c \leq 0.45$ in the w velocity field. Additionally, at $x/c \approx 0.35$ in the w velocity field, a structure with small undulations is visible, which could correspond to the tail of the wave packet. High two-dimensionality with small undulations of the structure maybe because of the recent onset of secondary instability. The characteristic spanwise wavelength of the coherent structures, quantifying breakdown, varies as they convect downstream. By $\phi = 4$ (w velocity field), the wave front has moved downstream and the trailing structures have broken down. The u-plane shows distinct peak valley patterns at $x/c = 0.55$. However, in the w-velocity plane, the structures form a staggered pattern visible between $x/c = 0.4$ to 0.5. Such a pattern was also noted by Borgmann et al. (2022) in their experiments, where they note that their observed pattern resembles the staggered pattern formed due to classical subharmonic resonance of a boundary layer. Though they observe the formed pattern when forcing at fundamental frequency, the pattern observed here is at a lower forcing frequency. This concludes the discussion of wave packet evolution for $f^+ = 0.19$.

Next, the phase-averaged vorticity fields are analyzed for the intermediate forcing frequency $f^+ = 2.26$. Downstream of formation, the vortices undergo changes that are evident in both planes. The wall-normal vorticity fields are presented in figure 6.12, showing sequence of vortex evolution. At $\phi = 1$, the shear layer is near the airfoil, and previous studies (Diwan and Ramesh, 2009; Yarusevych and Kotsonis, 2017) associate such a configuration with lower amplification rates of natural disturbances. By $\phi = 2$, three distinct rollups are observed in the shear layer. Following the same procedure as before, the vortex V_2 is estimated to be the primary vortex generated from the wave packet. As the phase progresses $\phi = 3$, V_2 convects downstream and reaches the mean reattachment point, causing the following vortex to break down. This is observed in the wall-parallel plane. Vortex merging is not observed in this case. The separation between the shed vortices V_1 and V_2 increases while convecting downstream, as visible in the vorticity fields of $\phi = 3$ and $\phi = 4$. At $\phi = 5$, the vortices emanating from the next wave packet are evident, giving much less time for recovery compared to the forcing frequencies lower than this case.

In the wall-parallel plane, the initial signature of vortex V_2 is identified in the wall-parallel plane at $(x/c) \approx 0.43$ of $\phi = 2$ (figure 6.13a) indicated by arrows. This matches with its location in the wall-normal plane. As the phase progresses, the vortex V_2 breaks down as seen near $x/c \approx 0.5$ of $\phi = 3$. An interesting observation is the breakdown signature observed for the vortex V_2 at $x/c \approx 0.5$ of $\phi = 3$ and the following shear-layer rollup at $x/c \approx 0.5$ of $\phi = 4$. This difference in breakdown characteristics may be attributed to the presence of the enforced normal mode in vortex V_2. As the vortex V_1 and V_2 convect further downstream, only the outer layer of the core resulting from the diffusive growth is visible in the later phases ($\phi = 4, 5$). However, in $\phi = 6$ the breakdown of the next wave packet is evident, corroborating the less recovery of the bubble as seen in the wall-normal plane.

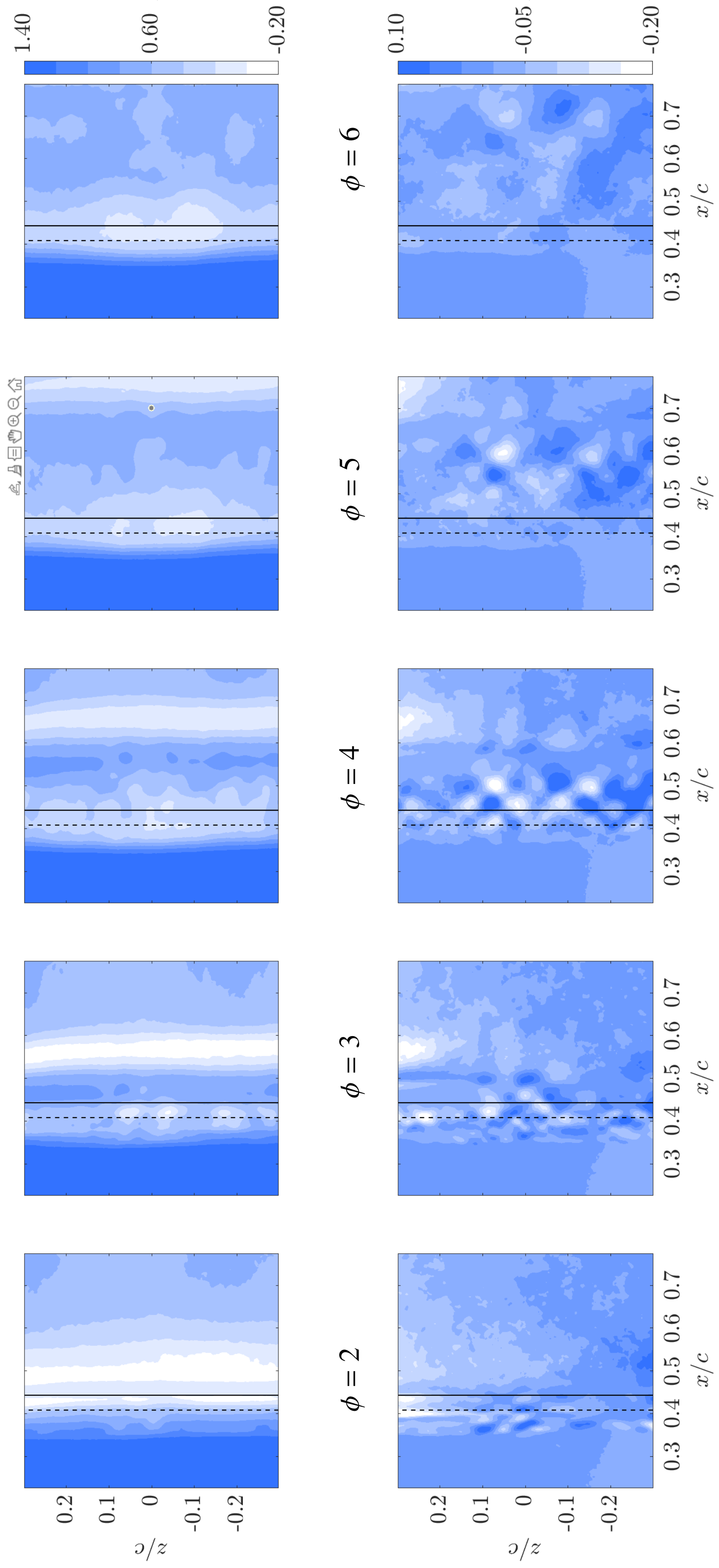

Figure 6.11: Sequence of velocity fields showing evolution of the wave packet for $f^+ = 0.19$. The dashed line indicates the time-averaged maximum height of the bubble, and the solid line indicates the time-averaged reattachment point in the wall-normal plane.

The wall-parallel velocity fields, presented in figure 6.14. The coherent structure size increases downstream, which is attributed to the diffusive growth of the vortices downstream and their distance from the wall-parallel plane. In $\phi = 2$ coherent structures corresponding to the actuated wave packet are observed at $x/c = 0.40$. As they convect downstream, these structures break down, which is observed in $\phi = 3$ at $x/c \approx 0.52$. Diffusive growth continues in $\phi = 4$ with increasing structure separation at $x/c = 0.60$. By $x/c = 0.70$ in $\phi = 5$ structures have separated further and cores have moved away from the wall. In $\phi = 6$ the observed breakdown at $x/c \approx 0.50$ is associated with the next wave packet.

A notable observation in both vorticity and velocity fields is the difference in the breakdown pattern as compared to the low forcing frequency cases. This is later quantified using wavelet analysis. Because the bubble lacks recovery time, the shear layer remains closer to the wall. This may limit the oblique-mode influence and hence change the breakdown characteristics. By contrast, at lower frequencies, the tail of the wave packet encounters a different bubble state and therefore a different growth rate and breakdown pathway. At $f^+ = 3.40$, interactions between consecutive wave packets would become visible in both the planes. This is not presented here due to the unavailability of experimental data in the wall-normal plane. This concludes the discussion of wave packet evolution for $f^+ = 2.26$.

Effects of leading-edge and laser-sheet misalignment persist, yielding spanwise non-uniformity observation of structures across z/c. This is more prominent in the u-component: in $\phi = 2$ at $x/c = 0.5$, the actuated streamwise structures or rollers appear tapered. This concludes the discussion of wave packet evolution for $f^+ = 2.26$.

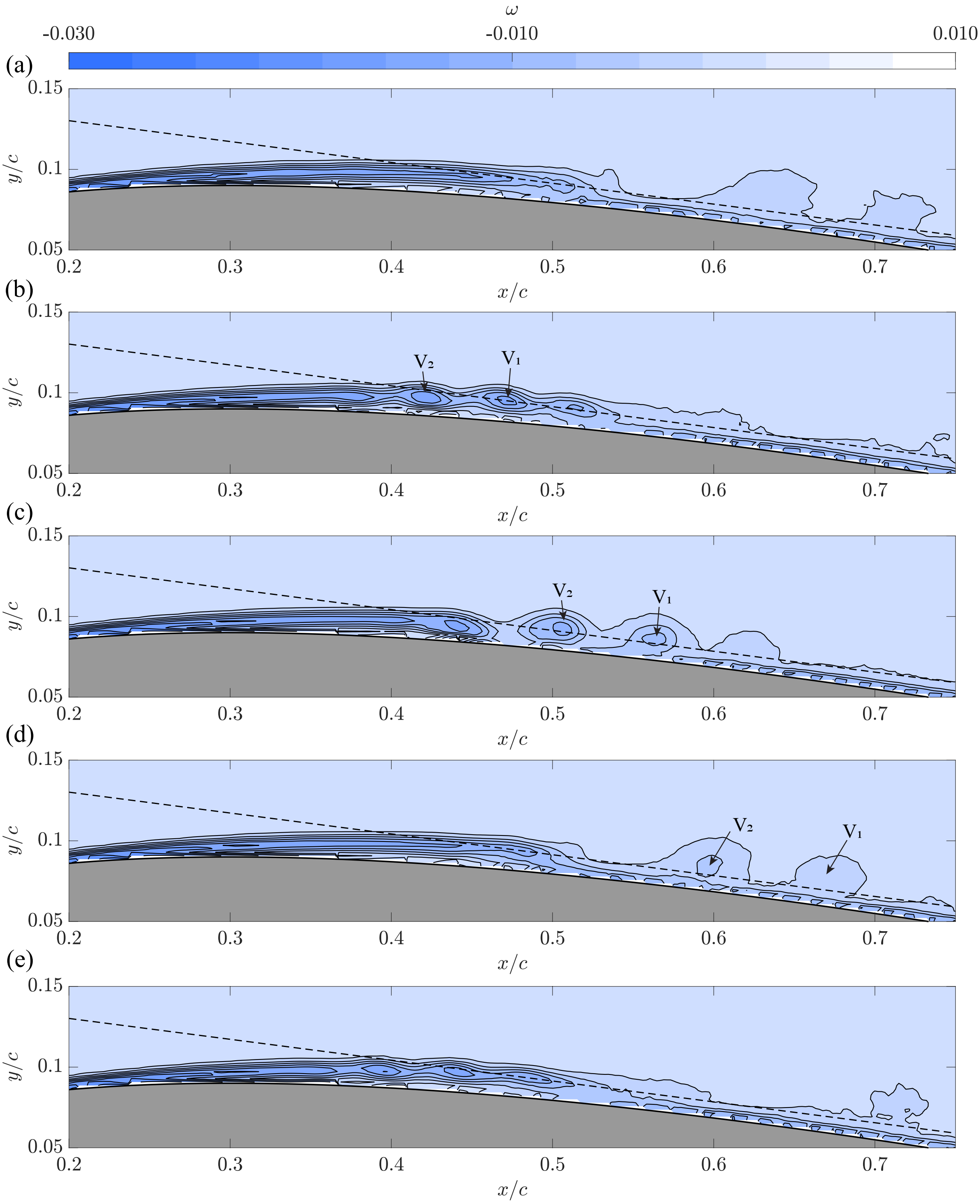

Figure 6.12: Sequence of wall-normal plane vorticity fields showing evolution of shed vortices for $f^+ = 2.26$. (a) $\phi = 1$ (b) $\phi = 2$ (c) $\phi = 3$ (d) $\phi = 4$ (e) $\phi = 5$. The annotations in the figure qualitatively track the interaction of vortices and their interaction throughout the phases. The inclined dashed line near the airfoil shows the position of the wall-parallel plane.

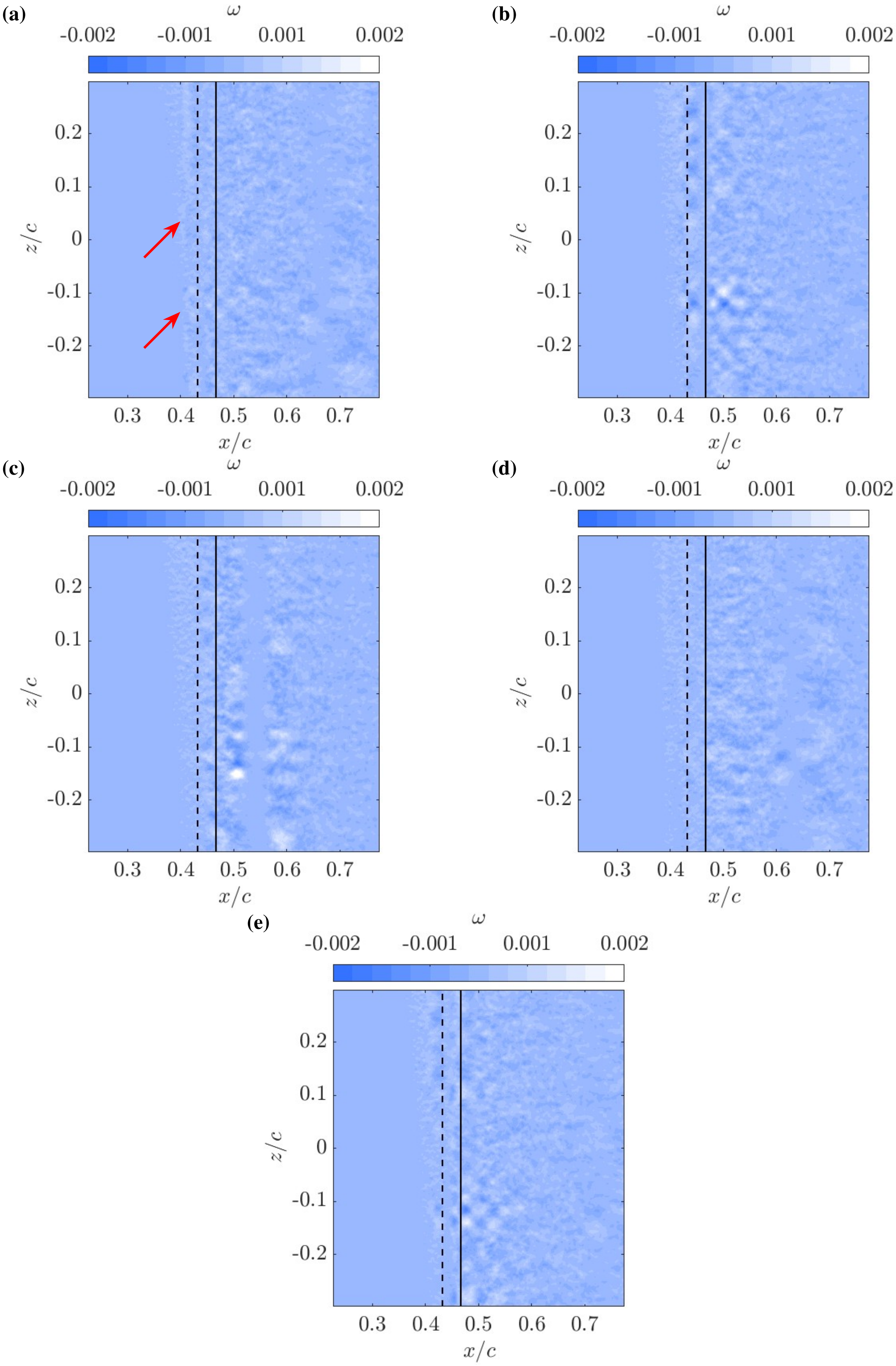

Figure 6.13: Sequence of wall-parallel plane vorticity fields showing evolution and breakdown of shed vortices for at $f^+ = 2.26$. (a) $\phi = 2$ (b) $\phi = 3$ (c) $\phi = 4$ (d) $\phi = 5$ (e) $\phi = 6$. Horizontal line at $z/c = 0$ in (a) indicates the position of the wall normal plane. The dotted vertical line indicates the time-averaged maximum bubble height, and the solid vertical line indicates the time-averaged reattachment point in the wall-normal plane.

The wall-normal vorticity fields for the near subharmonic forcing frequency $f^+ = 4.52$ are presented in figure 6.15 and analyzed. Since the wave packets overlap, the bubble cannot recover, and the shear layer stays at a constant distance from the wall without varying over phases. Since the wave packets interact, a modulated shedding could happen. This draws inference from a similar study by Michelis et al. (2018) whose modal analysis showed modulated shedding. As seen in $\phi = 1$ multiple vortices form and convect downstream. The vortex V_2 is deemed the primary vortex actuated by the packet based on convective speed. As the vortices V_1 and V_2 convect downstream, they approach and subsequently merge, forming a larger vortex that grows diffusively before breaking down. While this merging event happens further downstream, another merging event is evident in $\phi = 1$ at $x/c = 0.4 - 0.5$ with the resulting structure at $x/c \approx 0.58$ in $\phi = 2$. This merging behavior is different than the merging observed for $f^+ = 0.19$, where the vortices co-rotate far away from the airfoil surface before merging, indicating a diminished influence of variation in convection velocity and airfoil curvature. Hence, the driving factor may be saturation of the subharmonic mode due to forcing at the near-subharmonic forcing frequency (Kurelek et al., 2019). They state that subharmonic forcing directly affects the intended mode without relying on secondary energy cascading.

In the wall-parallel vorticity field, shown in figure 6.16, initial undulation appears in $\phi = 2$ for V_1 at $x/c = 0.48$. As V_2 convects downstream, it breaks down into smaller scales ($x/c = 0.5 - 0.6$ for $\phi = 3$ under the action of secondary instability mechanisms. In $\phi = 3$ and $\phi = 4$, structures indicating vortex merging are also evident in the wall-parallel plane as V_1 and V_2 approach and merge. By $\phi = 6$ near $x/c = 0.7$, structures have broken down and are weak. Since the bubble has no time to recover, the instability growth rate does not vary between consecutive packets, and the observed variation in breakdown as compared to previous cases may be attributed to any existing modulation. This concludes the discussion of wave packet evolution for $f^+ = 4.52$.

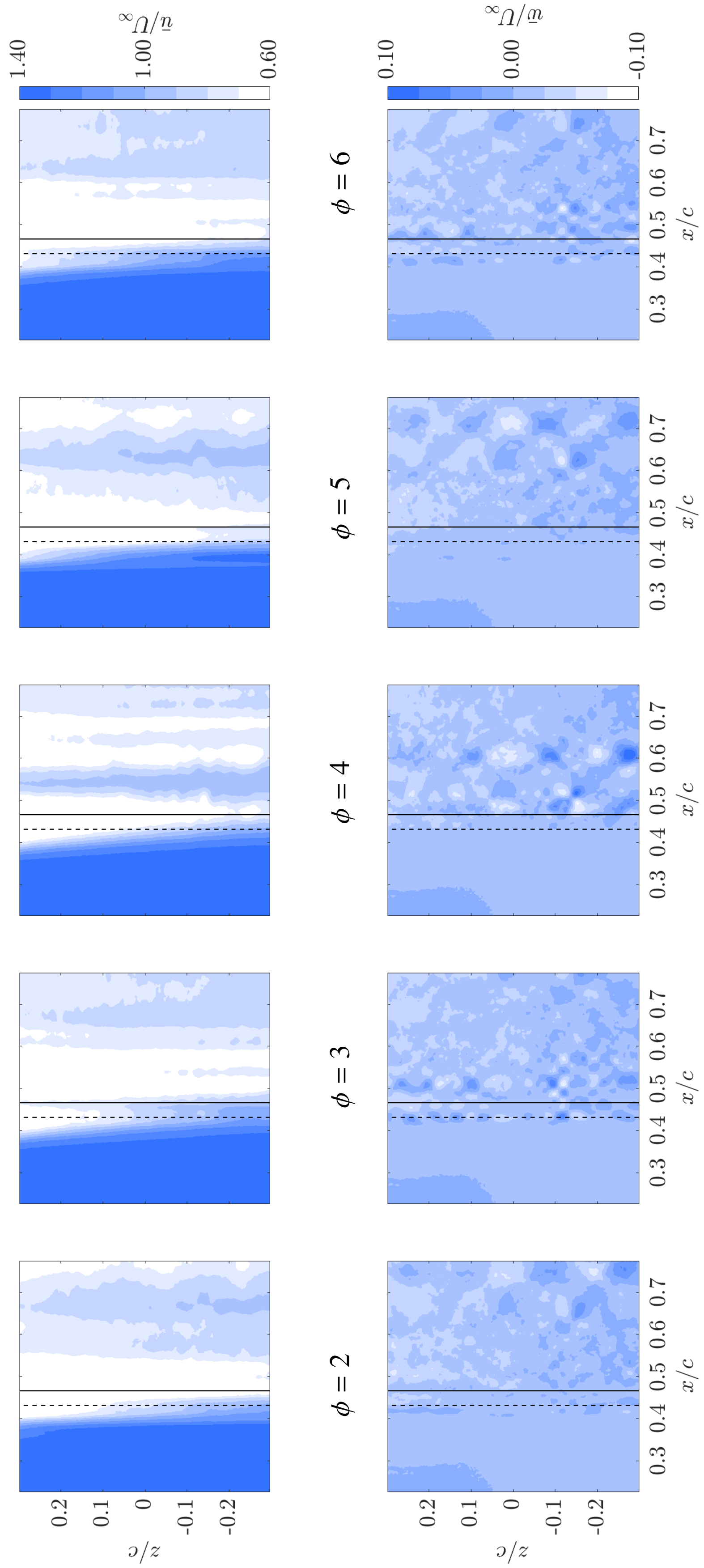

Figure 6.14: Sequence of velocity fields showing evolution of the wave packet for $f^+ = 2.26$. The dashed line indicates the time-averaged maximum height of the bubble, and the solid line indicates the time-averaged reattachment point in the wall-normal plane.

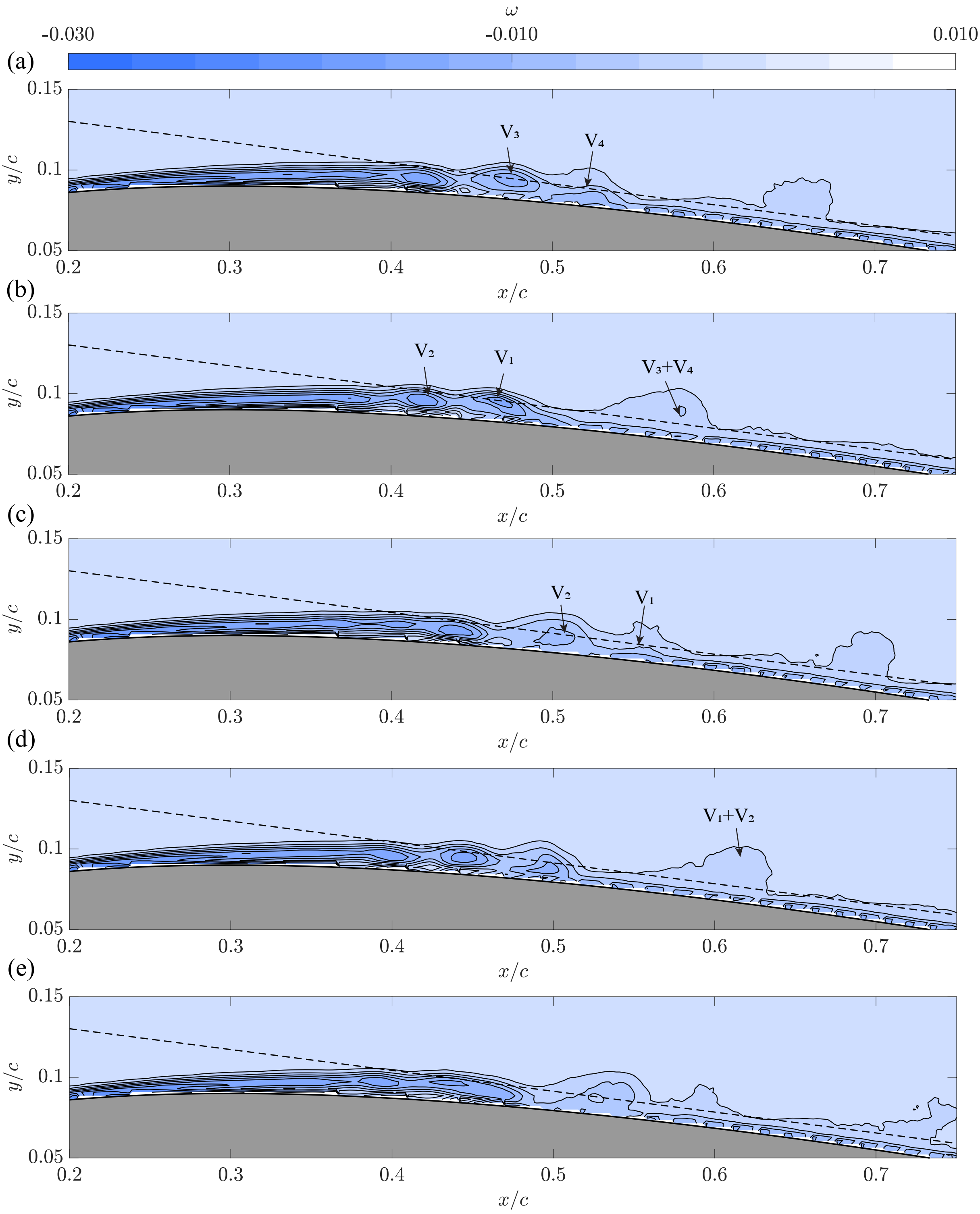

Figure 6.15: Sequence of wall-normal plane vorticity fields showing evolution of shed vortices for $f^+ = 4.52$. (a) $\phi = 1$ (b) $\phi = 2$ (c) $\phi = 3$ (d) $\phi = 4$ (e) $\phi = 5$. The annotations in the figure qualitatively track the interaction of vortices and their merging throughout the phases. The inclined dashed line near the airfoil shows the position of the wall-parallel plane.

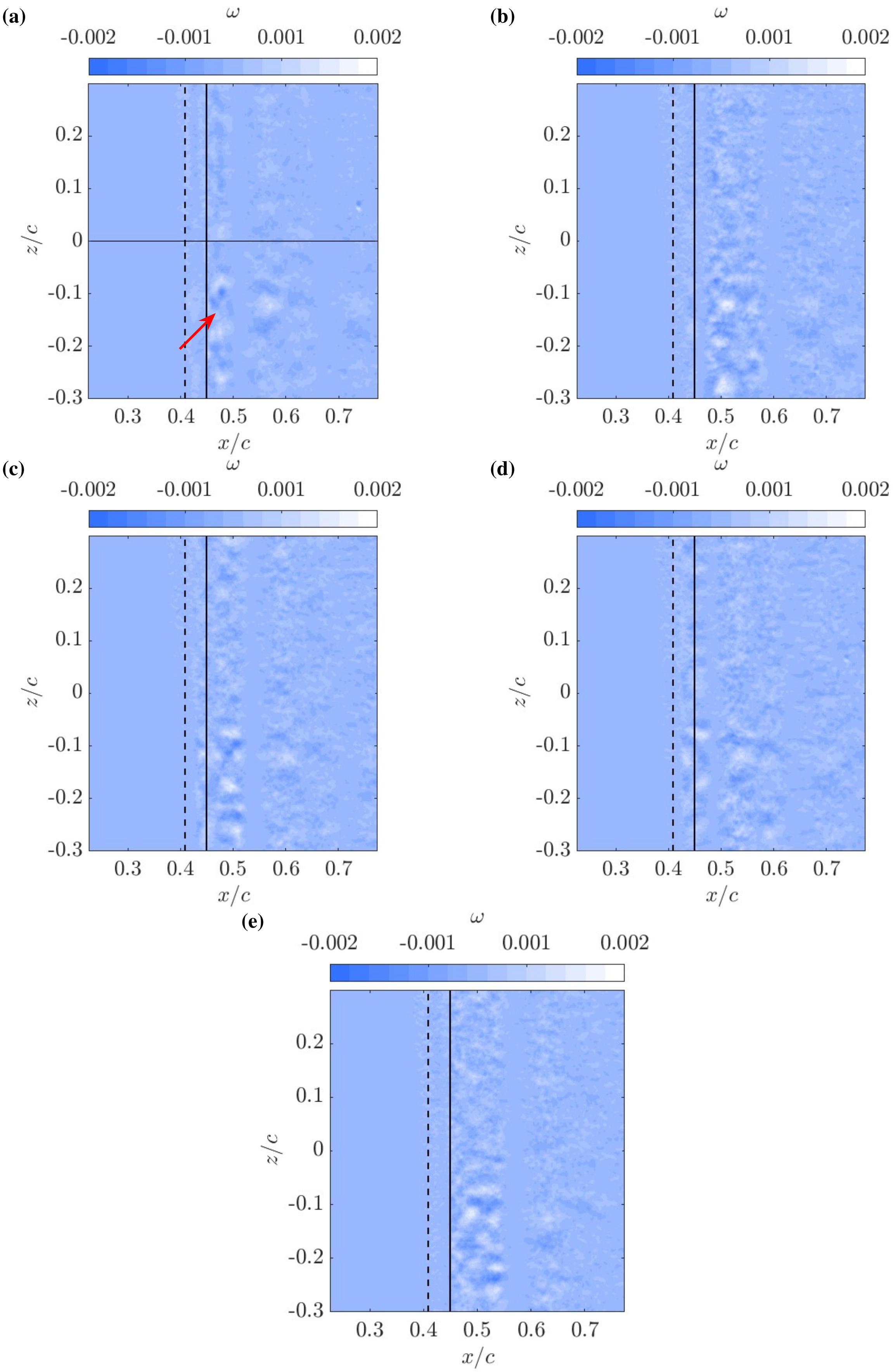

Figure 6.16: Sequence of wall-parallel plane vorticity fields showing evolution and breakdown of shed vortices for at $f^+ = 4.52$. (a) $\phi = 2$ (b) $\phi = 3$ (c) $\phi = 4$ (d) $\phi = 5$ (e) $\phi = 6$. Horizontal line at $z/c = 0$ in (a) indicates the position of the wall normal plane. The dotted vertical line indicates the maximum bubble height, and the solid vertical line indicates the mean reattachment point in wall-normal plane.

Finally, the sequence of vortex shedding for the fundamental forcing frequency is presented in figure 6.17 in the wall-normal plane. As the shed vortices convect, vortex merging is inhibited in the aft part of the airfoil. This behavior is consistent with findings reported in the literature (Kurelek et al., 2019). This behavior is also indicative of lock-in of the actuated wave packet to the shear layer instability (Borgmann et al., 2025). Additionally, lock-in also minimizes cycle-to-cycle variability in shedding.

The wall-parallel plane sequence is presented in figure 6.18. As this vortex convects downstream, normal mode saturation induces earlier transition, and a breakdown is observed at $x/c \approx 0.5$ in $\phi = 3$. The observed breakdown pattern is different from the lower and subharmonic frequency breakdown characteristics. While in a low forcing frequency, the oblique modes may dominate the breakdown; for subharmonic forcing, the modulation and subsequent merging may affect the breakdown of shed vortices. Hence, the differences in forcing frequency lead to different breakdown characteristics. Despite the difference in the breakdown mechanism, signatures of hairpin structures are observed at $x/c \approx 0.55$ of $\phi = 2$. In the wall-parallel u velocity-field, the actuated structures appear evenly spaced (e.g., in $\phi = 2$ $\Delta(x/c) = 0.05$) with distinct peak-valley patterns indicating in and out of plane and spanwise motion. This motion in the w-field corroborates this observation.

While comparing the time-averaged bubble shape, a notable observation emerges: the bubble areas at the near-subharmonic $f^+ = 4.52$ and fundamental (harmonic)$f^+ = 10.19$ forcing frequencies are similar. Kurelek et al. (2019) state a similar observation in their work, which they attribute to equal momentum transfer in both cases due to vortex merging in the subharmonic forcing case.

Fundamental forcing sustains stronger structures farther downstream compared to other forcing frequencies. This is visible in velocity fields presented in figure 6.19 and 6.14. A staggered breakdown pattern appears in the w velocity field at $x/c \approx 0.55$ of $\phi = 2$, which was also observed by Borgmann et al. (2022). They relate the pattern formation to classical subharmonic resonance of a boundary layer. Additionally, a distinct checkerboard pattern is observed downstream of breakdown in the w velocity fields at $x/c \approx 0.55$ of $\phi = 2$. A similar observation was made by Borgmann et al. (2022), who associate this observation with primary wave and dominant oblique mode interaction. This concludes the discussion of wave packet evolution for $f^+ = 10.19$.

Following the flow field analysis, a comparison of bubble topology and breakdown characteristics is done, focusing on mean-flow deformation and wavelength variation for different forcing frequencies. The observed trends and behavior form the basis of further discussion.

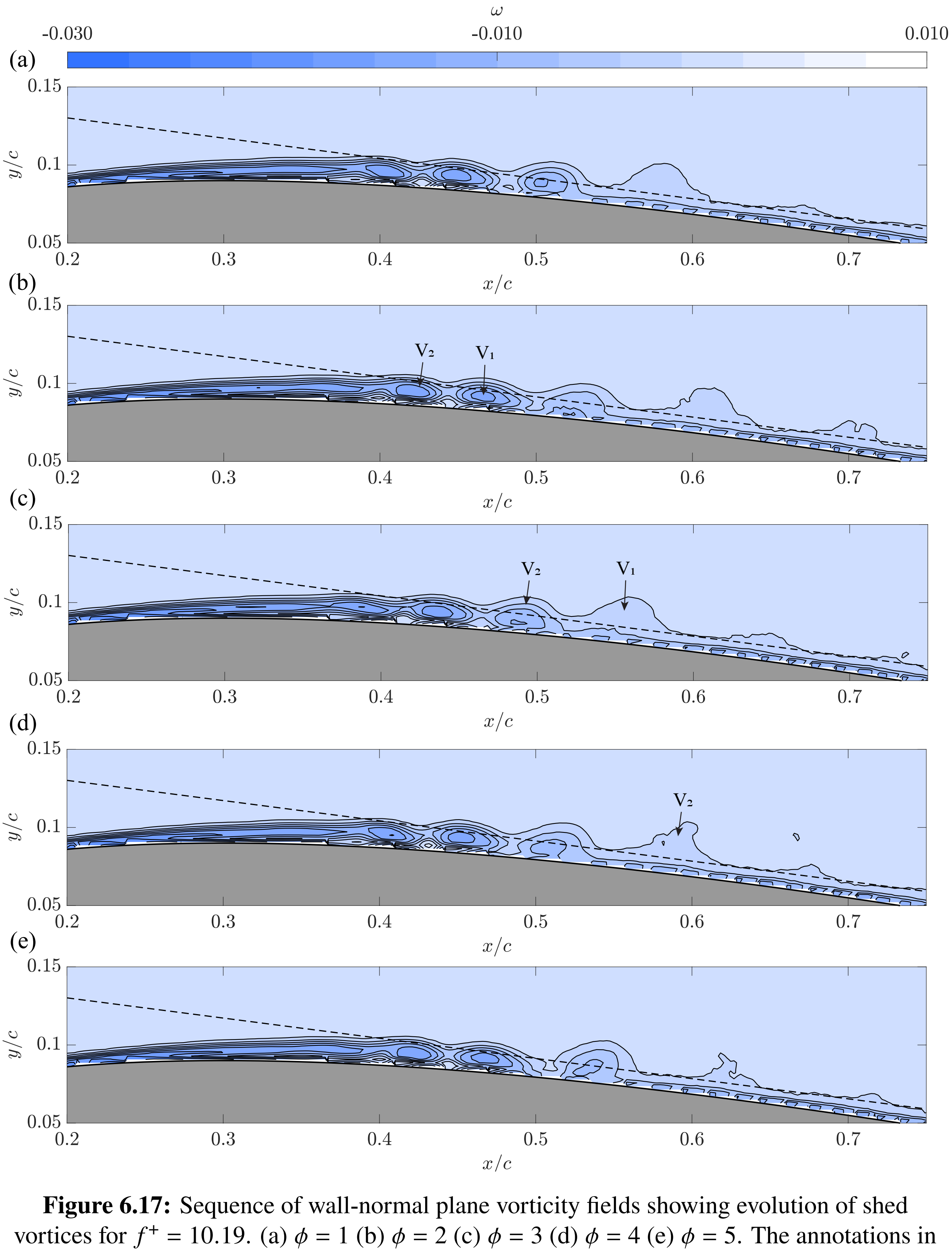

Figure 6.17: Sequence of wall-normal plane vorticity fields showing evolution of shed vortices for $f^+ = 10.19$. (a) $\phi = 1$ (b) $\phi = 2$ (c) $\phi = 3$ (d) $\phi = 4$ (e) $\phi = 5$. The annotations in the figure qualitatively track the interaction of vortices and their merging throughout the phases. The inclined dashed line near the airfoil shows the position of the wall-parallel plane.

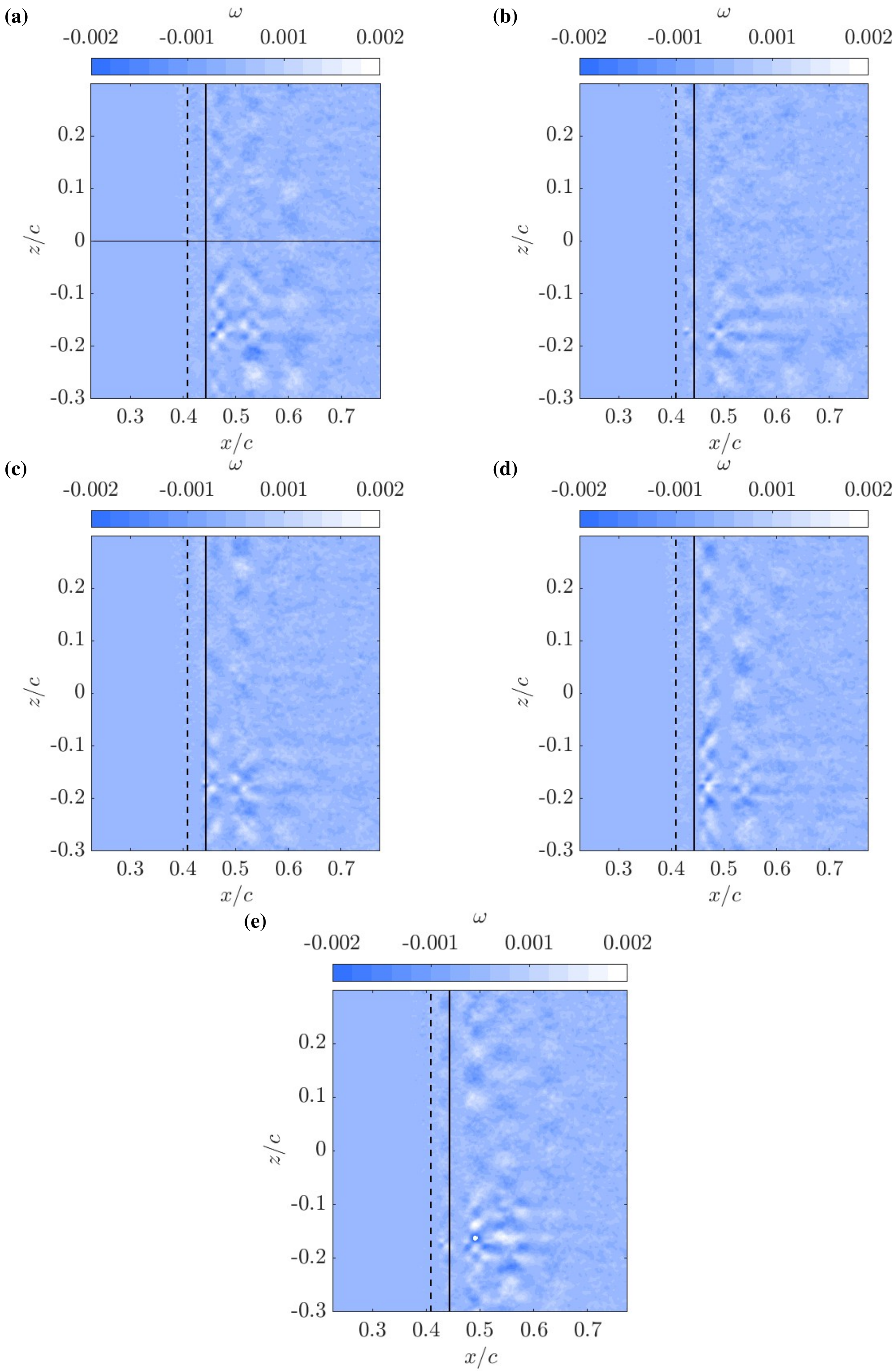

Figure 6.18: Sequence of wall-parallel plane vorticity fields showing evolution and breakdown of shed vortices for $f^+ = 10.19$. (a)$\phi = 2$ (b)$\phi = 3$ (c)$\phi = 4$ (d)$\phi = 5$ (e)$\phi = 6$. Horizontal line at $z/c = 0$ in (a) indicates the position of the wall normal plane. The dotted vertical line indicates the maximum bubble height, and the solid vertical line indicates the mean reattachment point in the wall-normal plane.

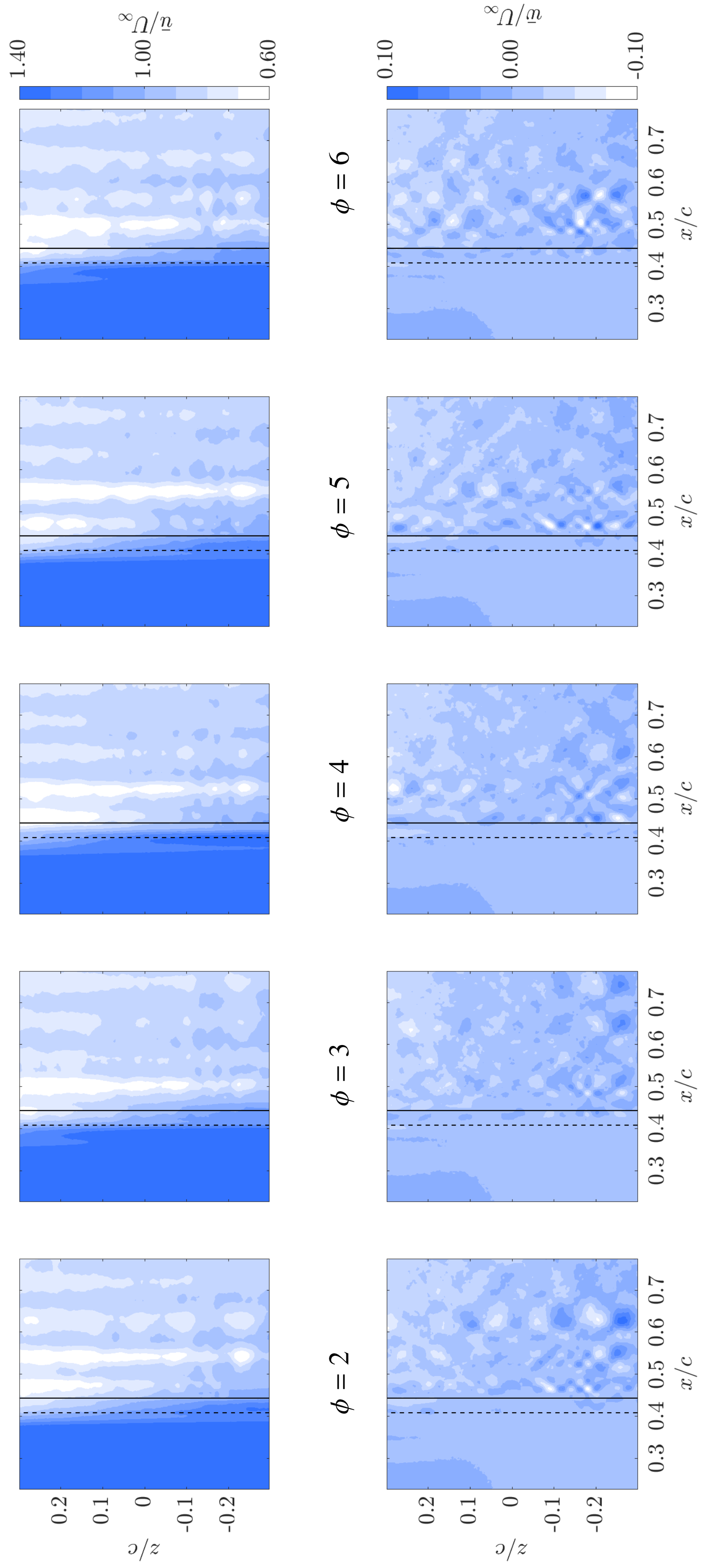

Figure 6.19: Sequence of velocity fields showing evolution of the wave packet for $f^+ = 10.19$. The dashed line indicates the maximum height of the bubble, and the solid line indicates the mean reattachment point in the wall-normal plane.

6.3 Changes in Bubble topology

The effect of periodic forcing on the LSB is assessed through its impact on the time-averaged state of the bubble. The changes in bubble size and boundary-layer integral quantities quantify the mean flow deformation and change in the shear layer stability respectively. Several studies (Marxen and Rist, 2010; Marxen and Henningson, 2011; Michelis et al., 2017) state that changes in the mean state change the breakdown pathway, as the vortex shedding and its breakdown-driven reattachment depend on the disturbance growth rates supported by the base flow.

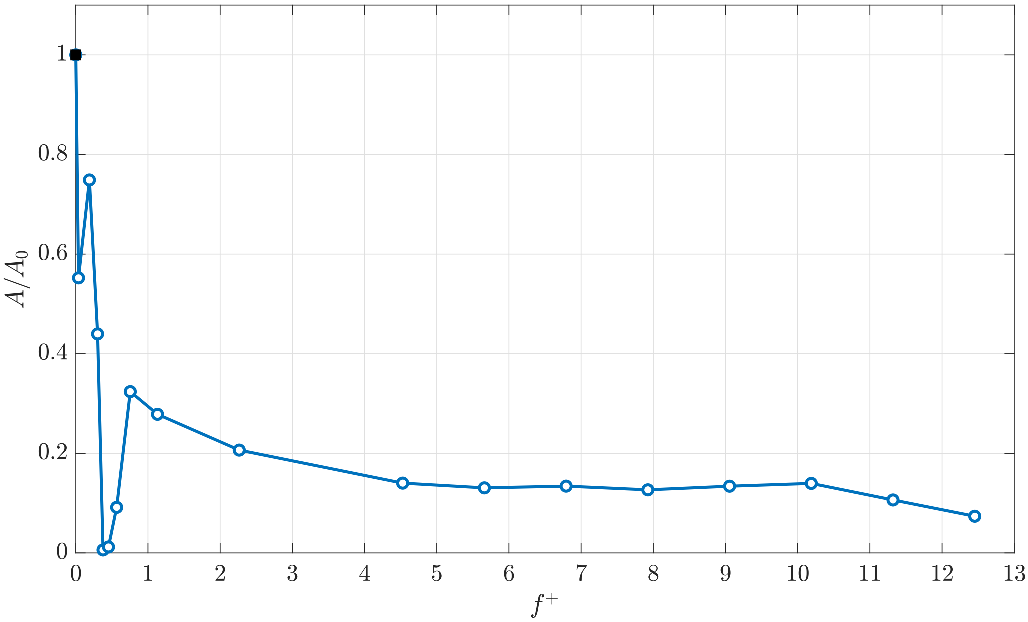

Figure 6.20: Normalised area trend showing the variation of bubble area with different forcing frequencies. The change in area also indicates Mean Flow Deformation with forcing frequency.

Mean flow deformation is quantified by plotting bubble area versus forcing frequency. The bubble area considered is the area enclosed by the bounding streamline of the bubble in the wall-normal plane u velocity field. The bubble area is then normalized by the unforced bubble area and plotted against non-dimensional forcing frequency. A steep decrease in the bubble area is observed in the low forcing frequency regime, followed by a gradual change in the subharmonic and fundamental forcing frequencies. While significant mean flow deformation is observed at $f^+ = 2.26$ (figure 6.6b) with limited recovery of the bubble, at $f^+ = 3.40$ the forced wave packets interact. While previous studies have not studied the variation of the LSB area with forcing frequency, Yarusevych and Kotsonis (2017); Kurelek et al. (2019); Borgmann et al. (2022) show variation of LSB topology in terms of length and height for different forcing frequency regimes.

Outliers are observed at $f^+ = 0.03, 0.37, 0.45, 0.56$. To explain this, the streamwise velocity standard deviation fields are presented in figure 6.21. At $f^+ = 0.37, 0.45, 0.56$, the corresponding actuation frequencies lie above the Nyquist limit of the sampling rate. It is proposed that three factors together produce the behavior: (i) the actuation induces a strong periodic change in the bubble topology, (ii) the response is undersampled, so the true periodic motion appears in the data as a slower effective modulation, and (iii) each realization starts from a different actuation phase and covers a limited fraction of this slow envelope. When all samples are averaged over time, the result spans different bubble states (elongated, compressed, partially broken down), so the standard deviation of u is dominated by differences between these states rather than by small fluctuations around a single mean. This causes the higher standard deviation observed in figure 6.21.

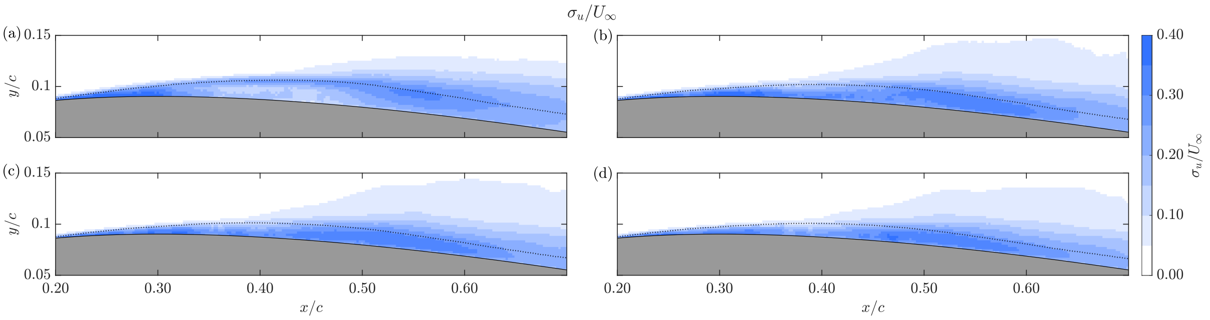

Figure 6.21: Standard deviation fields for dimensional forcing frequency. (a)$f^+ = 0.03$, (b)$f^+ = 0.37$, (c)$f^+ = 0.45$, (d)$f^+ = 0.56$. While the increased values in (b),(c), and (d) is due to alisaing, the increased value at (a) is due to bubble dynamics at an impulsive forcing frequency.

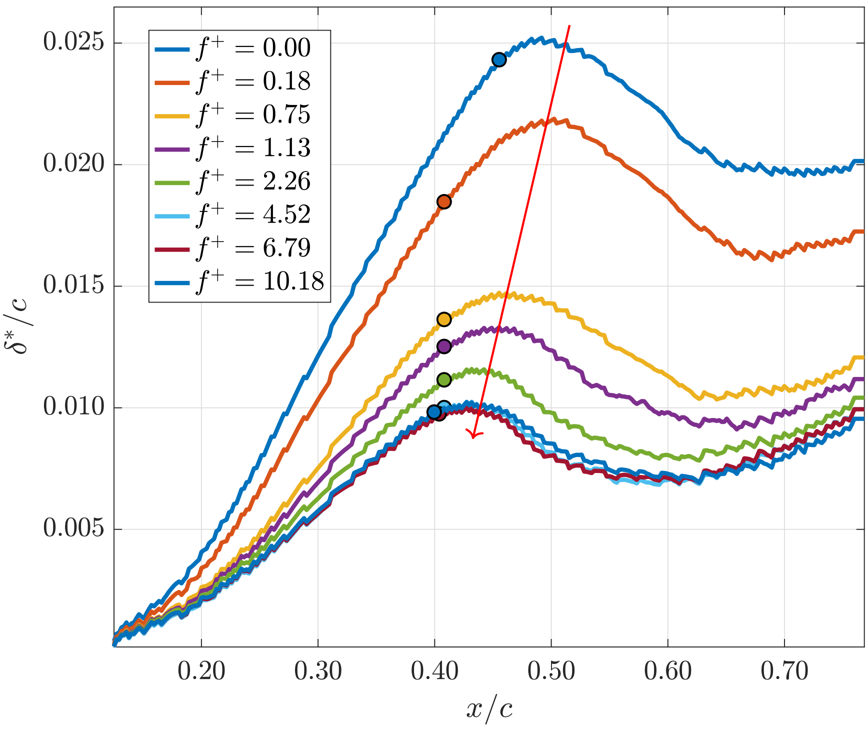

Figure 6.22: Variation of displacement thickness with forcing frequency. The cases shown here include cases discussed for the flow-field characteristics of the forced bubble. The filled circle markers are the maximum shape factor location for the cases.

At $f^+ = 0.03$, the cause of the higher standard deviation is different. The actuation frequency lies below the Nyquist limit, but the forcing triggers a pronounced elongation recovery cycle within each actuation. The bubble shortens early in the cycle and then elongates before recovering to its original state. Hence, the elevated standard deviation reflects these changes in topology within each actuation. Additionally, in the actuation cycle, the bubble is also receptive to natural instabilities. This is not an issue for other low forcing frequency cases, as the bubble does not recover fully between the actuations. Further analysis does not include these outliers.

The displacement-thickness and shape-factor trends indicate stabilization of the base state with increasing forcing frequency. Plotting the displacement thickness against forcing frequency (figure 6.22) shows that δ^* progressively approaches the wall, while the location of the maximum shape factor shifts upstream at higher frequencies relative to lower ones. This behavior is consistent with observations made in previous studies Yarusevych and Kotsonis (2017); Michelis et al. (2017). Furthermore, for the near-subharmonic and fundamental forcing frequencies, the displacement thickness is very similar. This aligns with the similar bubble area observed in the previous section for these two cases.

Using the time-averaged behavior of the bubble, shear-layer, and flow field characteristics observed above, the analysis now discusses how the wave packet interaction regime, in which packet spacing in time and space constrains bubble recovery, biases the breakdown. A recovery-limited regime is observed after $f^+ = 3.40$ in which the interval between consecutive wave packets is insufficient for the bubble to start recovery. In this regime, the shear layer remains near the wall with less phase-to-phase variability, leading to different breakdown characteristics than before this regime.

6.4 Breakdown Characteristics

Breakdown is quantified in terms of streamwise and spanwise wavelengths: variation in streamwise wavelength indicates change in relative motion and merging of vortices, whereas variation in spanwise wavelength indicates undulation and breakdown of the formed spanwise vortex. For this study, the spanwise wall-parallel velocity component (w) is used for quantifying the spanwise breakdown. This is done by extracting the wavelength of the velocity signals using spatial wavelet analysis. The process is explained in detail in section 5.5.2. Velocity signals are extracted at designated windows determined using convective velocity based tracking of the actuated packet through phase. The methodology of fixing the window is described in detail in section 5.5.3. This velocity component is chosen over the vorticity field (a derived quantity) as it gives a clearer indication of three-dimensionalisation of the flow field.

The spanwise wavelength variation with phase is presented in figure 6.23. Based on the distinct trend of wavelength with phase, the experimental matrix is divided into three categories: (i) lower forcing, (ii) subharmonic, and (iii) near-fundamental. This classification is also supported by the observed different breakdown patterns in section 6.2.2.2.

Low forcing range cases exhibit less variation in spanwise wavelength (λ_z) with phase, whereas subharmonic range cases show a distinct “U”-shaped trend due to detected initial coherence, breakdown, and subsequent convection of broken-down structures. As a general observation, it is noted that $\phi = 2$ shows the initial undulations, $\phi = 3$ shows the breakdown, and further phases show the growth of broken-down structures. This observation is common across the categories defined. In the low forcing frequency category, the wavelength remains approximately constant with phase because the extraction window detects the wave packet tail. Hence, only the breakdown of this part of the wave packet is observed over the phases. Due to the fixation of the signal extraction window and the normal-mode enforced vortex (observed at $x/c \approx 0.45$

of figure 6.9b) moves out of plane before its breakdown capture. Additionally, for many low-frequency cases, the shear layer lies partly outside the wall-parallel plane, and the structures projected may introduce a projection-related bias. The slight increase in spanwise wavelength in $\phi = 6$ indicates the vortices outside the wall parallel plane as seen in figure 6.9 and 6.10. Additionally, a part of the increase might be due to merging, but this requires further investigation. With increasing forcing frequency, a notable observation is the coherence spanwise vortices at $\phi = 2$ of $f^+ = 2.26$, as indicated by a high spanwise wavelength. This is due to the shear layer moving close to the wall, and the initial coherence is captured before the onset of breakdown. This can be inferred in the flow evolution presented in figure 6.13, which is representative of this forcing case.

Approaching the forcing frequency where the wave packets interact, the shear layer is closer to the wall. Previous studies say that for such a situation, the growth rate of natural disturbance reduces, and hence a different breakdown characteristic can be expected. While the wave packets start interacting only at $f^+ = 3.40$, the spanwise wavelength trend of $f^+ = 2.26$ is similar to it, as the recovery time is small. This case is discussed in 6.2.2.2. Higher forcing frequency cases in this regime show coherent vortices indicated by a higher spanwise wavelength in $\phi = 2$ of figure 6.23. The vortex breakdown is indicated by small wavelength values in $\phi = 3$. On further convection, the broken-down structures undergo diffusive growth, increasing the wavelength in $\phi = 4, 5, 6$. This variation of wavelength shows a “U”-shaped pattern. A probable reason could be the projection of the hairpin structures onto the wall-parallel plane. Another probable reason could be spanwise undulations, as they play an intrinsic role in vortex merging, which can be non-uniform in span (Kurelek et al., 2019). Though not observed for the current study, time-resolved visualizations may show merged segments coexisting with distinct unmerged segments along the span, yielding spanwise varying wavelength signatures.

In the near-fundamental range, the spanwise wavelength trend is different compared to the low forcing and subharmonic range. In $\phi = 2$, the high spanwise wavelength indicates the initial coherence of the vortex. In $\phi = 3$, there is a dip in spanwise wavelength. $\phi = 4$ and further show an increase in wavelength. A similar observation of an increase in the spanwise wavelength (λ_z) obtained from wall-normal velocity fields by Borgmann et al. (2022), where they observe an increase in wavelength after the time-averaged reattachment location. While the predicted spanwise wavelengths from Secondary Instability Analysis (Herbert, 1988) match the observed experimental data for their case, they did not provide any explanations for such an increase.

With the variation of the spanwise wavelength with phase discussed above, the variation of the streamwise wavelength with different phases is now discussed. As a general observation across the ranges, the streamwise wavelength grows monotonically through the phases. The variation streamwise wavelength is presented in figure 6.24. The gradual increase in the streamwise wavelength for the low forcing category indicates the merging in the aft part of the airfoil, as is visible from the wall normal vorticity field (figure 6.9). Additionally, the increase may also be attributed to the projection of out-of-plane vortices into the wall-parallel plane. In subharmonic cases, the downstream increase is consistent with observed merging. The downstream increase of wavelength in the fundamental range is attributed to the lock-in and gradual separation in the aft part of the bubble. The observed trend matches with observations made in section 6.2.2.2.

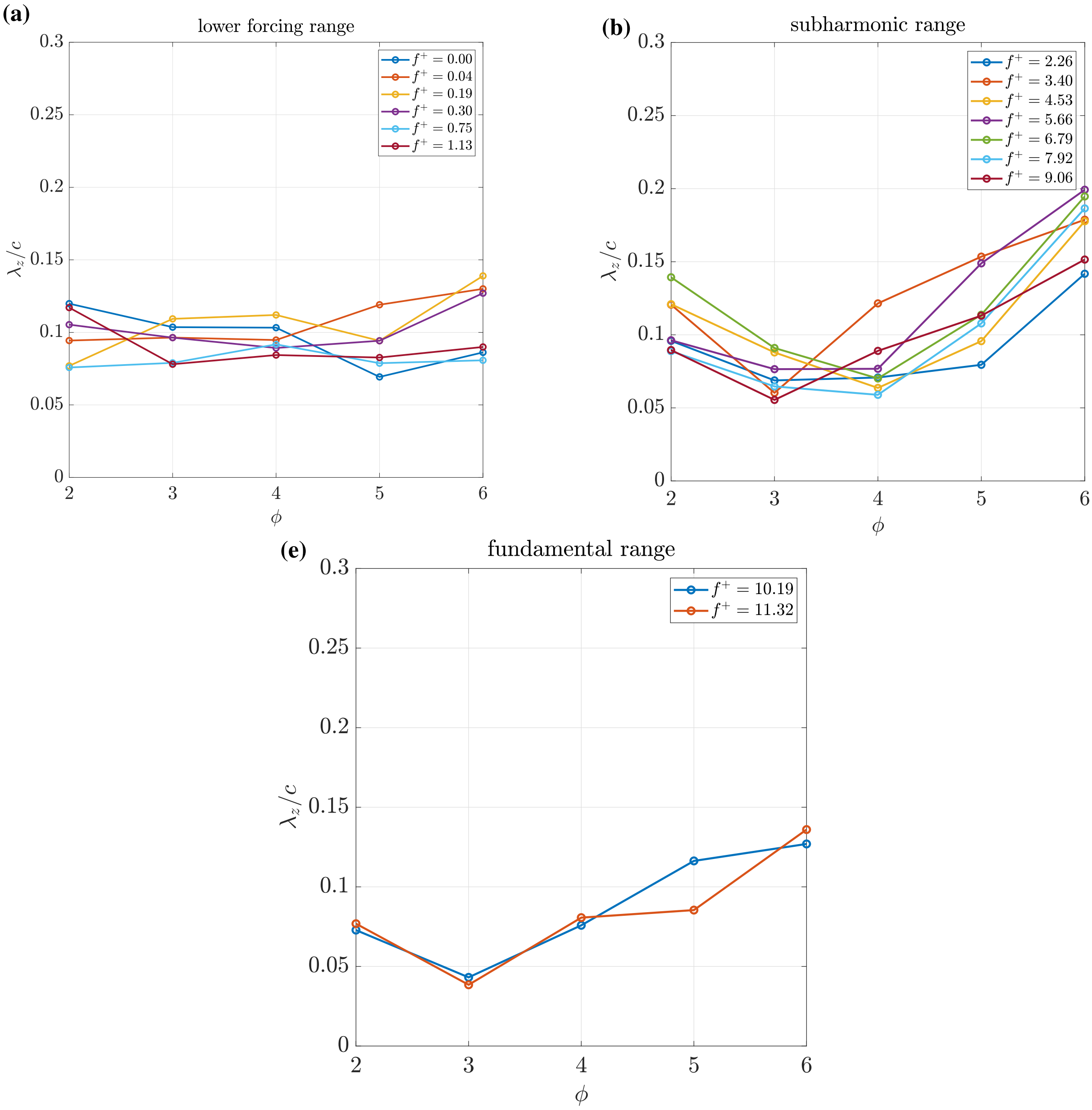

Figure 6.23: Variation of spanwise wavelength with phase for different forcing frequency categories. (a) lower forcing range (b) subharmonic range (c) fundamental range.

After presenting the variations in spanwise (λ_z) and streamwise (λ_x) wavelengths, the variation of their ratio $r = \lambda_z/\lambda_x$ is discussed as a combined indicator of the breakdown. The wavelength ratios are plotted in figure 6.25 for the defined three categories and discussed. For the low forcing range, the wavelengths show a gradual decrease with phase. At $\phi = 2$, the ratio is highest, indicating the initial undulations. From the wall parallel vorticity and velocity field for the category, it is seen that the breakdown occurs at $\phi = 3$. Additionally, the variation of the wavelength of an unforced bubble is included here for reference and comparison. The data for the unforced bubble are obtained from the instantaneous velocity fields, rather than the phase-averaged velocity field. The obtained ratio at the breakdown location in $\phi = 3$ matches well with the previous observations (Michelis et al., 2018; Rodríguez et al., 2021). Since a resemblance is observed between the breakdown of the unforced bubble and the breakdown in the low forcing category, it can be said that the breakdown in the low forcing category follows the breakdown pathway of the unforced bubble, i.e, an oblique mode dictated breakdown (Michelis et al., 2018).

As the structures convect downstream, the ratio decreases because of a subsequent increase in streamwise wavelength as the structures move out of the wall parallel plane or merge to form larger streamwise wavelengths.

For the subharmonic range, a mildly decreasing trend is observed. While it is difficult to obtain a definitive conclusion from this, this trend may be attributed to a possible modulation of the shed vortices and merging, leading to a different breakdown footprint. For the fundamental range, the breakdown characteristics show a similar trend as the subharmonic range.

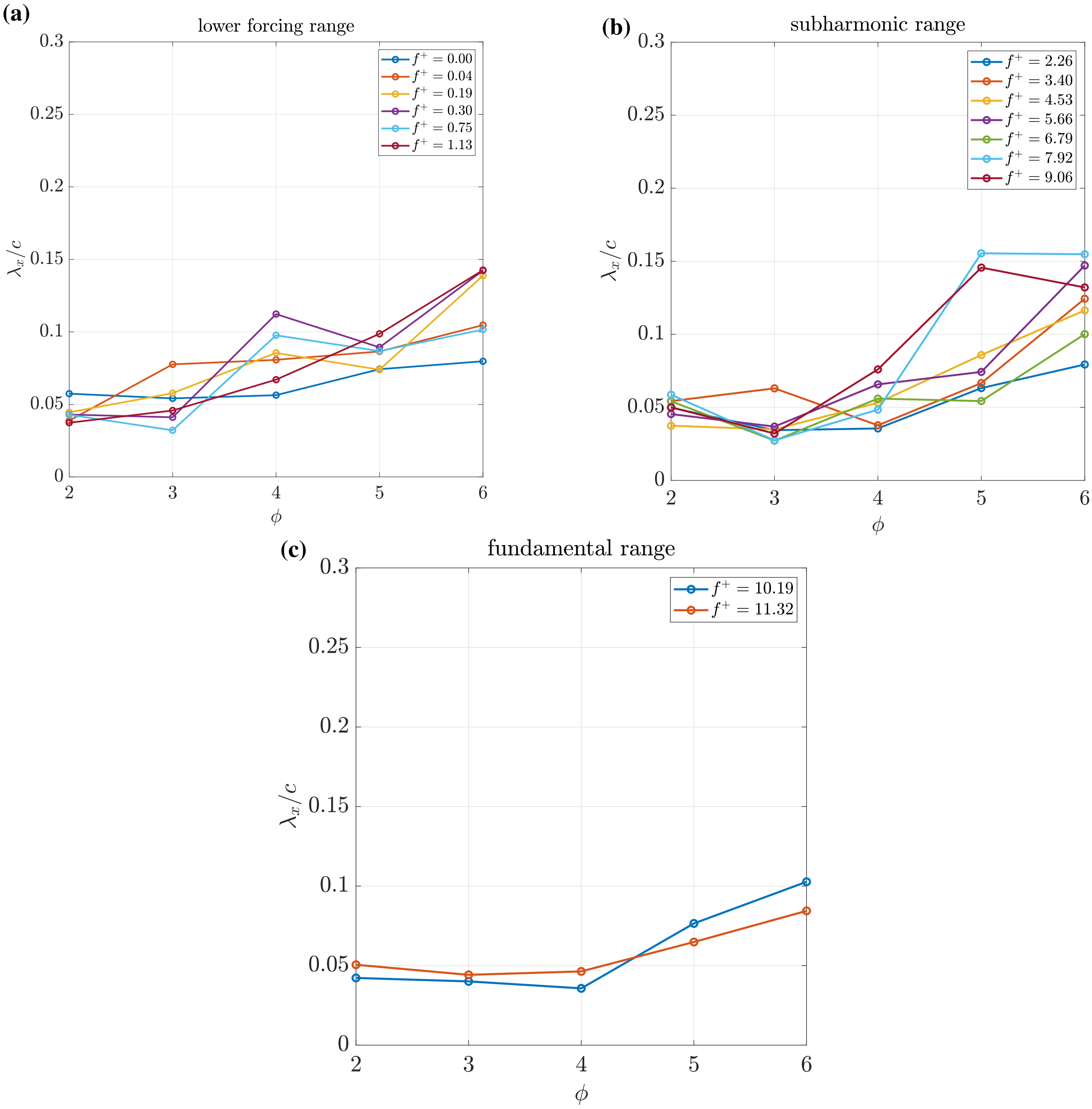

Figure 6.24: Variation of streamwise wavelength with phases for different forcing frequency categories. (a) lower forcing range (b) subharmonic range (c) fundamental range.

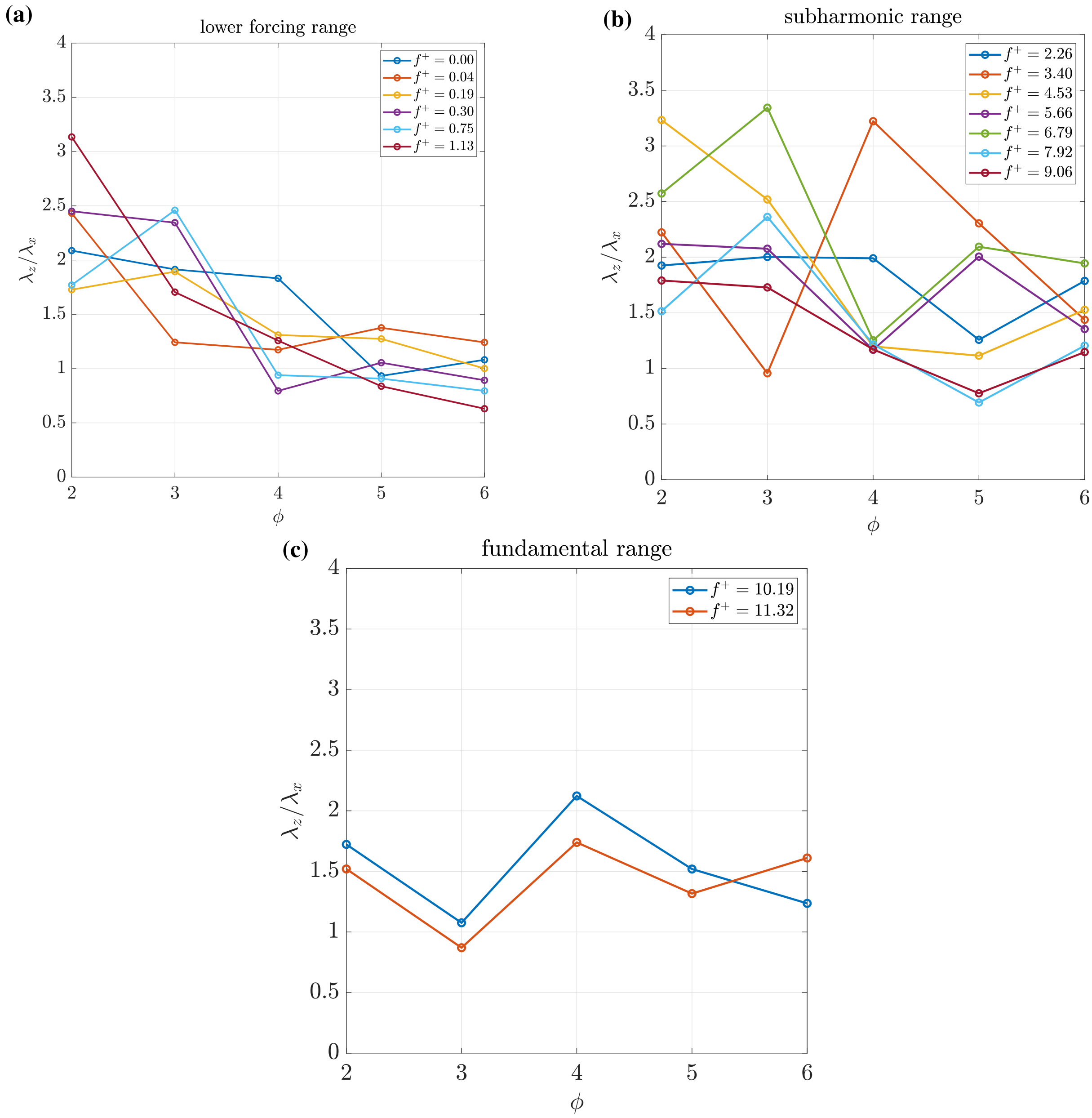

Figure 6.25: Variation of wavelength ratio quantifying breakdown with phases for different forcing frequency categories. (a) lower forcing range (b) subharmonic range (c) fundamental range.

To complement the phase wavelength variation, a wavelength frequency variation is presented and discussed. While the wavelength variation with phase plots captures spatial structure evolution and breakdown, it is difficult to deduce patterns across different forcing frequency regimes. The spanwise wavelength variation is shown in figure 6.26. A similar segregation is done as per the previous observation: lower forcing, subharmonic, and fundamental forcing. In lower forcing frequency, the spanwise wavelength λ_z exhibits a pattern: the wavelength value increases with an increase in phase. This increase occurs as the vortices move out of the plane (figure 6.9). However, as the f^+ increases in the low forcing regime, the shear layer moves close to the airfoil, and the observed wavelength difference between phases decreases.

In the subharmonic range, the shear layer and shed vortices remain closer to the airfoil. The value of λ_z is large at the $\phi = 2$, signaling initial undulations. It reaches a minimum near the

$\phi = 3$, indicating a breakdown, following which it increases again and grows as it convects and the broken down structures undergo diffusive growth. At fundamental forcing, the spanwise wavelength λ_z decreases at $\phi = 3$, indicating a breakdown, following which it increases through phases, yielding the large structures downstream.

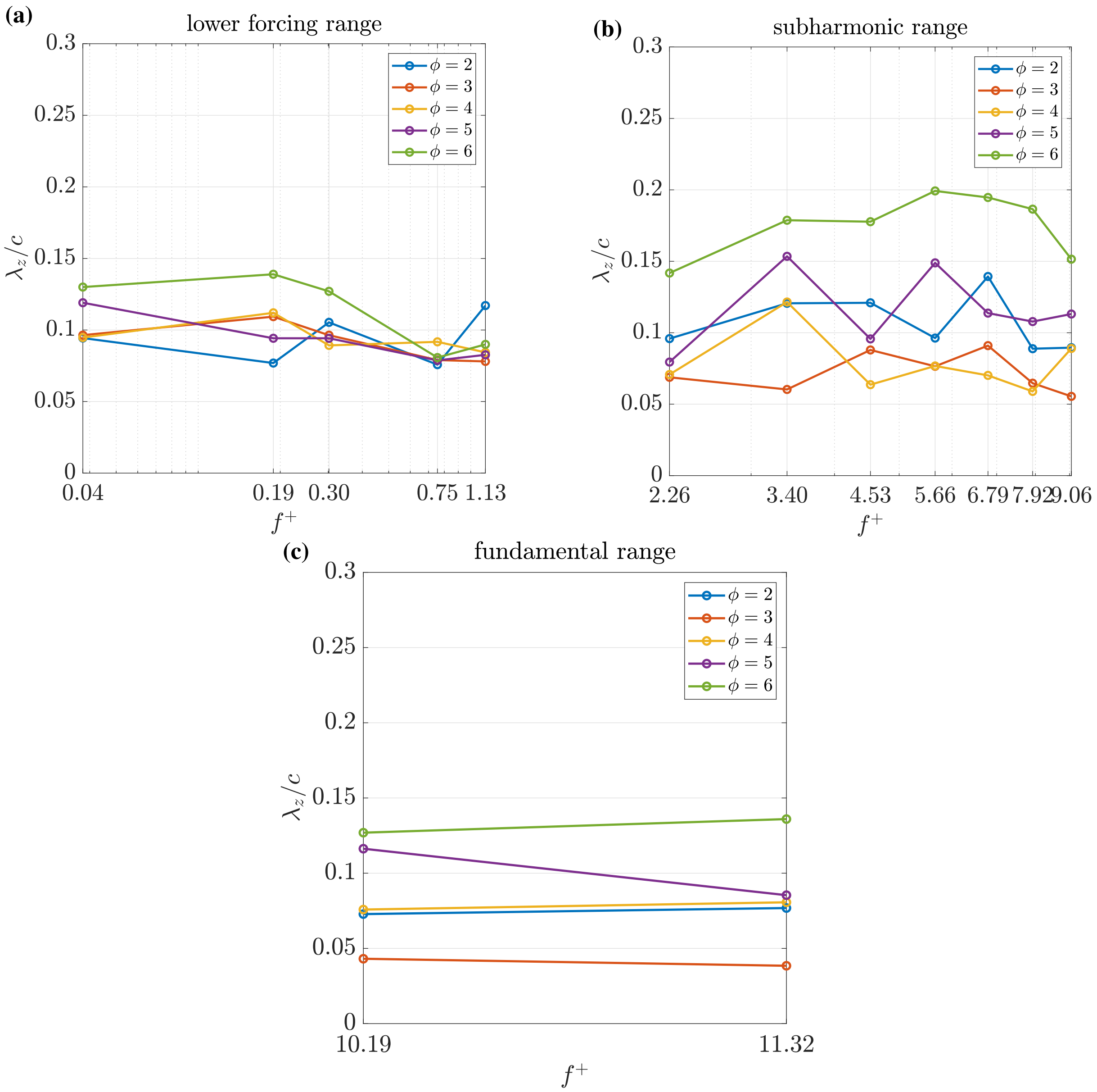

Figure 6.26: Variation of spanwise wavelength quantifying breakdown with forcing frequencies for different phases and forcing frequency categories. (a) lower forcing range (b) subharmonic range (c) fundamental range.

With the spanwise wavelength variation discussed, the streamwise wavelength variation is shown in figure 6.27. In the low forcing frequency category, the streamwise wavelength λ_x shows a clear trend. λ_x is small at the initial phases and increases with phase. At the last phase, the wavelength value has doubled, indicating streamwise vortex merging in the aft part of the flow. In the subharmonic range, at lower forcing frequencies and early phases, λ_x remains small. However, as the phase increases, the $\phi = 3$ shows lower values than $\phi = 2$, indicating breakdown. The higher phases show an increase in wavelength indicative of streamwise merging (Kurelek et al., 2019).

Variation in fundamental forcing shows the monotonic behavior. λ_x is low at early phases and increases with phase, indicating larger streamwise scales downstream.

To characterize the geometry of coherent vortical structures in one parameter, the variation of their ratio r is shown in figure 6.28. In the low forcing frequency case, early phases do not exhibit a particular trend, whereas at later phases the ratio decreases with increasing frequency. In the subharmonic range, the ratio decreases with increasing frequency at the mid and late phases, while early phases show no robust trend. For fundamental forcing, definitive conclusions cannot be drawn for all ratios.

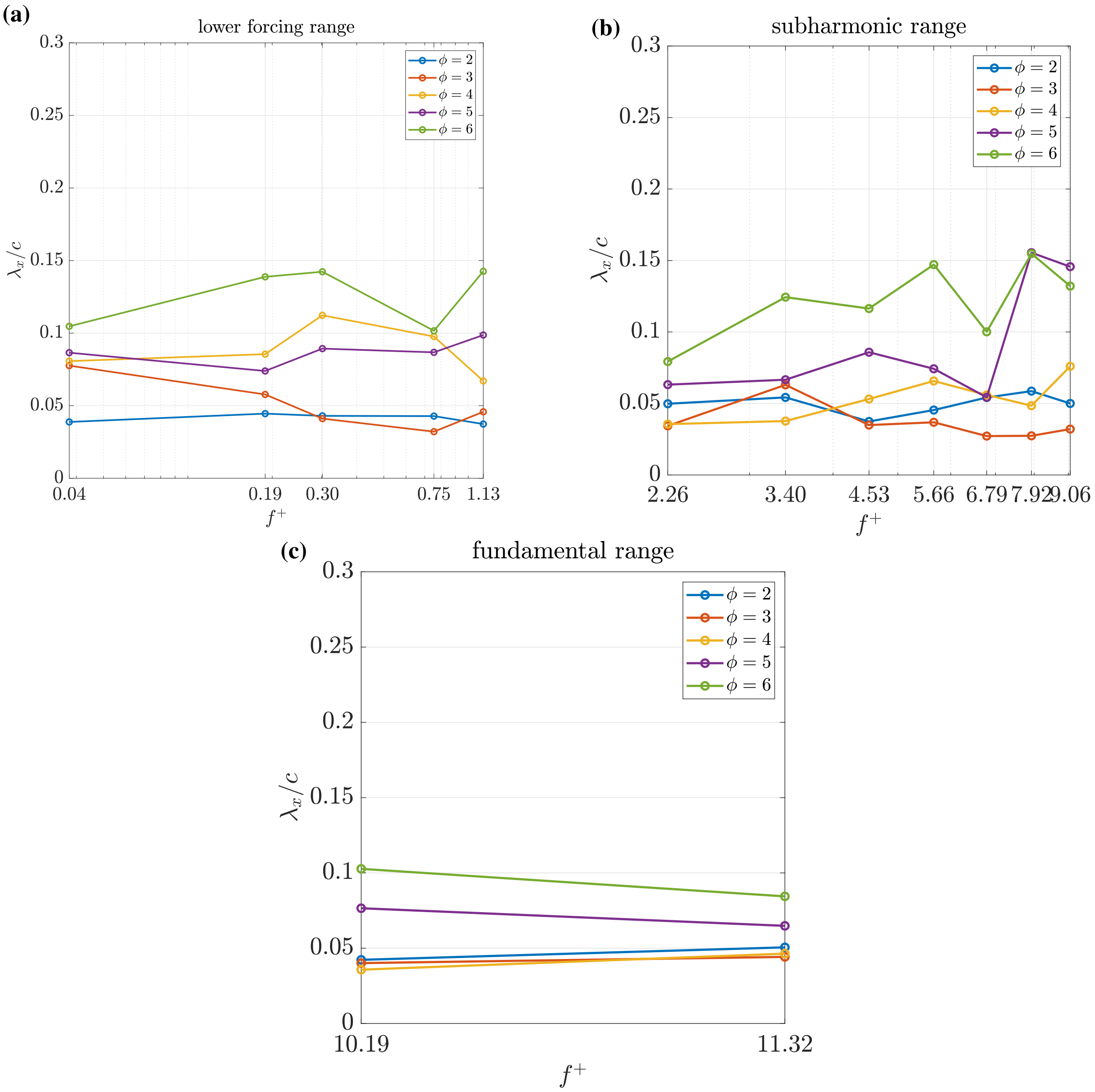

Figure 6.27: Variation of streamwise wavelength quantifying breakdown with forcing frequencies for different phases and forcing frequency categories. (a) lower forcing range (b) subharmonic range (c) fundamental range.

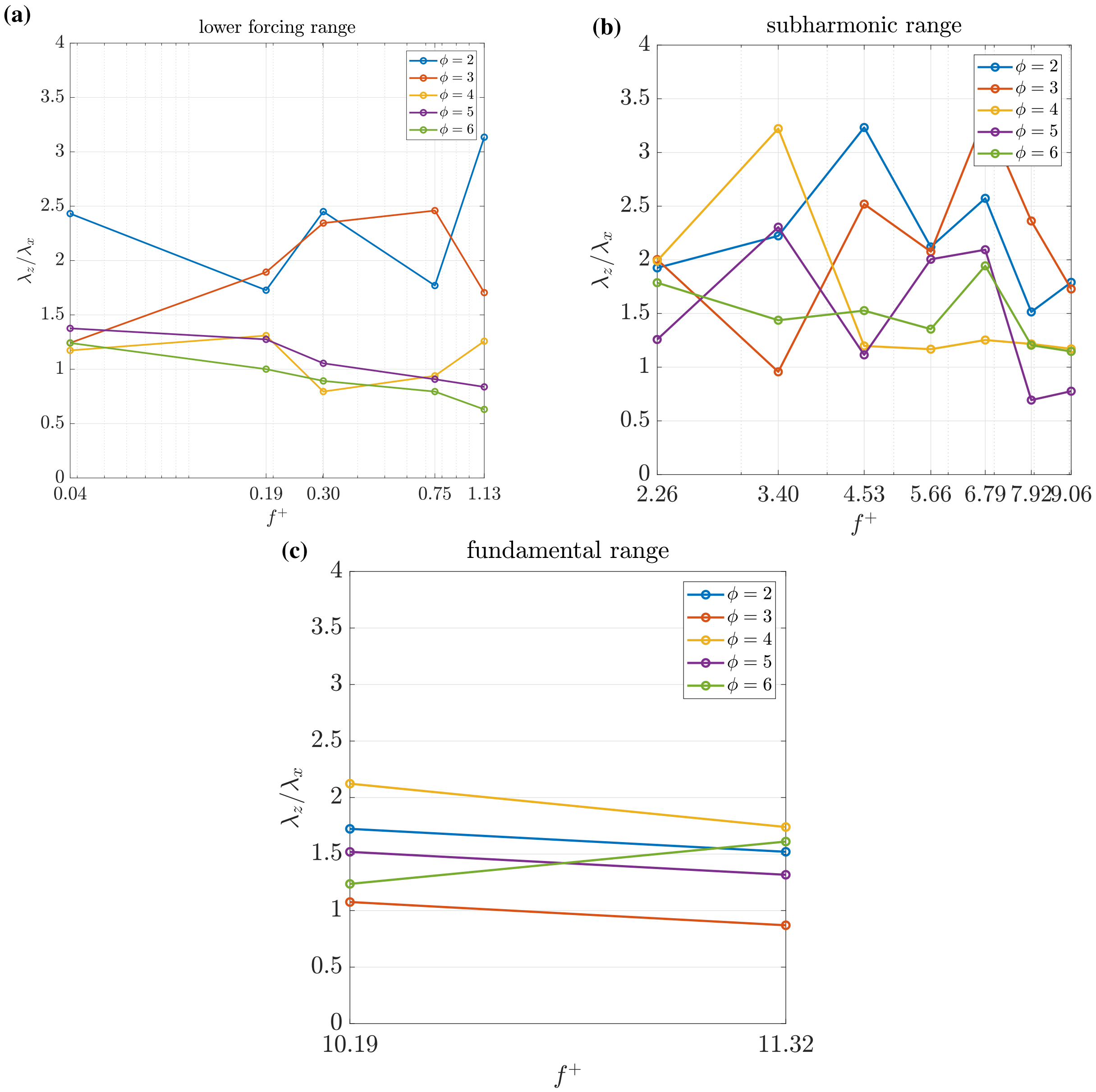

Figure 6.28: Variation of wavelength ratio quantifying breakdown with forcing frequencies for different phases and forcing frequency categories. (a) lower forcing range (b) subharmonic range (c) fundamental range.

7

Discussion and Conclusion

This work investigates how AC-DBD forcing, varied from the lower forcing to fundamental forcing frequency, alters the topology of a laminar separation bubble and the three-dimensional breakdown of the actuated wave packets. Based on the formulated research questions, an experimental matrix was chosen. Experiments were performed on a NACA0018 airfoil using planar PIV in two orthogonal planes: the wall-normal plane and the wall-parallel plane. In this section, the obtained results are discussed and synthesised to give an overview of the findings. Additionally, the posed research questions in section 3.1 are answered comprehensively.

7.1 Discussion

Changes in Bubble Topology: Mean Flow Deformation

As the forcing frequency increases, the bubble area decreases monotonically. Mean flow deformation is quantified by plotting the normalized bubble area with forcing frequency in figure 6.20. The unforced LSB obtained in the wall-normal plane serves as the baseline case for comparison. A steep decrease in bubble area occurs in the low forcing frequency range, followed by a gradual change at higher forcing frequencies. This trend in bubble area is paired and analysed with the observed flow field characteristics, and a relation between the bubble area and bubble recovery is noted. As the forcing frequency increases, the time available for bubble recovery decreases. Hence, at a particular forcing frequency, consecutive wave packets start interacting. Flow field analysis in section 6.2.2.2 identifies this frequency near $f^+ = 3.40$ for the current study. The observed steep decrease in bubble area happens before this frequency.

With an increase in forcing frequency, the displacement thickness (δ^*) moves closer to the wall, and the maximum shape factor (H) shifts upstream. This observation, in conjunction with findings from previous studies, suggests that the deformed mean flow changes the growth rates of incoming disturbances. Additionally, with an increase in forcing frequency, the corresponding standard deviation fields show reduced fluctuations and organized breakdown.

Flow-field Characteristics: Some observations

In the wall-normal plane, the phase-averaged vorticity fields are used to analyse the evolution of the wave packet. In all considered cases, a primary vortex resulting from the actuation is identified for comparison of breakdown characteristics in the wall-parallel plane. At lower forcing frequencies, this primary vortex co-rotates and merges in the aft part of the airfoil. In the intermediate forcing-frequency case, the wave packets arrive consecutively, allowing minimal bubble recovery. Here, the vortices do not merge. In the sub-harmonic cases, the vortices merge, and the shear layer remains closer to the airfoil. Under fundamental forcing, the shear layer locks into the actuated wave packet, and a coherent, organised vortex shedding is observed. The vortices do not merge, and their relative distance increases in the aft part of the airfoil.

As observed in the wall-parallel plane, the breakdown characteristics show a strong dependence on the forcing frequency. For the lower forcing frequency case, the observed breakdown characteristics resemble those of an unforced bubble and correspond to the shear-layer roll-up after the primary vortex. In the intermediate case, breakdown is observed both for the primary vortex and for a shear-layer roll-up. The breakdown characteristics are very different from each other, which indicates the effect of the mode dictating the breakdown. In the sub-harmonic case, the irregular breakdown characteristics may be attributed to possible modulation of vortices. At fundamental forcing, a very distinct breakdown pattern is observed, similar to the breakdown characteristics observed for the primary vortex for the intermediate case.

Breakdown Characteristics: Wavelength-based quantification

Spatial wavelet analysis is applied to velocity signals extracted from specific windows in the wall-parallel plane. This provided phase consistent sampling of the actuated packet and yields spanwise wavelength (λ_z), streamwise wavelength (λ_x), and their ratio (r) across phases and frequencies.

Across the defined forcing frequency ranges, the observed vortex evolution remains common: initial undulations at $\phi = 2$, breakdown at $\phi = 3$, and later phases show further evolution downstream. At the low forcing frequency range, the spanwise wavelengths do not show much variation with phase, and the observed breakdown in section 6.2.2.2 is similar to the breakdown of an unforced bubble. In the subharmonic forcing, the wavelength variation with phase shows a distinct "U"-shape. For the fundamental forcing case, a different trend in breakdown is seen both in the wall parallel velocity and vorticity fields with a moderate "U"-shape across the phases, indicating different breakdown characteristics than previous ranges.

Streamwise wavelengths increase with phase for all forcing frequencies. Across the defined forcing frequency ranges, the observed vortex evolution remains common: initial spacing at $\phi = 2$, breakdown at $\phi = 3$, and further evolution downstream. Later phases generally show an increase due to merging in subharmonic forcing frequencies, both merging and out-of-plane motion at lower forcing frequencies, and an increase in distance due to lock-in for fundamental forcing frequencies.

The spanwise to streamwise wavelength ratio λ_z/λ_x indicates the three-dimensional breakdown. In the low-forcing range, the ratio r reaches its highest value at phase $\phi = 2$ and then reduces at $\phi = 3$ to a value that matches the wavelength ratio of the unforced bubble. This similarity suggests that, under low forcing, the vortices follow a breakdown pathway similar to an unforced bubble. As the structures convect downstream, r gradually decreases because the streamwise wavelength grows when vortices merge or move out of the wall-parallel plane. In the sub-harmonic range, r corresponding to higher forcing frequencies in the regime shows only a gradual decline. This may be due to the modulation or merging of the shed vortices, leading to a different breakdown topology. Fundamental range also shows a similar trend, though no modulation and merging of vortices is observed.

7.2 Conclusion

The research questions guiding this work and their comprehensive answers are stated here.

1. How does the LSB topology vary with a two-dimensional AC-DBD actuation frequency ranging from impulsive to fundamental forcing frequency?

   Answer: As the forcing frequency increases, the LSB topology varies significantly. Mean Flow Deformation (MFD) is observed for all the considered cases and is quantified in terms of bubble area. The bubble area decreases with an increase in forcing frequency. While the bubble area decreases steeply in the lower forcing frequency range, it shows a gradual change in the subharmonic and fundamental frequency range. With an increase in forcing frequency, the displacement thickness moves closer to the airfoil, and the shape-factor moves upstream, indicating enhanced stability of the shear layer for incoming natural disturbances and early transition, respectively. Both effects are observed in time-averaged velocity fields: the changed stability results in different breakdown characteristics, and the early transition causes early reattachment. Additionally, the standard deviation fields show a reduction in fluctuations with an increase in frequency.

2. How does the 3D breakdown of the shed vortex, quantified in terms of wavelengths of coherent structures in streamwise and spanwise directions, vary over the range of actuation frequency?

   Answer: The 3D breakdown of the shed vortex shows definitive trends with different actuation frequency regimes.

   Spanwise wavelength trend: At the low forcing frequency range, the spanwise wavelength does not vary much across phases and shows a trend similar to the breakdown of an unforced bubble vortex. In the sub-harmonic range, the wavelength variation with phase is U-shaped. In the initial phase, the value of wavelength is high as it indicates coherence of the shed structure; it decreases as the structure breaks down and then increases due to possible modulation and movement out of plane. In the fundamental forcing regime, though the sequence of breakdown remains the same and the wavelength variation with phase is a mild U-shape, the breakdown characteristics change considerably.

   Streamwise wavelength trend: The wavelength value increases with phase for all forcing frequencies. In the low-forcing frequency range, the wavelength increases downstream as they merge and move out of plane. A similar trend is also observed for the sub-harmonic forcing frequency, although the increase in wavelength is primarily because of merging. For the fundamental forcing, the increase is attributed to the lock-in and the increasing spacing between shed vortices in the aft part of the airfoil.

8

Recommendations

In this chapter, recommendations arising from the findings and limitations of the present study are presented. First, practical suggestions are provided concerning improvements to the experimental setup, measurement strategy, and data-processing procedures that could enhance the robustness of future investigations. Subsequently, directions for further research are outlined, with emphasis on future choice of experimental matrix, refining the characterisation of three-dimensional breakdown, and other analysis techniques.

8.1 Experimental Setup

During the course of this thesis, several experimental limitations were encountered that affected the analysis and quality of results discussion and interpretation. The following list highlights the recommendations corresponding to the experimental setup.

- **Laser sheet misalignment and Airfoil Leading Edge alignment:** Laser-sheet misalignment caused the wall-parallel plane to intersect the flow structures at different heights above the airfoil surface, resulting in uneven visualization. At the leading edge, a misalignment between the two assembled parts of the model was observed. This led to different disturbance growth rates. This was visible in multiple velocity contours throughout the thesis. Future experiments could be careful about handling these experimental limitations.
- **Phase offset:** A phase offset between the wall-normal and wall-parallel planes was observed for all cases, the origin of which remains unclear. Despite strict experimental procedures, the offset may indicate an accidental delay in parameter setting; careful synchronization in future campaigns would mitigate this limitation.
- **Geometry masking:** Masking near the airfoil wall in the wall-normal plane was performed in DaVis, which offered limited control. As a result, near-wall velocity vectors were excluded and subsequently had to be extrapolated. A more accurate approach would be to perform the masking in MATLAB using a precise airfoil outline for the wall-normal plane, and then import the masked velocity field into DaVis for further processing.
- **Multiple plane actuator characterization:** Pre-and post-test actuator characterization would be beneficial. Testing the actuator across a larger number of spanwise planes would enable verification of spanwise uniformity of the actuation input. Such characterization would help establish that the actuator forcing remains uniform over time and along the span during the experiments.

- **Projection of structures into Wall-parallel plane:** Interpretation of characteristic wavelengths is constrained by two experimental factors. Firstly, for extracting phase-locked wavelengths, phase windows were used while the packet convects, introducing bias. Secondly, the airfoil curvature causes the wall-parallel plane to cut the structures at varying angles, leading to projection bias in λ_x, λ_z, and hence the ratio. These limitations could be mitigated in future work by employing a different model or by using multi-dimensional, multi-component measurement techniques.

8.2 Future research

During the course of this thesis, several conclusions were drawn. This also highlighted a number of possible analysis and investigation directions that can be further pursued. The list highlights the recommendations concerning further research directions.

- **Investigation into the switch point:** While a switch point was identified, it was determined approximately from the existing experimental dataset and therefore does not represent the exact location. Future work should explore a finer sweep of actuation frequencies within the identified window to pinpoint the switch more precisely and to relate the local mean-flow deformation to the breakdown dynamics at that location.
- **Stability analysis:** Linear stability theory (LST) can be used to quantify the growth of disturbances and compare the amplification rates of different modes. This would also help better understand the breakdown characteristics. A secondary instability analysis (SIA) may be performed on the time-periodic vortex that results from saturation of the primary mode. Such an analysis can quantify the growth rates of secondary modes and investigate the spanwise and streamwise wavenumber ranges over which the shed vortex is unstable.
- **Modal analysis:** Proper Orthogonal Decomposition can identify dominant structures and their energy, while the temporal coefficients capture the time evolution/modulation of the corresponding spatial modes, including large-scale low-frequency motions and checkerboard patterns associated with oblique modes.
- **Stereoscopic/Planar/Tomographic Time Resolved-PIV:** A sophisticated diagnosis choice would provide additional velocity components and temporal resolution for a detailed modal, spectral, and stability analysis used in tandem to probe the flow dynamics deeply. This can also help address faced issues such as out-of-plane motion.

Bibliography

Aftab, S., A. Mohd Rafie, N. Razak, and K. Ahmad (2016). Turbulence model selection for low reynolds number flows. *PloS one 11*(4), e0153755.

Alam, M. and N. D. Sandham (2000). Direct numerical simulation of 'short' laminar separation bubbles with turbulent reattachment. *Journal of Fluid Mechanics 410*, 1–28.

Avanci, M. P., D. Rodríguez, and L. S. d. B. Alves (2019). A geometrical criterion for absolute instability in separated boundary layers. *Physics of Fluids 31*(1).

Borgmann, D., S. Hosseinverdi, J. C. Little, and H. F. Fasel (2021). Investigation of laminar separation bubbles using experiments, theory and dns. In *AIAA Aviation 2021 Forum*, pp. 2898.

Borgmann, D., S. Hosseinverdi, J. C. Little, and H. F. Fasel (2022). Active control of boundary-layer transition in laminar separation bubbles. In *AIAA Scitech 2022 Forum*, pp. 2433.

Borgmann, D., J. Little, and H. Fasel (2025). Active control of transition to turbulence in laminar separation bubbles. *Journal of Fluid Mechanics 1016*, A59.

Boutilier, M. S. H. and S. Yarusevych (2012, August). Separated shear layer transition over an airfoil at a low Reynolds number. *Physics of Fluids 24*(8), 084105.

Chandrasekhar, S. (2013). *Hydrodynamic and hydromagnetic stability*. Courier Corporation.

Dellacasagrande, M., D. Barsi, D. Lengani, and D. Simoni (2024, July). Instability processes in short and long laminar separation bubbles. *Exp Fluids 65*(7), 109.

Dellacasagrande, M., D. Lengani, D. Simoni, and S. Yarusevych (2023, December). A data-driven analysis of short and long laminar separation bubbles. *J. Fluid Mech. 976*, R3.

Diwan, S. S. and O. N. Ramesh (2009, June). On the origin of the inflectional instability of a laminar separation bubble. *J. Fluid Mech. 629*, 263–298.

Dovgal, A., V. Kozlov, and A. Michalke (1994). Laminar boundary layer separation: instability and associated phenomena. *Progress in Aerospace Sciences 30*(1), 61–94.

Gaster, M. (1967). The structure and behaviour of separation bubbles.

Herbert, T. (1988). Secondary instability of boundary layers. *Annual review of fluid mechanics 20*, 487–526.

Horton, H. P. (1968). *Laminar separation bubbles in two and three dimensional incompressible flow.* Ph. D. thesis, Queen Mary University of London.

Hosseinverdi, S. and H. F. Fasel (2018). Role of klebanoff modes in active flow control of separation: direct numerical simulations. *Journal of Fluid Mechanics 850*, 954–983.

Kundu, P. K., I. M. Cohen, D. R. Dowling, and J. Capecelatro (2024). *Fluid mechanics*. Elsevier.

Kurelek, J. (2021). The vortex dynamics of laminar separation bubbles.

Kurelek, J. W., M. Kotsonis, and S. Yarusevych (2023). Superposition of ac-dbd plasma actuator outputs for three-dimensional disturbance production in shear flows. *Experiments in Fluids 64*(4), 84.

Kurelek, J. W., A. R. Lambert, and S. Yarusevych (2016). Coherent structures in the transition process of a laminar separation bubble. *AIAA Journal 54*(8), 2295–2309.

Kurelek, J. W., B. A. Tuna, S. Yarusevych, and M. Kotsonis (2021). Three-dimensional development of coherent structures in a two-dimensional laminar separation bubble. *AIAA Journal 59*(2), 493–505.

Kurelek, J. W., S. Yarusevych, and M. Kotsonis (2019). Vortex merging in a laminar separation bubble under natural and forced conditions. *Physical Review Fluids 4*(6), 063903.

Lambert, A. and S. Yarusevych (2019). Effect of angle of attack on vortex dynamics in laminar separation bubbles. *Physics of Fluids 31*(6).

Lambert, A. R. and S. Yarusevych (2017, August). Characterization of Vortex Dynamics in a Laminar Separation Bubble. *AIAA Journal 55*(8), 2664–2675.

Lissaman, P. B. S. (1983). Low-reynolds-number airfoils. *Annual Review of Fluid Mechanics 15*(1), 223–239.

Mack, L. M. (1984). Boundary-layer linear stability theory. *Agard rep 709*.

Marxen, O. and D. S. Henningson (2011, March). The effect of small-amplitude convective disturbances on the size and bursting of a laminar separation bubble. *J. Fluid Mech. 671*, 1–33.

Marxen, O., M. Lang, and U. Rist (2013, August). Vortex formation and vortex breakup in a laminar separation bubble. *J. Fluid Mech. 728*, 58–90.

Marxen, O., M. Lang, U. Rist, O. Levin, and D. S. Henningson (2009). Mechanisms for spatial steady three-dimensional disturbance growth in a non-parallel and separating boundary layer. *Journal of Fluid Mechanics 634*, 165–189.

Marxen, O. and U. Rist (2010). Mean flow deformation in a laminar separation bubble: separation and stability characteristics. *Journal of Fluid Mechanics 660*, 37–54.

McMasters, J. H. and M. L. Henderson (1979). Low-speed single-element airfoil synthesis. *NASA. Langley Res. Center The Sci. and Technol. of Low Speed and Motorless Flight, Pt. 1*.

Merino-Martínez, R., A. R. Carpio, L. T. L. Pereira, S. van Herk, F. Avallone, D. Ragni, and M. Kotsonis (2020). Aeroacoustic design and characterization of the 3d-printed, open-jet, anechoic wind tunnel of delft university of technology. *Applied Acoustics 170*, 107504.

Michelis, T. (2017). *Boundary Layer Separation: Diagnostics and Control*. Ph. D. thesis, Delft University of Technology.

Michelis, T., M. Kotsonis, and S. Yarusevych (2018, September). Spanwise flow development within a laminar separation bubble under natural and forced transition. *Experimental Thermal and Fluid Science 96*, 169–179.

Michelis, T., S. Yarusevych, and M. Kotsonis (2017, June). Response of a laminar separation bubble to impulsive forcing. *J. Fluid Mech. 820*, 633–666.

Michelis, T., S. Yarusevych, and M. Kotsonis (2018, April). On the origin of spanwise vortex deformations in laminar separation bubbles. *J. Fluid Mech. 841*, 81–108.

Monkewitz, P. (1990). The role of absolute and convective instability in predicting the behavior of fluid systems. *European Journal of Mechanics, B/Fluids 9*(5), 395–413.

Morkovin, M. V. (1994). Transition in open flow systems-a reassessment. *Bull. Am. Phys. Soc. 39*, 1882.

Mueller, T. J. and B. JANSEN, JR (1982). Aerodynamic measurements at low reynolds numbers. In *12th Aerodynamic Testing Conference*, pp. 598.

Prandtl, L. (1904). Über flüssigkeitsbewegung bei sehr kleiner reibung. In *Verhandlungen des dritten internationalen Mathematiker-Kongresses in Heidelberg*, pp. 484–491.

Raffel, M., C. E. Willert, F. Scarano, C. J. Kähler, S. T. Wereley, and J. Kompenhans (2018). *Particle image velocimetry: a practical guide*. springer.

Reed, H. L. and W. S. Saric (2015, June). Receptivity: The Inspiration of Mark Morkovin (Invited). In *45th AIAA Fluid Dynamics Conference*, Dallas, TX. American Institute of Aeronautics and Astronautics.

Rist, U. (2002). On instabilities and transition in laminar separation bubbles. In *Proc. CEAS Aerospace Aerodynamics Research Conference*, pp. 10–12.

Rist, U. and K. Augustin (2006). Control of laminar separation bubbles using instability waves. *AIAA journal 44*(10), 2217–2223.

Rist, U. and U. Maucher (2002). Investigations of time-growing instabilities in laminar separation bubbles. *European Journal of Mechanics-B/Fluids 21*(5), 495–509.

Robinet, J.-C. (2013, October). Instabilities in laminar separation bubbles. *J. Fluid Mech. 732*, 1–4.

Rodríguez, D., E. M. Gennaro, and M. P. Juniper (2013, November). The two classes of primary modal instability in laminar separation bubbles. *J. Fluid Mech. 734*, R4.

Rodríguez, D., E. M. Gennaro, and L. F. Souza (2021, January). Self-excited primary and secondary instability of laminar separation bubbles. *J. Fluid Mech. 906*, A13.

Saric, W. S., H. L. Reed, and E. J. Kerschen (2002). Boundary-layer receptivity to freestream disturbances. *Annual review of fluid mechanics 34*(1), 291–319.

Schlichting, H. and K. Gersten (2017). *Boundary-Layer Theory*. Berlin, Heidelberg: Springer Berlin Heidelberg.

Tani, I. (1964). Low-speed flows involving bubble separations. *Progress in Aerospace Sciences 5*, 70–103.

Tani, I. (1969). Boundary-layer transition. *Annual Review of Fluid Mechanics 1*(1), 169–196.

Watmuff, J. H. (1999). Evolution of a wave packet into vortex loops in a laminar separation bubble. *Journal of Fluid Mechanics 397*, 119–169.

White, F. M. and J. Majdalani (2006). *Viscous fluid flow*, Volume 3. McGraw-Hill New York.

Yarusevych, S. and M. Kotsonis (2017, February). Steady and transient response of a laminar separation bubble to controlled disturbances. *J. Fluid Mech. 813*, 955–990.

Zaman, K., D. McKinzie, and C. Rumsey (1989). A natural low-frequency oscillation of the flow over an airfoil near stalling conditions. *Journal of Fluid Mechanics 202*, 403–442.